HIDRAULICA

HYDRAULICS-PNEUMATICS-TRIBOLOGY-ECOLOGY-SENSORICS-MECHATRONICS

CONTENTS

EDITORIAL

Transferul tehnologic de dulap

Se poate accepta ca unul din elementele de baza ale dezvoltarii economice il constituie dezvoltarea industriala. Acest lucru implica imediat intrebari referitoare la cine concepe, la ce nivel tehnico-stiintific se discuta, cum se face transferul, cine preia noutatile care sa permita dezvoltarea si pe ce criterii se desfasoara aceste activitati.

Primul subiect de discutie il constituie precizarea ideii de cercetare aplicativa, care in final nu reprezinta niste studii, niste metodologii sau idei constructive generale, ci proiecte concrete de produse cu toate cele necesare asimilarii in fabricatie. Rezultatele cercetarii aplicative

Dr. ing. Petrin DRUMEA
DIRECTOR DE PUBLICATIE

trebuie sa fie usor de asimilat in fabricatie si sa nu devina niste documente inutile, bune de depozitat intr-un dulap in care sa nu se mai umble nicicand. Ideea de cercetare aplicativa teoretica este de neacceptat, este un nonsens si ascunde de fapt incompetenta elaboratorilor de a se adapta cerintelor industriei.

Un al doilea subiect de discutie il constituie definirea corecta a transferului tehnologic. Conceptul porneste de la existenta pe piata a unor produse si a unor fabricanti care nu se intalnesc si pentru care ar trebui sa existe o a treia parte care sa ii puna cap la cap pe cei doi si care sa poata sprijini metodologic apropierea lor. Preluarea ideii si la noi in tara s-a facut destul de repede, fara insa a se face o analiza serioasa a marimii nevoii de unitati de transfer tehnologic si, ca urmare, ne-am trezit cu realizarea unui mare numar de centre specializate pe acest domeniu, care de fapt nu au nicio activitate practica utila. Este evident ca daca numarul celor care realizeaza proiecte pe care nu le transfera este mic, daca numarul celor care doresc sa preia proiecte este mic, nu are cum sa fie mare numarul celor care se ocupa de transfer tehnologic. Rezultatul practic al acestei situatii este ca de multe ori centrele se fac ca preiau proiecte pe care apoi se fac ca le transfera si in final hartiile se baga in dulapuri de care nimeni nu se va apropia niciodata.

Un al treilea subiect de discutat este modalitatea de imbunatatire a sistemului de transfer tehnologic, pentru ca despre necesitatea acestuia nu cred ca exista indoieli. Prima masura cred ca este largirea numarului de specialisti care sa produca proiecte adecvate si usor transferabile in industrie. A doua masura ar trebui sa fie sprijinirea institutionala a celor care pot si doresc sa preia rezultatele cercetarii. A treia masura care s-ar impune ar fi ca prin intermediul centrelor de transfer tehnologic sa se creeze niste modalitati simple de intalnire a cercetatorului cu producatorul.

In final, revin la ideea ca este nevoie de adaptarea cercetarii aplicative la nevoile industriei realizand produse si nu hartii de depozitat in dulapuri si la ideea ca centrele de transfer tehnologic ar fi bine sa fie un intermediar prietenos.

EDITORIAL

File Box Technology Transfer

One can admit that one of the basic elements of economic development is the industrial development. This immediately involves questions about who conceives, at what scientific and technical level is the matter discussed, how the transfer is made, who takes over updates that enable development and what criteria such activities are undertaken on.

The first topic of discussion would be a more accurate stating of the idea of applied research, which ultimately should not be represented by some studies, methodologies or general constructive ideas, but by actual projects of products with everything needed for uptake in

Ph.D.Eng. Petrin DRUMEA
DIRECTOR OF PUBLICATION

manufacturing. The results of applied research must be easily assimilable in manufacturing and they should not become some useless documents, suited to be stored in a file box which no one will ever open. The idea of theoretical applied research is unacceptable; it is nonsense and actually covers incompetence of the elaborators to adapt to industry requirements.

A second topic of discussion would be a correct definition of technology transfer. The concept starts from the situation of certain products and certain manufacturers existing on the market but not meeting each other, for which there should be a third party that would put together the former two parties and would be able to methodologically support their convergence.The idea has been taken oven in our country quite quickly, but without making a reliable analysis on sizing the need for technology transfer units and, as a result, we have found ourselves developing a large number of specialized centers in this area, which in fact have no useful practical activity. It stands to reason that if the number of those who carry out projects which they do not transfer is a small one, if the number of those willing to uptake projects is a small one, the number of those dealing with technology transfer could not possibly be a large one. The practical result of this is that often those centers pretend to uptake projects which they further pretend to transfer and in the end the papers are put in file boxes that no one will ever get close to.

A third topic to be discussed is how to improve the technology transfer system, as I think there are no doubts about the necessity of it. I consider the first step to be taken would be to broaden the number of specialists able to produce projects which are adequate and readily transferable to industry. A second step should be to grant institutional support to those who can and want to uptake the research results. A third step required would be that through technology transfer centers some simple ways of gathering the researcher and the manufacturer to be created.

In the end, I reiterate the idea that it is necessary for applied research to adapt to the needs of industry making products, not papers to be stored in file boxes, and also the idea that the technology transfer centers would be better to be a friendly intermediate agent.

Configurations of the Flow Induced by a Fan Impeller without Casing

Lecturer PhD Eng. **Andrei DRAGOMIRESCU**[1]

[1] University Politehnica of Bucharest, Department of Hydraulics, Hydraulic Machinery and Environmental Engineering, andrei.dragomirescu@upb.ro

Abstract: *This paper presents a study of the turbulent, compressible air flow induced by a fan impeller without scroll casing. The equations governing the flow – continuity equation, momentum equations, energy equation and the equation of state – were solved numerically using the finite volume method. The Reynolds Stress Model was used to provide the closure equations. Different simulations were made by changing the overpressure imposed as boundary condition at the outflow. The overpressure was varied stepwise between the choke limit and the limit corresponding to reversed flow. Despite the symmetry of geometry and boundary conditions, the results obtained indicate the appearance of non-axisymmetrical solutions. Moreover, two bifurcating solutions were obtained at certain operating points. These solutions are characterized by two and, respectively, three dominant directions of the flow outside the impeller. By dominant directions we denote regions where the velocity is higher than in neighboring areas at the same radius. Based on the results, a bifurcation diagram is plotted. The bifurcating solutions lead to different values of the average mass flow rate delivered by the impeller for the same outflow pressure. This could offer an explanation for the hysteresis of the characteristic curves of some pneumatic turbomachines. Moreover, the dominant directions extend inside the impeller and cause time-periodic pressure pulsations on the blade, which could be an additional explanation for the vibrations and noise in pneumatic turbomachines.*

Keywords*: bifurcating solutions, compressible flow, flow configurations, free impeller, high pressure fan*

1. Introduction

High pressure fans are fans that, considering the classifications in ISO 13349 [1], have compression rations between 1.1 and 1.3 when they pump air having a density of 1.2 kg/m^3. The EUROVENT norms [2] define different limits and, according to them, high pressure fans have compression ratios between 1.036 and 1.3. The compressible turbulent gas flows (usually air flows) induced by impellers of high pressure fans are governed by the equation of state and several partial differential equations: continuity equation, momentum equations, and energy equation. To these, the closure equations corresponding to the turbulence model chosen to study the flow should be added. Due to the continuous movement of the fan impeller, the gas flow is inherently unsteady, so that the governing partial differential equations can be written in the following condensed form:

$$\frac{\mathrm{d}\mathbf{U}}{\mathrm{d}t} = \mathbf{F}(\boldsymbol{\mu}, \mathbf{U}),\tag{1}$$

with the initial value

$$\mathbf{U}(0) = \mathbf{U}_0 \tag{2}$$

and associated boundary conditions. In the above equations $\mathbf{U}$ is the vector of flow variables (velocity components, pressure, temperature, density, turbulent variables), $\mathbf{F}$ is a vector function whose components are functions of the components of $\mathbf{U}$, and $\boldsymbol{\mu}$ is a vector of parameters (gas viscosity, coefficient of thermal conductivity, etc.). A solution to which equation (1) evolves after the transient effects associated with the initial values (2) have diminished is called *asymptotic solution*. It should be mentioned here that $\mathbf{U} = \mathbf{0}$ cannot be a solution of the problem, since $\mathbf{U} \neq \mathbf{0}$ is forced by nonzero forcing data embedded in $\mathbf{F}(\boldsymbol{\mu}, \mathbf{U})$, and, if applicable, in the boundary conditions. Examples of nonzero forcing data are the pressure force per unit mass, $\nabla p/\varrho$, and, in a non-inertial reference frame attached to the impeller, the centrifugal force per unit mass, $\boldsymbol{\omega} \times (\boldsymbol{\omega} \times \mathbf{r})$, where ϱ is the gas density, vector $\boldsymbol{\omega}$ is the angular velocity of the impeller, and $\mathbf{r}$ is the position vector. Among the possible asymptotic solutions of the autonomous problem formulated above there are (i) steady solutions and (ii) T-periodic solutions of the form $\mathbf{U}(t) = \mathbf{U}(t + T)$. Asymptotic solutions
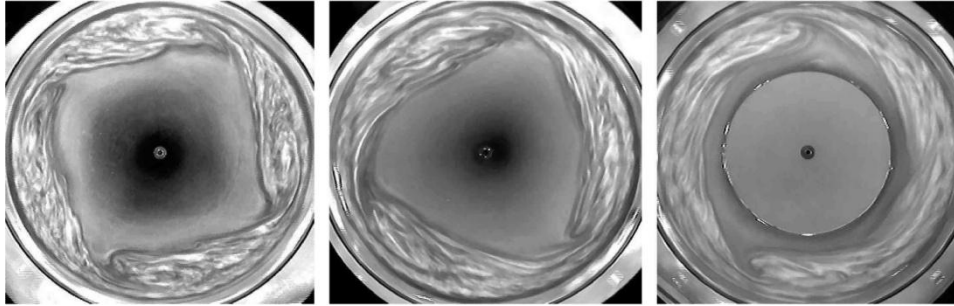
Fig. 1. Flow configurations induced by a disc rotating inside a casing, obtained experimentally by Poncet and Chauve [8]

which form intersecting branches in a suitable space of functions are called *bifurcating solutions*. It is said that one asymptotic solution bifurcates from another at $\mu = \mu_0$ if there are two distinct asymptotic solutions $\mathbf{U}^1(\mu, t)$ and $\mathbf{U}^2(\mu, t)$, continuous in μ, such that $\mathbf{U}^1(\mu_0, t) = \mathbf{U}^2(\mu_0, t)$. One work, in which the bifurcation theory is extensively treated, is that of Ioos and Joseph [3].

An important characteristic of bifurcation is the appearance of solutions that can break the symmetry pattern of the forcing data, should this symmetry exists. Thus, non-symmetrical solutions are possible even when the geometry and the boundary conditions are symmetrical.

It is often true that a necessary condition for bifurcation is the instability of the asymptotic solution to small disturbances. In a real flow, disturbances are usually small deviations in the symmetry of the geometry due to manufacturing imperfections, slight changes in the upstream or downstream flow conditions, etc. In a numerical simulation, disturbances can be introduced by the inherent numerical errors.

Bifurcating solutions were found experimentally and numerically even in cases of simple flows, like those through symmetrical sudden expansions [4, 5], through a symmetrical channel with a sudden expansion and a sudden contraction [6], or through a lid driven cavity with throughflow [7]. More recently, Poncet and Chauve [8] identified experimentally different configurations, without axial symmetry, of the flow induced by a rotating disc enclosed by a fixed cylindrical shroud. Central hubs having different radii were attached to the disk. Above a certain threshold, the flow shows different modes characterized by sharp-cornered polygonal patterns with m vortices. The number of vortices changes as the rotational Reynolds number, Re, increases and shows a noticeably hysteresis when Re decreases. Three modes observed by Poncet and Chauve, with 2, 3, and 4 vortices, are presented in Figure 1 for subsequent comparisons. Ciocanea [9] investigated numerically the fluid motion induced by a rotating disk inside a vessel and found flow configurations with different numbers of inner vortices depending on the Reynolds number calculated based on disk radius.

This paper investigates another type of rotational flow and its instabilities. It is the compressible turbulent air flow induced by a free impeller, i.e. an impeller without scroll casing, of a high pressure fan. The study was performed by means of numerical simulations. In the following, the problem is formulated in terms of geometry, flow equations, fluid parameters and numerical algorithms. The results are then presented and discussed and conclusions are drawn.

2. Problem description

The study was performed for the impeller of a high pressure fan designed for a rated compression ratio of $\tau = 1.3$ and a rotational speed of $5000\,\mathrm{rpm}$ to which the angular velocity $\omega = 526.6\,\mathrm{rad/s}$ and the rotational frequency $f = 83.33\,\mathrm{Hz}$ correspond. The design was based on a method proposed by Pfleiderer and Petermann [10]. In many cases, in order to keep the geometry of the machine as simple as possible, so that the manufacturing process is simplified and the cost is reduced, fan impellers have a constant width from inlet to outlet. For this reason we chose to use a two-dimensional geometry in our study. The computational domain consists of the impeller and two annular zones placed inside and outside the impeller. A sketch of a part of the computational domain, comprising the impeller, is presented in Figure 2. The impeller rotates counter-clockwise. The diameter at impeller inlet is $D_1 = 330\,\mathrm{mm}$, while at outlet the diameter is $D_2 = 660\,\mathrm{mm}$. The
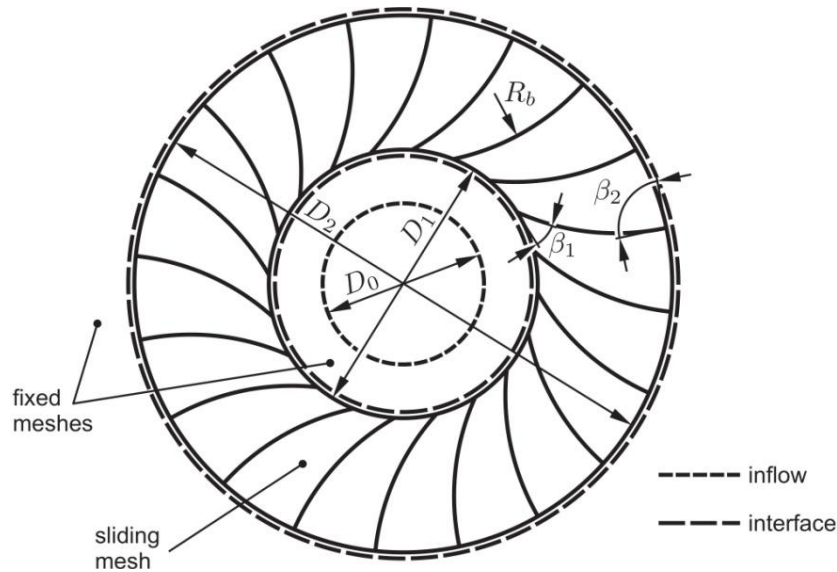
Fig. 2. Impeller geometry and configuration of the computational domain

impeller has 20 blades shaped as circular arcs of radius $R_b = 296\,\text{mm}$ and having the angles $\beta_1 = 33.5°$ at inlet and $\beta_2 = 90°$ at outlet. For the imposed rotational speed and the chosen number of blades, the blade passing frequency is $f_b = 1666.7\,\text{Hz}$.

The inflow boundary is situated at diameter $D_0 = 0.6D_1 = 198\,\text{mm}$, while the outflow boundary lies at diameter $D_3 = 3D_2 = 2040\,\text{mm}$. For the sake of clarity, diameter D_3 is not visible in Figure 2. The working fluid is air considered to be a perfect gas.

Both the turbulence and the rotational movement of the impeller render the flow unsteady. Turbulence was treated using a second order closure model, namely the Reynolds Stress Model. The reason for this choice, instead of a simpler, two equations model, is that second order closure models are designed to handle effects that cannot be caught by two equations turbulence models. Such effects are streamline curvature, sudden changes in strain rate, and secondary motion, which are likely to appear in the flow under study. In the Reynolds Stress Model the turbulent stresses are not modeled but solved, one additional transport equation being added for each turbulent stress [11].

The equations governing the unsteady turbulent compressible flow – continuity equation, momentum equations, energy equation, transport equations for turbulent quantities, and equation of state – were solved numerically by means of the finite volume method using the coupled solver in implicit formulation implemented in the commercial code Ansys Fluent. The continuity, momentum and energy equations were discretized using a second order upwind scheme, while the Reynolds stresses were discretized with a first order upwind scheme. The temporal discretization of the coupled equations was accomplished by a second order implicit time-marching scheme.

The reference pressure and the reference absolute temperature were chosen as $p_0 = 10^5\,\text{Pa}$ and $T_0 = 300\,\text{K}$, respectively. The required properties of air – dynamic viscosity, specific heat at constant pressure, and coefficient of thermal conductivity – were input as piece-wise linear functions of temperature using data found in literature [11]. As boundary conditions, the relative total pressure $p_{t_0} = 0\,\text{Pa}$ and the absolute temperature $T_0 = 300\,\text{K}$ were set at inflow. The no-slip condition was imposed on the blades. Simulations were performed for relative static pressures at outflow, p_r, ranging from $16000\,\text{Pa}$ to $34000\,\text{Pa}$.

The first simulation was performed for an outflow pressure of $20000\,\text{Pa}$. The initial guess for this simulation was obtained through auxiliary computations, in which the angular velocity of the impeller and the outflow static pressure were increased stepwise, in a coupled manner, starting from values close to zero, until the angular velocity reached the desired value of $523.6\,\text{rad}/s$ at an outflow pressure of $20000\,\text{Pa}$. After that, the solution of the last time step of each simulation was used as initial guess for the next simulation. For each new simulation the outflow static pressure was increased or decreased, as appropriate, by $1000\,\text{Pa}$. At each value of the outflow static pressure the simulations were advanced in time with the time step $\Delta t = 0.00015\,s$ until a

stabilization of the mass flow rate delivered by the impeller around an average value was observed for at least 40 revolutions of the impeller (3200 time steps).

As convergence criterion the drop of all scaled residuals by at least three orders of magnitude at each time step was imposed. The residuals were scaled by dividing them to the highest residual obtained in the first five iterations of the first auxiliary simulation.

Simulations were attempted also for outflow static pressures outside the range $16000 \ldots 34000\,\mathrm{Pa}$, but the results suggested that pressures below $16000\,\mathrm{Pa}$ lead to choke, while pressures above $34000\,\mathrm{Pa}$ cause a reversed flow through the impeller.

3. Results and discussion

The first results, obtained for $p_r = 20000\,\mathrm{Pa}$, indicate that outside the impeller the flow is not axisymmetrical, as expected, but it shows three regions of higher velocity. We will denote further these regions as dominant flow directions. Figure 3 shows contours of absolute velocity and streamlines plotted outside the impeller, which make evident the dominant flow directions. It can be seen that the three directions are practically equally spaced at angles of $120°$, the flow possessing a three-fold rotational symmetry with respect to impeller axis.

An image of an axisymmetrical flow, which could be induced by the impeller under study, can be obtained by means of the potential flow theory. The usage of considerations derived from this theory when designing turbomachines remains a common practice. If the flow outside the impeller is accepted to be potential and incompressible, then this flow can be regarded as a superposition of a source of volumetric flow rate Q and a potential vortex of circulation Γ, which rotates counter-clockwise, as the impeller does. The streamlines of such a flow are logarithmic spirals, which in polar coordinates (r, θ) have the equation

$$r = A\mathrm{e}^{(Q/\Gamma)\theta}, \tag{3}$$

where A is a constant whose value identifies a specific streamline in the family of streamlines. For a given streamline, the constant A can be easily computed if the coordinates (r, θ) of a point of the streamline are known. Both the flow rate Q and the circulation Γ can be computed using the results of the simulations. The flow rate should be equal to that pumped by the impeller and, at a particular diameter D, it can be computed with the formula

$$Q = \int_0^{\pi D} v_r \, \mathrm{d}s, \tag{4}$$

where v_r is the radial velocity obtained from simulations at diameter D and s is the coordinate along the circular path of diameter D.

Fig. 3. Contours of absolute velocity in m/s (left) and streamlines (right) obtained for an outflow static pressure $p_r = 20000\,\mathrm{Pa}$, showing three dominant flow directions

_____ streamlines resulted
from simulations
_ _ _ streamlines in potential flow
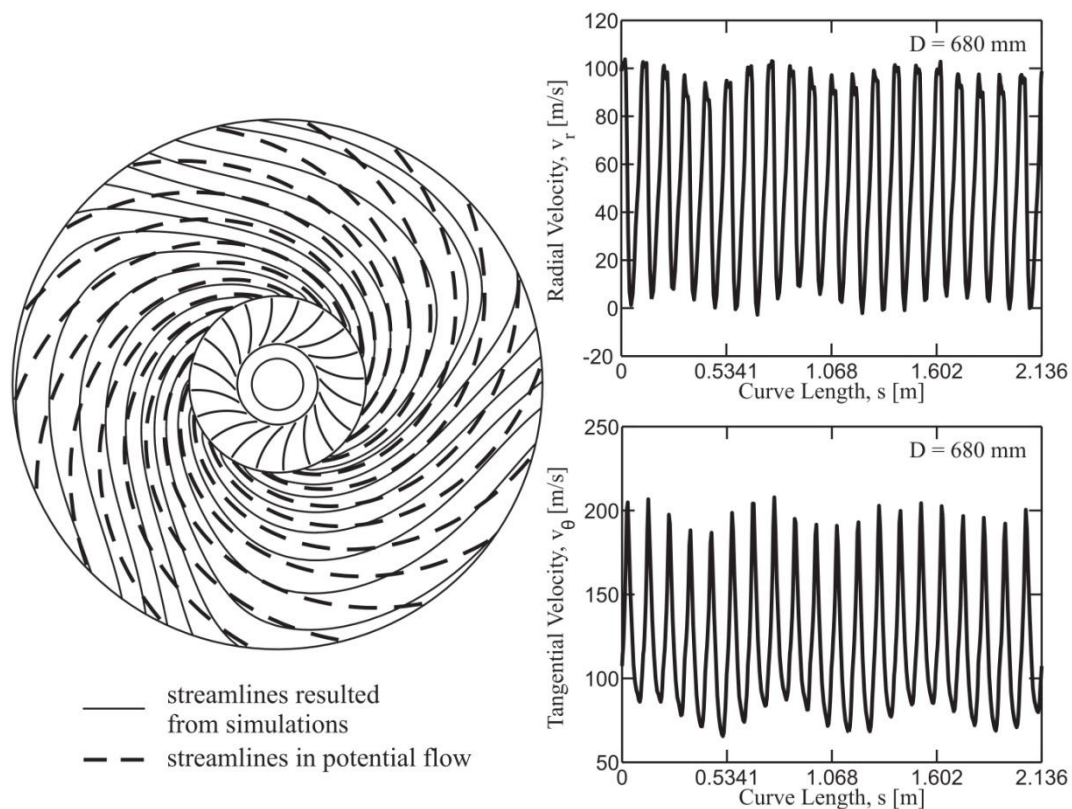
Fig. 4. Comparison between streamlines resulted from simulations at $p_r = 20000\,\text{Pa}$ and streamlines computed based on potential flow theory (left); velocity distributions resulted from simulations and used to compute the volume flow rate and the velocity circulation at a diameter of $680\,\text{mm}$ (right)

The circulation is given by the formula

$$\Gamma = \int_0^{\pi D} v_\theta \, \mathrm{d}s \,, \tag{5}$$

where v_θ is the tangential velocity obtained from simulations at diameter D. The flow rate and the circulation were computed at the interface between impeller zone and outflow zone. This interface is located at diameter $D = 680\,\text{mm}$, very close to impeller. By integrating the velocity distributions resulted from simulations at $p_r = 20000\,\text{Pa}$ and presented in Figure 4, $Q \approx 110.9\,\text{m}^3/\text{s}\cdot\text{m}$ and $\Gamma \approx 255.6\,\text{m}^2/\text{s}$ were obtained. With these values of Q and Γ, 20 equaly spaced streamlines of the potential flow were computed. These analitical streamlines are compared in Figure 4 with streamlines obtained numerically. It can be noticed that close to impeler a very good agreement exists between the two families of streamlines.

Subsequent simulations that were continued from the configuration with three dominant directions obtained at $p_r = 20000\,\text{Pa}$ showed that the number of dominant directions, i.e. three directions, remained unchanged for p_r values in the range $16000 \ldots 24000\,\text{Pa}$.

The image of the flow induced by the impeller changed after the outflow static pressure was increased from $24000\,\text{Pa}$ to $25000\,\text{Pa}$ and the flow rate became stable: the three dominant directions were replaced by only two dominant directions. As the outflow static pressure was further increased, this flow configuration remained unchanged up to $p_r = 29000\,\text{Pa}$. The flow configuration with two dominant directions is depicted in Figure 5 by a contour plot of the velocity magnitude and streamlines obtained for $p_r = 28000\,\text{Pa}$. With the two dominant directions spaced at $180°$, the flow possesses a two-fold rotational symmetry with respect to impeller axis.

For values of p_r between $30000\,\text{Pa}$ and $32000\,\text{Pa}$ the three dominant directions reappeared (Fig. 6). Finally, close to the limit of reversed flow, at $p_r = 33000\,\text{Pa}$ and $p_r = 34000\,\text{Pa}$, the results indicated again flow configurations with only two dominant directions (Fig. 7).

The first set of results described above indicate flow configurations with either three or two
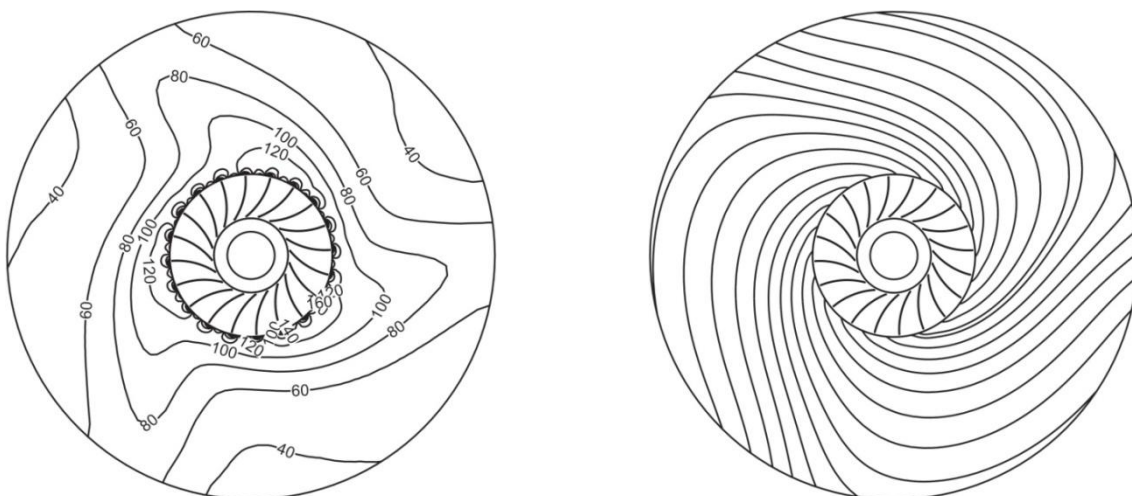
Fig. 5. Contours of absolute velocity in m/s (left) and streamlines (right) obtained for an outflow static pressure $p_r = 28000$ Pa, showing two dominant flow directions


Fig. 6. Contours of absolute velocity in m/s (left) and streamlines (right) obtained for an outflow static pressure $p_r = 30000$ Pa, showing (again) three dominant flow directions
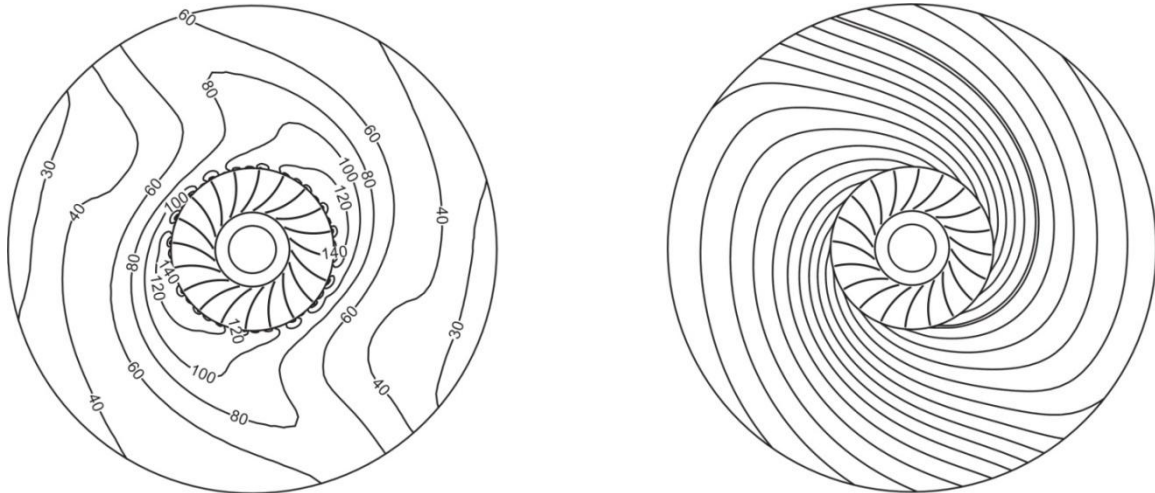

Fig. 7. Contours of absolute velocity in m/s (left) and streamlines (right) obtained for an outflow static pressure $p_r = 34000$ Pa, showing two dominant flow directions
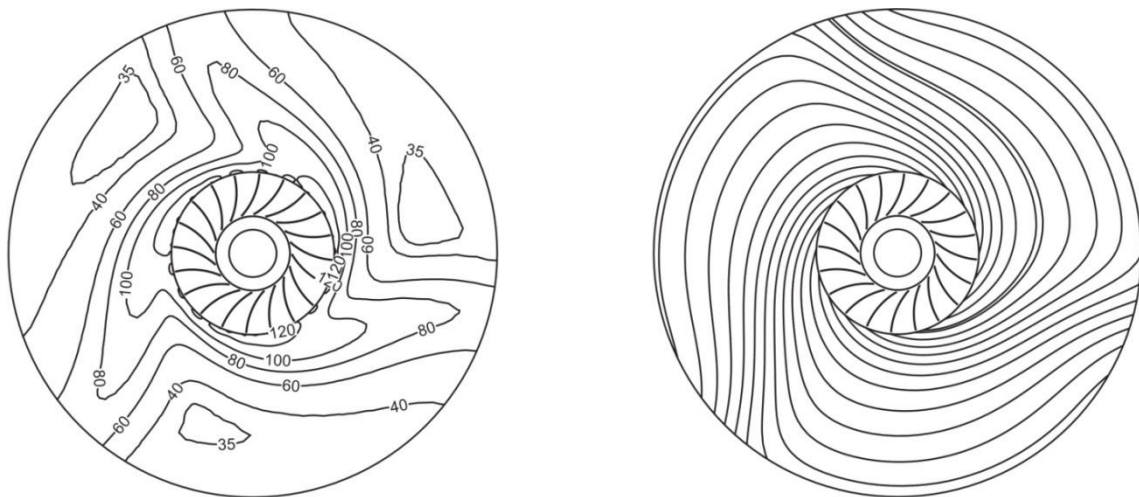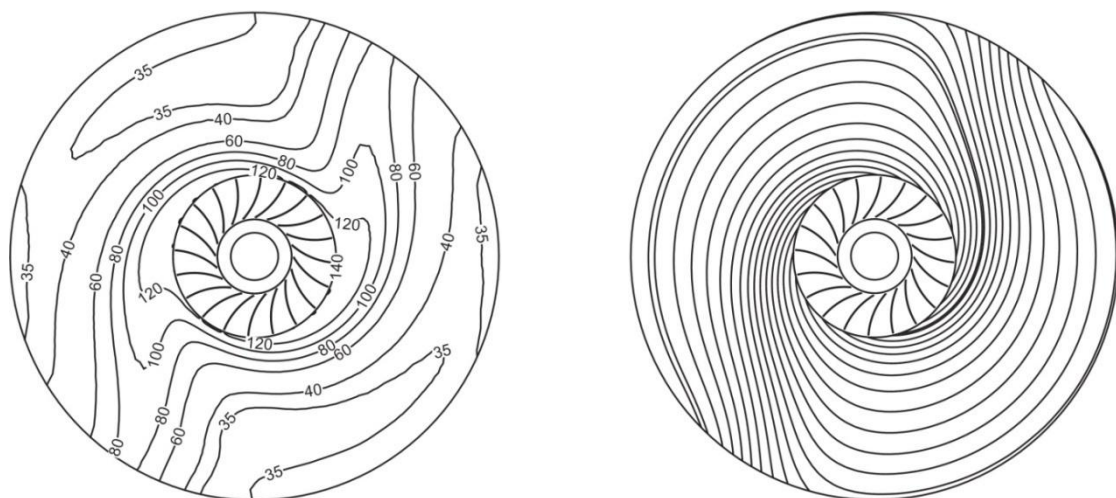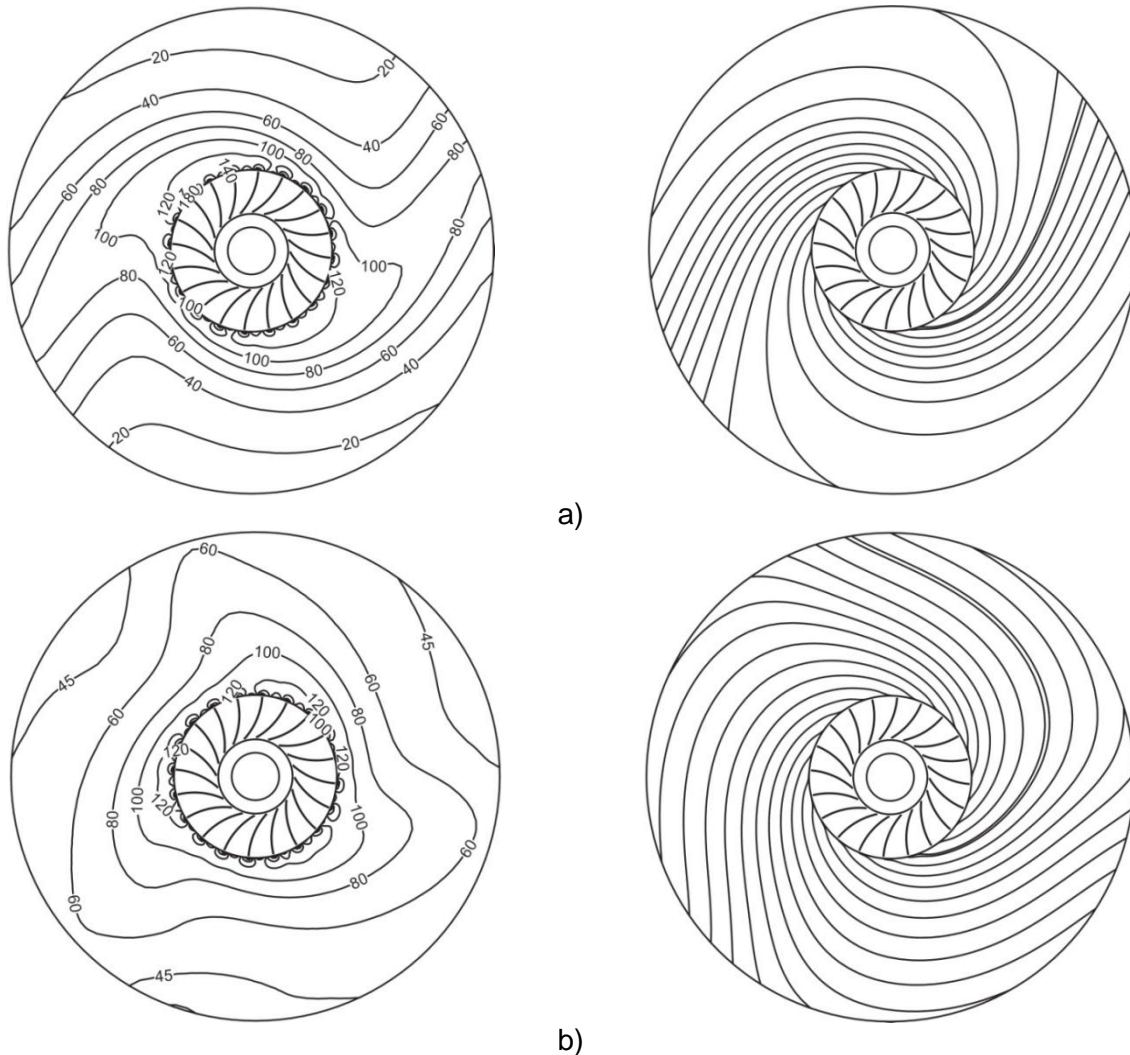
a)

b)

Fig. 8. Contours of absolute velocity in m/s (left) and streamlines (right) obtained for an outflow static pressure $p_r = 34\,000\,\text{Pa}$, showing two dominant flow directions

dominant directions, depending on the working regime of the impeller, characterized by the outflow static pressure p_r. To verify these results, new simulations were started from the last solution obtained for the outflow static pressure of $34\,000\,\text{Pa}$. The new set of simulations was continued by decreasing p_r stepwise by $1000\,\text{Pa}$. Down to $p_r = 25\,000\,\text{Pa}$, the new results showed no change in the flow configurations by comparison with those obtained previously. A change appeared only when p_r was decreased from $25\,000\,\text{Pa}$ to $24\,000\,\text{Pa}$. Instead of observing a switch from two dominant directions to three directions, as expected based on the previous results, the flow preserved its two dominant directions down to $p_r = 16\,000\,\text{Pa}$. In other words, when decreasing the outflow static pressure below $30\,000\,\text{Pa}$ in small steps only flow configurations with two dominant directions can be obtained. Figure 8 presents for comparison contours of absolute velocity and streamlines showing two flow configurations, both obtained at the same outflow static pressure $p_r = 24\,000\,\text{Pa}$.

A third set of results was obtained by increasing the outflow static pressure starting from the solution showing two dominant flow directions resulted for $p_r = 16\,000\,\text{Pa}$ in the second set of simulations. The flow configuration remained unchanged, with two dominant directions, up to $p_r = 29\,000\,\text{Pa}$, it changed to three dominant directions for p_r between $30\,000\,\text{Pa}$ and $32\,000\,\text{Pa}$ and then back to two directions for p_r between $33\,000\,\text{Pa}$ and $34\,000\,\text{Pa}$.

The fact that below $p_r = 25\,000\,\text{Pa}$ two flow configurations are possible indicates that a bifurcation point exists between $p_r = 24\,000\,\text{Pa}$ and $p_r = 25\,000\,\text{Pa}$. The results presented above are
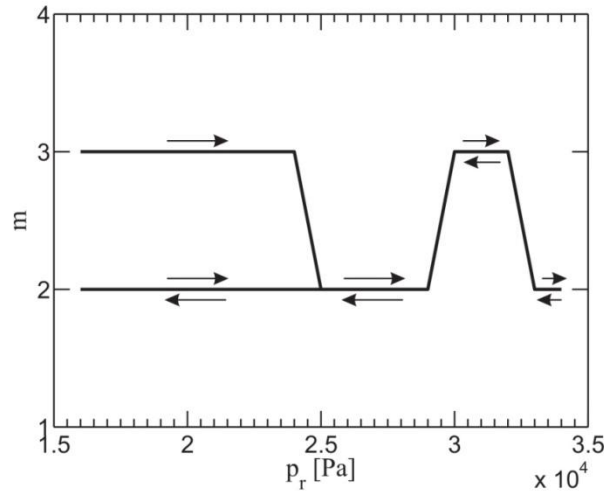
Fig. 9. Bifurcation diagram

summarized in the form of a bifurcation diagram in Figure 9. The diagram shows the number of flow directions, m, depending on the outflow static pressure p_r. According to the results, the branch corresponding to $m = 2$ can be traversed in both directions as long as the outflow static pressure changes in small steps. According to our results, if only small pressure changes are applied, close to the bifurcation point flow configurations with tree dominant directions evolve in flow configurations with two directions but flow configurations with two directions cannot evolve in flow configurations with three directions.
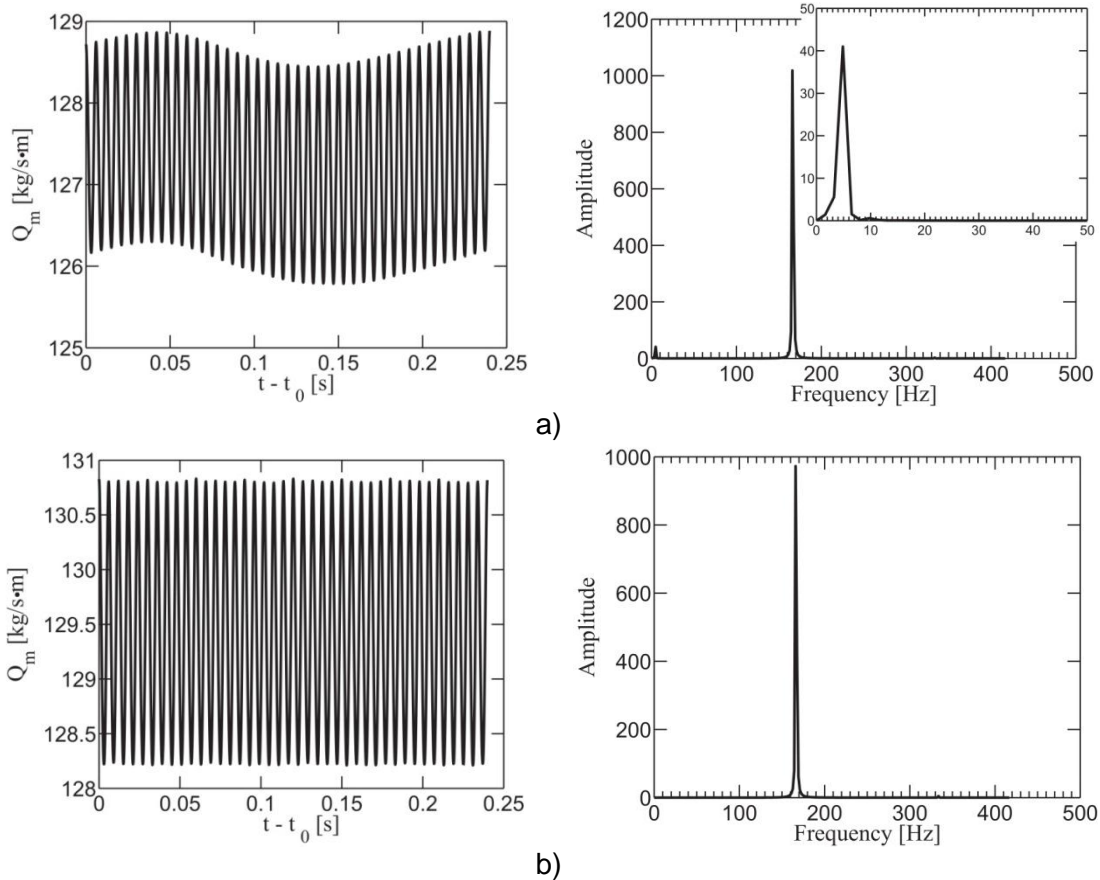
Fig. 10. Mass flow rate variations and their frequency spectra at outflow for 1600 time steps (20 full rotations) resulted at $p_r = 24\,000\,\mathrm{Pa}$ when the flow shows: a) two dominant directions and b) three dominant directions

Fig. 11. Contours of static pressure in Pa and circumferential pressure variations at three diameters inside the impeller ($D = 400$ mm, $D = 500$ mm, and $D = 600$ mm) resulted at $p_r = 24\,000$ Pa when the flow shows two dominant directions

The evolution in time of the mass flow rate Q_m at outflow changes depending on the flow configuration. The change is depicted in Figure 10 which shows time variations of Q_m and the frequency spectra of these variations obtained for $p_r = 24\,000$ Pa. It can be seen that, when the flow has two dominant directions, the mass flow rate has two modes of oscillation. For three dominant directions only one mode of oscillation is evident. In both cases, the first mode of oscillations has a frequency of 166.66 Hz, which is twice the rotational frequency of the impeller. For the flow with two dominant directions, the value of the first oscillation frequency could be related to the fact that, during a full revolution of the impeller, each blade interacts twice with the dominant flow directions. However, this explanation is no more valid for the flow with three dominant directions, which makes us to assume that the flow rate oscillations are caused by a more complex mechanism which probably includes the effect of the dominant flow directions and, also, the air compressibility. Another observation is that the configuration of the flow has also an influence on the average mass flow rate delivered by the impeller. For $p_r = 24\,000$ Pa the value of the average flow rate equals 127.3 kg/s · m when the flow shows two dominant directions and 129.5 kg/s · m when the flow has three directions, the relative difference being of about 1.7%. The bifurcation of the flow solutions could, therefore, offer an explanation for the small hysteresis of the characteristic curve observed in some cases when testing pneumatic turbomachines.

It is expected that the development of dominant flow directions outside the impeller has an influence on the flow inside the impeller. Of interest is especially the pressure, since pressure pulsations are among the causes for vibrations and aerodynamically generated noise in fans. Therefore, the pressure field was examined both for the configuration with two dominant flow directions and for the configuration with three directions. The configurations are those obtained for
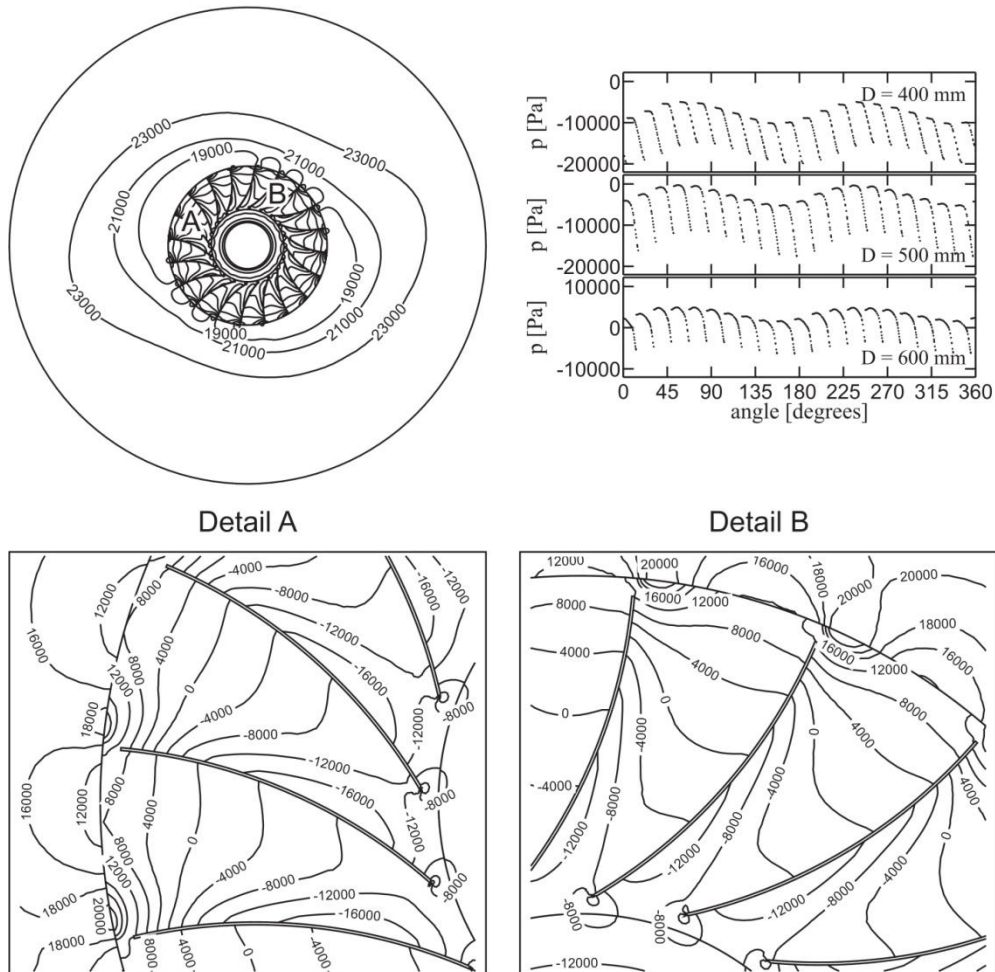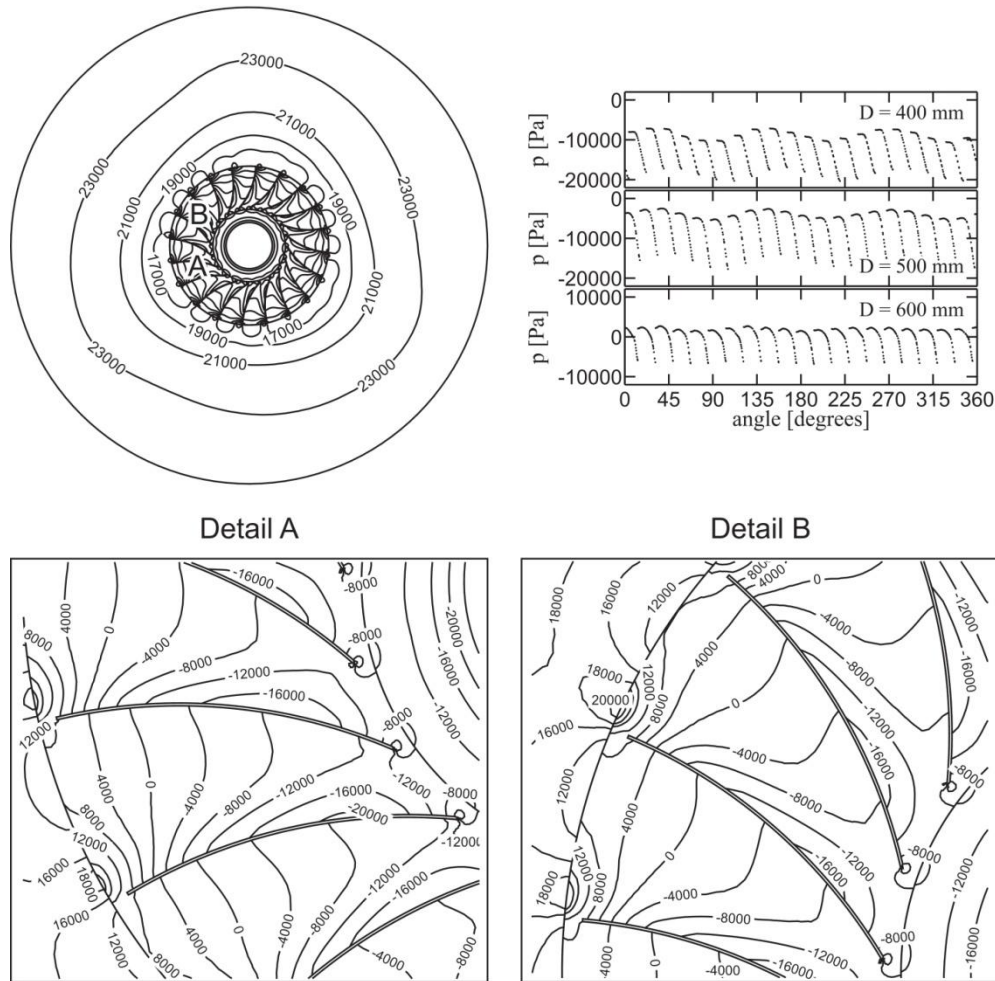
Fig. 12. Contours of static pressure in Pa and circumferential pressure variations at three diameters inside the impeller ($D = 400$ mm, $D = 500$ mm, and $D = 600$ mm) resulted at $p_r = 24\,000$ Pa when the flow shows three dominant directions

an outflow static pressure of $24\,000$ Pa. Figures 11 and 12 present circumferential pressure variations inside the impeller and pressure contours plotted inside blade channels which, at a certain time moment, either are aligned with a dominant flow direction or lie between two directions. The pressure distributions on the pressure sides and on the suction sides of the blades show noticeable changes as a blade crosses a dominant direction and then moves at angular positions between two dominant directions. These changes are also made evident by the diagrams of circumferential pressure variations, which show that during a full revolution of the impeller the blades undergo pressure pulsations, the number of maxima and minima being equal to the number of dominant flow directions. This shows that the dominant flow directions do not lie only outside the impeller, but extend inside it. The flow configuration outside the impeller influences the pressure pulsations, which are of lower amplitude when the flow exhibits three dominant directions. Therefore, the flow configuration with three dominant directions could be more desirable.

4. Conclusions

In this paper the compressible turbulent flow induced by a free impeller of a high pressure fan was investigated by means of numerical simulations. According to the results obtained, the flow outside the impeller is not axisymmetrical, but possesses either two or three dominant flow directions, depending on the boundary conditions. There is a certain similarity between the flow configuration presented in this paper and those observed by Poncet and Chauve for the flow induced by a disc rotating inside a fixed shroud. In a certain range of boundary conditions the flow solutions bifurcate, both flow configurations being possible. Based on the results, a bifurcation diagram was plotted.

The time variations of the mass flow rate delivered by the impeller are visibly influenced by the flow configurations. In the range of bifurcating solutions, the values of the average mass flow rate differ depending on the flow configuration. This fact could explain, at least partly, the small hysteresis of the characteristic curves obtained when testing some pneumatic turbomachines. The dominant flow directions extend inside the impeller, causing pressure pulsation on the blades. The flow instability investigated in this paper could therefore be an additional explanation for vibrations and aerodynamically generated noise inside pneumatic turbomachines.

References

[1] ISO 13349:2010, "Fans – Vocabulary and definitions of categories", ISO, 2010;
[2] EUROVENT 1/1, "Fan Terminology", EUROVENT/CECOMAF, 1984;
[3] G. Ioos, D.D. Joseph, "Elementary stability and bifurcation theory", 2nd Edition, Springer, New York, 1990;
[4] W. Cherdron, F. Durst, J.H. Whitelaw, "Asymmetric flows and instabilities in symmetric ducts with sudden expansion", Journal of Fluid Mechanics, 84, 1978, pp. 13–31;
[5] R.M. Fearn, T. Mullin, K.A. Cliffe, "Nonlinear flow phenomena in a symmetric sudden expansion", Journal of Fluid Mechanics, 211, 1990, pp. 595–608;
[6] J. Mitzushima, Y. Shiotani, "Transitions and instabilities of flow in a symmetric channel with a suddenly expanded and contracted part", Journal of Fluid Mechanics, 434, 2001, pp. 355–369;
[7] Dragomirescu, "Flow configurations in a lid driven cavity with throughflow", University Politehnica of Bucharest Scientific Bulletin, Series D: Mechanical Engineering, 66, 2–4, 2004, pp. 137–148;
[8] S. Poncet, M.P. Chauve, "Shear-layer instability in a rotating system", Journal of Flow Visualization and Image Processing, 14, 2007, pp. 85–105;
[9] A. Ciocanea, "Numerical Study on the Fluid Motion Induced by a Rotating Disk Inside a Vessel", Hidraulica, 4, 2013, pp. 65–69;
[10] Pfleiderer, H. Petermann, "Strömungsmaschinen", 4th Edition, Springer, Berlin, 1991;
[11] T.J. Chung, Computational Fluid Dynamics, Cambridge University Press, 2002;
[12] H.D. Baehr, K. Stephan, "Wärme- und Stoffübertragung", 3rd Edition, Springer, Berlin, 1998;
[13] H.K. Versteeg, W. Malalasekera, "An Introduction to Fluid Dynamics – The Finite Volume Method", Longman Scientific and Technical, London, 1996;
[14] F.S. Lien, M.A. Leschziner, "Assessment of Turbulent Transport Models Including Non-Linear RNG Eddy-Viscosity Formulation and Second Moment Closure", Computers and Fluids, 23, 8, 1994, pp. 983–1004;
[15] B.E. Launder, "Second-Moment Closure and Its Use in Modeling Turbulent Industrial Flows", International Journal for Numerical Methods in Fluids, 9, 1989, pp. 963–985;
[16] B.E. Launder, D.B. Spalding, "The Numerical Computation of Turbulent Flows", Computer Methods in Applied Mechanics and Engineering, 3, 1974, 269–289.

A Review of Design of Stirling Engines

Assistant Professor **Sunny NARAYAN**[1]

[1] Indus International University, Himachal Pradesh, India, rarekv@gmail.com

Abstract: *This work provides a review of n solar-powered Stirling engines devices. Previous works have focussed on the solar powered as well as low temperature differential engines. The aim of this work is to review working fluids for operation of this engine. Air was found to be a good alternative as a working medium for gamma type engines.*

Keywords*: Stirling Engines*

1. Introduction

In a Stirling engine the fluid is contained in a confined space, hence there are no problems of contamination. In order to reduce the heat losses, the mass flow rate must be low which can be maintained by low viscosity fluid or high working pressures. These engines are 30 to 40% efficient in a temperature range of 923–1073 K.[1].
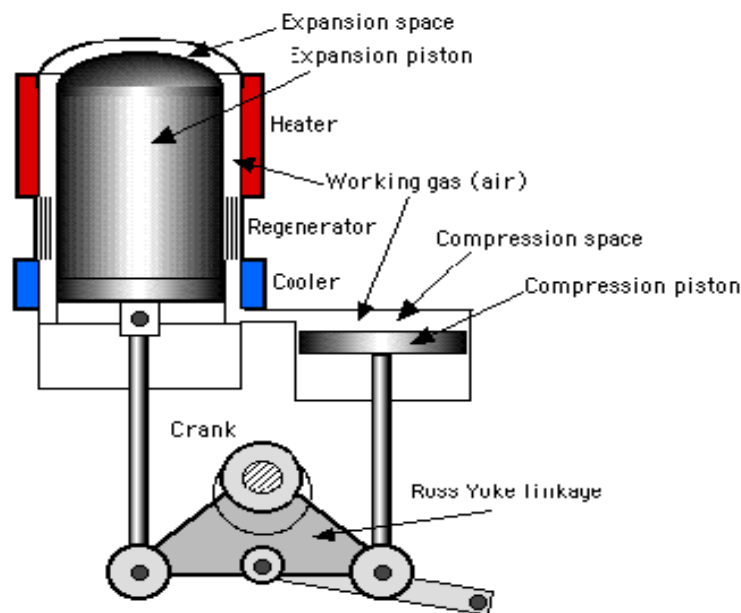
Fig. 1. Stirling engine [2]

A Stirling engine consists of following components:

1. **Heat source**-as fuel does not come in direct contact with the working fluid, Stirling engines can work on fluids which may damage parts of a conventional engine.
2. **Regenerator**-the function of regenerator is to use the waste heat from being lost to environment by storing it temporarily, thus helping to achieve high efficiencies close to an ideal Carnot cycle. A simple configuration consists of fine mesh of metallic wires. In an ideal Stirling cycle, the connecting space between hot and cold ends acts as regenerator.
3. **Heat sink**-typically the ambient environment acts as an ideal heat sink; otherwise the cold side can be maintained by iced water or cold fluids like liquid nitrogen.
4. **Displacer piston**-it causes the displacement of working gas between hot and cold regions so that expansion and contraction occurs alternatively for operation of engine.
5. **Power piston**- transmits the pressure to crankshaft.

In a Stirling engine, hot air expands when heated and contracts when cooled. This principle of operation was most properly understood by Irish scientist Robert Boyle from his results on experiments on air trapped in a J shaped glass tube. Boyle stated that pressure of a gas is inversely proportional to its volume and product of pressure and volume occupied is a constant depending on temperature of gas.

Hence PV=NRT

Various assumptions which are made in this cycle are [3]:

1) Working fluid is an ideal gas.

2) Conduction and flow resistance is negligible.

3) Frictional losses are neglected.

4) Isothermal expansion and contraction.

This cycle can be described by following stages: [3]

1) Phase C-D: Isothermal expansion-the working fluid undergoes an isothermal expansion absorbing the heat from source. The power piston moves out, hence increasing the volume and reducing the pressure. The work done in expansion of gas is given by:

$$We = RTln\left[\frac{V_D}{V_C}\right] = \int pdv = nRTc\ ln\left[\frac{V_D}{V_C}\right] \tag{1}$$

2) Phase D-A: Power piston now reaches the outermost position and stays there so that volume is constant. The working fluid is passed through the regenerator where it gives up heat for use in next cycle. Hence its temperature and pressure falls. No work is done during this phase.

3) Phase A-B: The power piston stats moving inwards, reducing its volume and increasing its pressure the working fluid gives up heat to cold sink. The work done in compressing the gas is given by:

$$Wc = RTln\left[\frac{V_B}{V_A}\right] = \int pdv = nRTh\ ln\left[\frac{V_B}{V_A}\right] \tag{2}$$

4) Phase 2-3: The power piston is at its most inwards point and stays there to keep volume constant. Working fluid passes again through the regenerator, recovering the heat lost in 2nd phase, hence its pressure and temperature goes up.

$$Wnet = We - Wc$$

$$= nR[Th - Tc]\left[\frac{Vmax}{Vmin}\right] \tag{3}$$

But

$$V_B = V_C\ \&\ V_A = V_D$$

$$efficiency\ of\ engine = \eta = \frac{Wnet}{Qe} = \frac{nR(Th - Tc)\ln\left[\frac{Vmax}{Vmin}\right]}{nR\ Th\ \ln\left[\frac{Vmax}{Vmin}\right]}$$

$$\eta = \frac{Th-Tc}{Th} \tag{4}$$

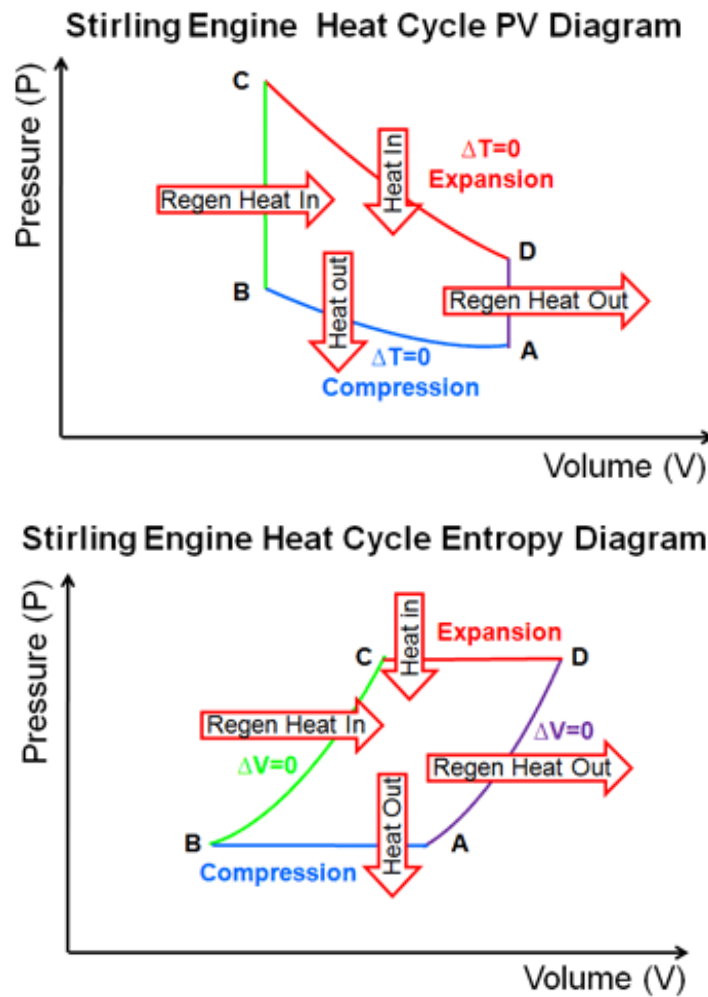**Fig. 2.** P-V & T-S plot of a Stirling cycle [4]

In Stirling cycle, two Isochoric processes replace the two Iso-entropic processes s in an ideal Carnot cycle. Hence more work is available than a Carnot cycle as net area under P-V curve is more. Thus there is no need for high pressures or swept volumes. This can be seen in the figures presented below.
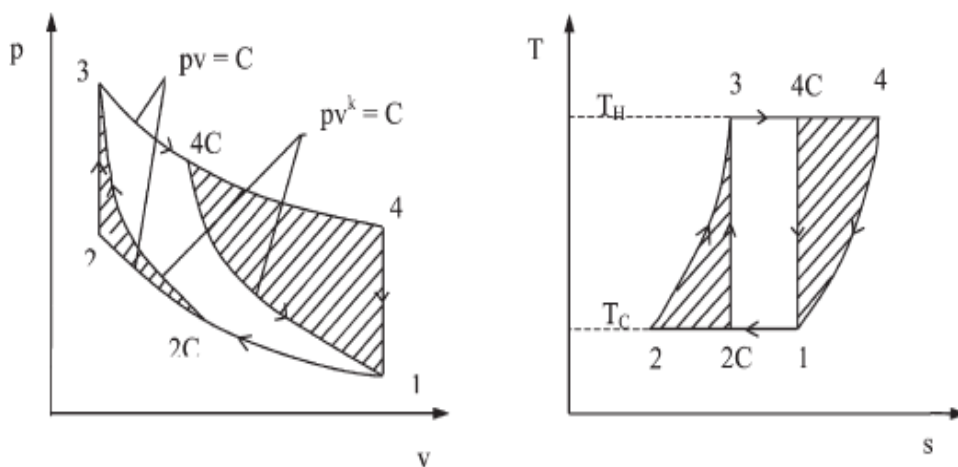
Fig. 3. Comparison of Stirling cycle and Carnot cycle [5]

2. Types of engines [6]

Stirling engines can be further classified as alpha, beta or gamma type. Alpha version consists of two power pistons in series with heat sink, heat source and regenerator.
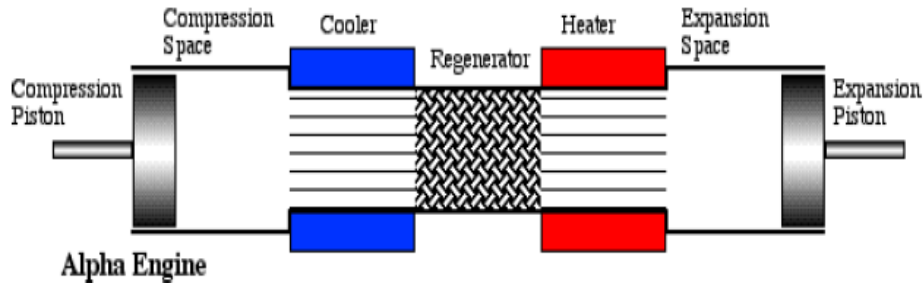
Fig. 4. An Alpha Stirling engine configuration

2.1 Working of an Alpha Stirling engine [6]

This engine consists of following stages:
1) Expansion-working gas is present in hot side and gains heat expanding, hence pulling both pistons inwards.
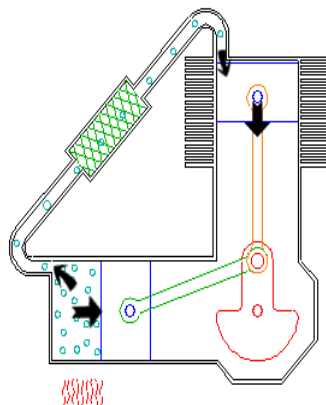
Fig. 5. Working stages of an Alpha Stirling Engine

2) Transfer Motion of crank shaft transfers most of the gas from hot side towards the cold side.
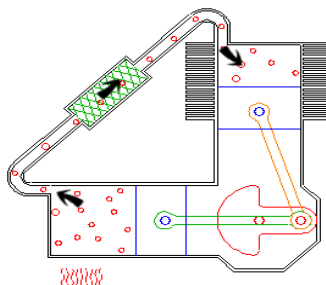
Fig. 6. Working stages of an Alpha Stirling Engine

3) Contraction-Working gas is transferred towards cold side, cools and contacts pushing both pistons outwards.
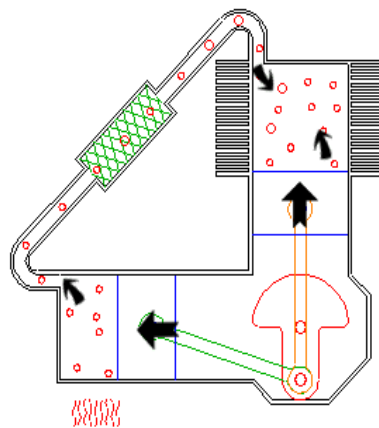
Fig. 7. Working stages of a Alpha Stirling Engine

4) Transfer-Motion of crank shaft through 90° causes transfer of gas again to hot side so that cycle is repeated again.
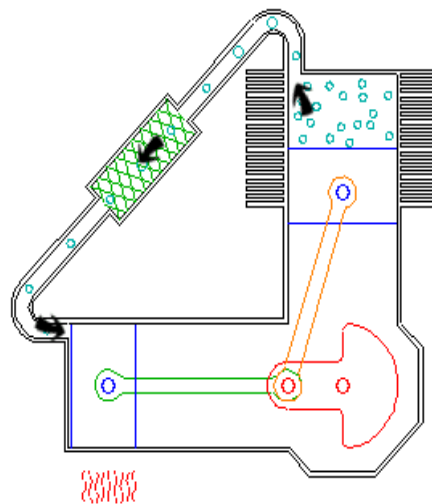
Fig. 8. Working stages of a Alpha Stirling Engine [16]

2.2 Working of a Beta Stirling engine [6]

Beta type engine and gamma type engine have a single power piston, whereas alpha type engine have two power pistons. Beta type Stirling engine has both power and displacer pistons on the same axis whereas in gamma configuration, both pistons are separate. Gamma engines are best suited for studies whereas Beta ones are difficult to fabricate.
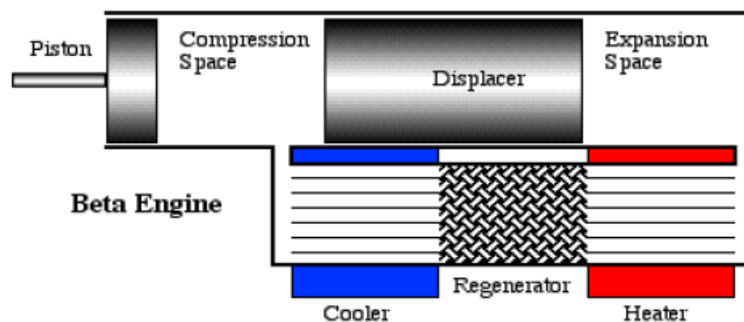
Fig. 9. A Beta Stirling engine

Working of a beta engine can be understood in following cycles:
1) Expansion-most of the gas is at the hot end, which gains heat and expands.
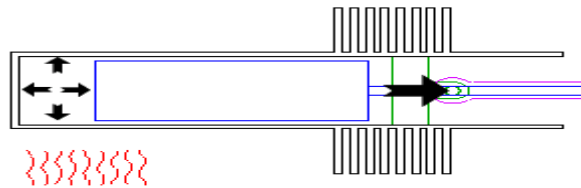
Fig. 10. Working stages of a Beta Stirling Engine

2) Transfer-motion of fly wheel causes gas to move towards cold end passing over the displacer.
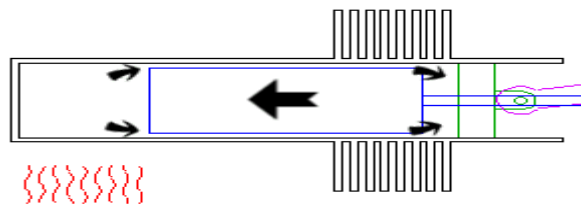
Fig. 11. Working stages of a Beta Stirling Engine

3) Contraction-most of the gas is in cold end where it cools and contracts drawing piston inwards.
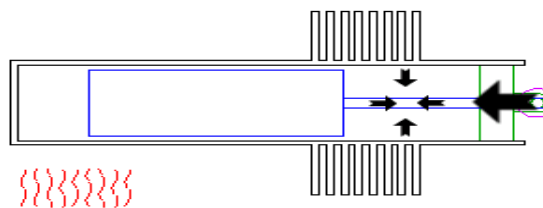
Fig. 12. Working stages of a Beta Stirling Engine

4) Transfer-motion of flywheel causes displacer to move out, transferring gas again to hot end.
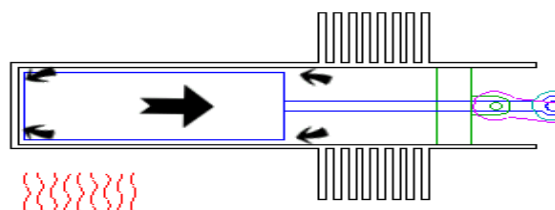
Fig. 13. Working stages of a Beta Stirling Engine
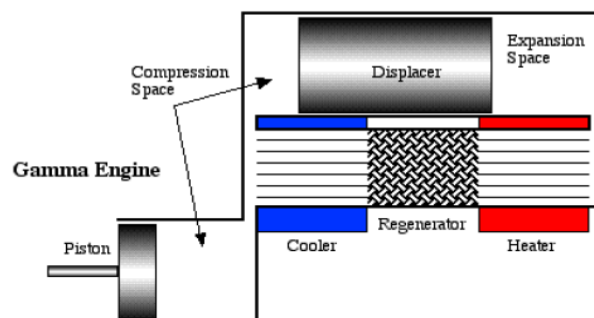
Fig. 14. A Gamma Stirling engine

3. Working gas

It is a gas on which engine operates. There are several gases that can be used to run a Stirling engine. Lighter gases having atomic mass lesser than that of air have higher specific heat and gas constant and lower viscosity resulting in lesser viscous losses and higher heat storing capacity [7].This can be seen in the following graph which was obtained by simulation by Philip Brothers.
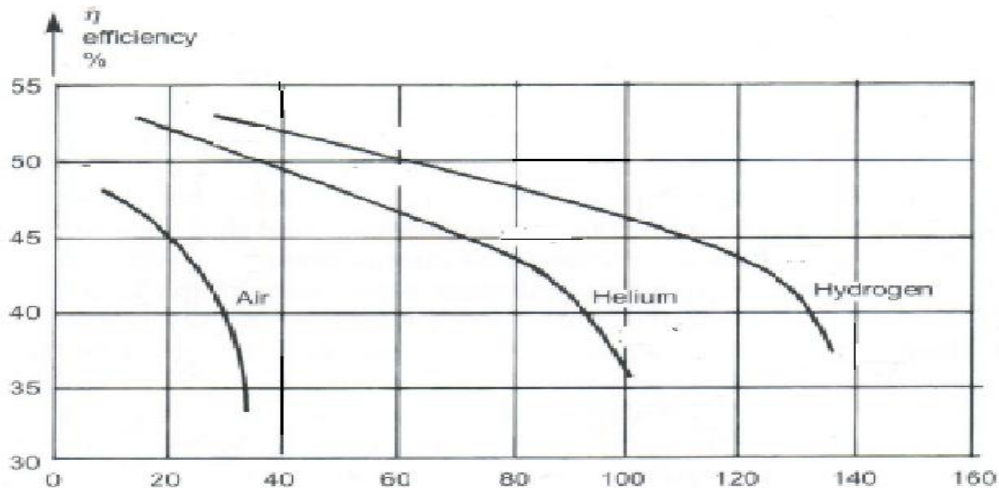
Fig. 15. Stirling engine efficiency V/S power output for various gas [8]

4. Pros and cons of Stirling engine

Stirling engine has some merits as well as demerits which are discussed below

1) Merits
A) Stirling engines can be run on wide variety of fuels including solar energy without need for fuel to come in contact with operating gas hence avoiding containment. Hence even if solar energy is unavailable, alternative fuels can be used for operations. Thus these devices are not susceptible to fuel shortage.
B) Low and noise less operations are possible. Hence suitable for submarines.
C)Lower maintenance is needed and combustion of fuel occurs outside the engine.
D) Can be used as a CHP unit.
E) No danger of explosion as in steam engines.
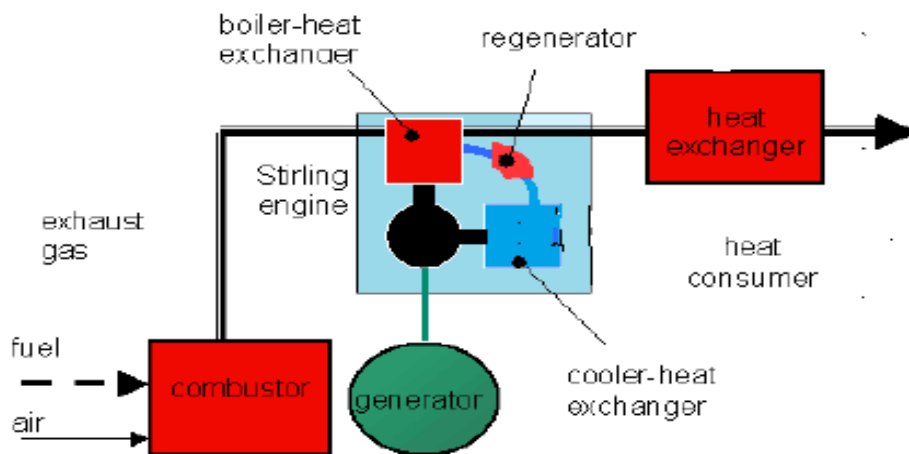
Fig. 16. A CHP Stirling engine

2) Demerits
A) Commercial feasibility not possible on large scale manufacturing.
B) Takes time to start from the cold.

5. Low temperature difference Stirling engine

These engines can run at a typically low temperature difference of less than 100°C between hot and cold end .with high temperature difference between hot and cold end, it is necessary to maintain long separation between hot and cold ends where as area of heating and cooling is less important. In year 1980 Sneft and Kolin developed of simple versions of such engines where a cup of hot tea could be used as a heat source. The upcoming figures show clear distinguish between the LTD &HTD engines.
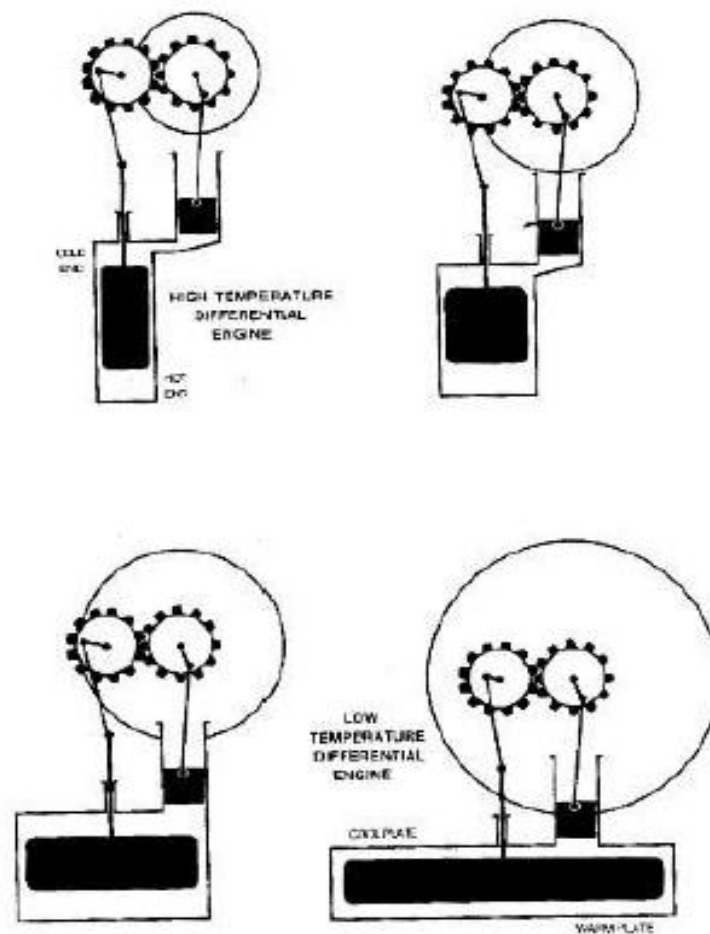
Fig. 17. Comparison of LTD and HTD engines [9]

6. Conclusions

This work reviews research works done in field of technology of Stirling engines, solar-powered Stirling engines, and LTD Stirling engines. The keys ways to improve the efficiency of the engine is to device new materials for good heat transfer to the working fluid. Lower viscosity working fluid pumped at higher pressure is ideal condition for good heat transfer. The efficiency of Stirling engine may be low, but it has high reliability and low setup costs.
For use in rural areas reflector can be used to focus the solar energy on a displacer hot-end surface for heat transfer by conduction to the air inside the displacer cylinder. The air expands and moves the power piston which in turn can be useful for mechanical power output.

References

[1] Stine WB. Stirling engines. In: Kreith F, editor. The CRC handbook of mechanical engineers. Boca Raton: CRC Press; 1998. p. 8-7–8-6.
[2] Van Arsdell BH. Stirling engines. In: Zumerchik J, editor. Macmillan Encyclopedia of Energy, vol.3. Macmillan Reference USA; 2001. p. 1090–95.
[3] Senft JR. Ringbom Stirling engines. New York: Oxford University Press, 1993.
[4] Walpita SH. Development of the solar receiver for a small Stirling engine. In: Special study project report no. ET-83-1. Bangkok: Asian Institute of Technology; 1983.
[5] Rizzo JG. The Stirling engine manual. Somerset: Camden miniature steam services, 1997.
[6] Howell JR, Bannerot RB. Optimum solar collector operation for maximizing cycle work output. Sol Energy 1977;19:149–53.
[7] Schmidt G. Theorie der Lehmannschen calorischen maschine. Zeit Des Vereines deutsch Ing 1871;15(1-12):97–112.
[8] Martini WR. Stirling engine design manual. 2nd ed. NASA CR-168088; 1983.
[9] West CD. Principles and applications of Stirling engines. New York: Van Nostrand Reinhold, 1986.

Liquid Film Adhesion in Contact between Rough Surfaces

PhD. stud. Eng. **Amir ROSTAMI**[1], Prof. PhD. Eng. **Jeffrey L. STREATOR**[2]

[1] Georgia Institute of Technology, amir.rostami@gatech.edu

[2] Georgia Institute of Technology, jeffrey.streator@me.gatech.edu

Abstract: Many micro and nano scale devices are influenced by the presence of liquid at the interface between contacting surfaces. Such liquid may induce large and undesired adhesive or "stiction" forces. In some cases, liquid may find its way into the interface of two rough surfaces that are already in contact. It is of interest to model the manner in which the interface proceeds to a new equilibrium configuration upon introduction of the liquid. Such a process involves interactions among viscosity, elasticity and capillarity. To simulate such effects, a contact model is employed to account for surface deformation, a mixed-lubrication model is applied to analyze liquid flow and the Young-Laplace equation is implemented at the boundary of the wetted region to provide the capillary pressure. Calculations are performed to reveal the roles of liquid viscosity, liquid surface tension, surface roughness and elastic modulus on the generation of adhesive forces.

Keywords: Capillary flow, Surface roughness, Liquid-mediated adhesion

1. Introduction

Many natural and engineered systems involve a thin liquid film between two solid surfaces. Familiar examples in nature include: plants and trees, which transport fluid from roots to leaves in opposition of gravity through xylem conduits [1]; and soils whose strength characteristics depend on the way water interacts between solid particles [2]. Among engineered systems, there are several small scale devices for which liquids are present in confined regions during fabrication or during operation [3, 4]. In many cases, the presence of the liquid film causes excessive adhesive forces and device failure [5, 6]. On the positive side, in the operation of nanofluidic devices, capillary forces operating in submicron channels are used to pump liquids from one location to another [7, 8]. In this work, a model for the capillary flow between two nominally flat rough surfaces is presented. The current model represents an extension to the previous published models of liquid-mediated adhesion. Streator and Jackson [9] and Streator [10] presented 2D spectral and deterministic approaches, respectively, to model liquid-mediated adhesion between rough surfaces. Rostami and Streator extended the 2D liquid-mediated adhesion models to 3D models using a spectral approach [11, 12] and a deterministic approach [13]. These former analyses are restricted to static conditions (i.e., do not consider flow) and treats the free surface of the liquid in only an average sense namely that the film thickness at the periphery of the film is equated with the global average spacing between the surfaces.

2. Methodology

A schematic plot of the interface of interest is shown in Fig. 1. The wetting liquid spreads between an annular rigid flat punch and a rough disk until its radius, b, reaches the outer radius of the punch, r_o. The liquid is introduced at the inner radius of the punch, r_i, and the capillary effect is the driving force for the liquid flow. The large concave curvature at the free surface of the liquid causes a pressure drop across the free surface, which drives the liquid between the two surfaces. The pressure at the inner radius of the punch is ambient, and at the outer boundary of the liquid film, the negative pressure can be obtained from Laplace-Young relation [14]. The negative pressure within the capillary film induces tensile stresses in the interface. The compressive stresses arising at solid-solid contact spots oppose the tensile stresses due to capillary effects.
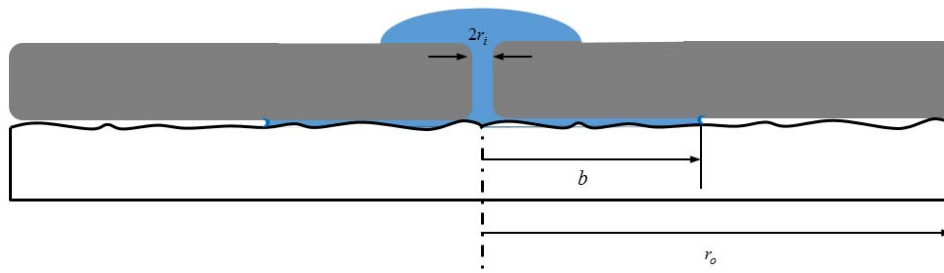
Fig. 1. Schematic depiction of the modeled interface.

In this work, a model is developed to study the capillary flow between the surfaces depicted in Fig. 1. The model is comprised of a macro-contact model, a micro-contact model and a mixed lubrication model. The macro-contact model is used to determine the pressure distribution within the nominal region due to external load acting on the contacting surfaces. In macro-contact model, the effect of surface roughness is neglected, so that the contacting surfaces are assumed to be smooth. The surface roughness effects are considered in the micro-contact model where the local gap is calculated. The hydrodynamic pressure distribution within the liquid flow due to the capillary effects is obtained from the mixed lubrication model. An iterative numerical algorithm is designed to solve the three sub-models simultaneously to obtain the results for the tensile force, liquid flow rate and local gap between the two contacting surfaces.

2.1 Macro-Contact Model

In the macro-contact model, the pressure distribution under a rigid annular punch deforming an elastic half-space is evaluated. A schematic view of this problem is shown in Fig 2. The pressure distribution and displacement field for the contact of an annular rigid punch and an elastic half space under external loading of P_{ext} can be obtained numerically via influence coefficients. The influence coefficients are derived from the analytical surface deformation solution of an elastic half-space under uniform pressure [15]. A finite radius of curvature is assumed for the edges of the rigid punch to avoid unbounded contact pressures. Results for the contact pressure distribution under a rigid punch with inner and outer radii of $r_i = 1\,\text{mm}$ and $r_o = 3\,\text{cm}$ respectively and with edge radius of $r' = 0.1\,\text{mm}$ under the penetration of $d = 0.1\,\mu\text{m}$ is given in Fig. 3.

Fig. 2. Illustration of surface deformation in a half-space deformed by an annular rigid punch.

Fig. 3. Pressure distribution under the rigid annular punch.

2.2 Macro-Contact Model

On a micro-level, all surfaces have some degrees of waviness or roughness. The pressure distribution from the macro-contact model along with the hydrodynamic pressure within the liquid flow cause surface deformation in the contacting rough disk at micro levels. In the current model, the Jackson and Streator (JS) multiscale model is used to model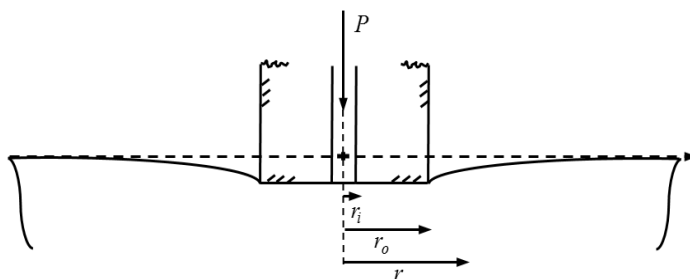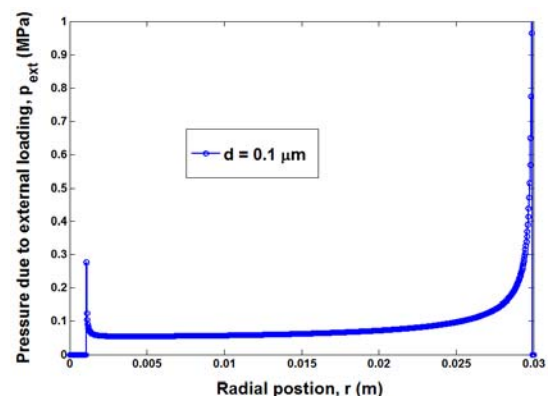 the contact at micro-scale level. The JS model is based on representing the rough surface in multi scales of roughness using the fast Fourier transform (FFT) of the surface heights. The rough surface data is generated employing a surface profile generation method outlined by Garcia and Stoll [16]. A two dimensional FFT is then performed on the generated surface heights to obtain the amplitude at each frequency level as is performed in [17]. At each frequency level, the asperities are modelled assuming a three-dimensional sinusoidal geometry. The relation between average gap and the average pressure at frequency level is given by [18]

$$\frac{\overline{g}_k}{\Delta_k} = \left(1 - \left(\frac{\overline{p}_k}{p_k^*}\right)^{1/2}\right)^{5/2} \qquad (1)$$

where is the amplitude of the sinusoidal-shaped asperity and is the complete contact pressure at frequency level. In the current model, the same volume-loss approach employed by Green et al. [17] is used to calculate the gap at each radial position.

2.2 Mixed Lubrication Model

A mixed lubrication model is used to determine the hydrodynamic pressure distribution within the liquid flow. An average Reynolds equation [19] for incompressible fluid in polar coordinates is used which is given by

$$\frac{\partial}{\partial r}\left(\varphi r h^3 \frac{\partial p_{hyd}}{\partial r}\right) + \frac{1}{r}\frac{\partial}{\partial \theta}\left(\varphi h^3 \frac{\partial p_{hyd}}{\partial \theta}\right) = 12\eta r \frac{\partial h}{\partial t} \qquad (2)$$

where r, θ are the radial and azimuthal directions, respectively, p_{hyd} is the hydrodynamic pressure, h is the film thickness or the local gap, $\varphi = 1 - 0.9e^{-0.56(h/\sigma)}$ is the pressure flow factor, and η is the dynamic viscosity of the working fluid. The second term in Eq. (2) disappears due to axisymmetric flow assumption. Also, it is assumed that the squeeze film effects is negligible (right-hand side of Eq. 2). Equation (2) along with the boundary conditions are solved numerically using Gauss-Seidel method to obtain the hydrodynamic pressure distribution.

3. Numerical Algorithm

A numerical algorithm is designed to solve the liquid flow problem. After introducing the input parameters (see Table 1), an initial value is selected for the radius of liquid flow, b_0. Next, the Reynolds equation is solved for the hydrodynamic pressure distribution. The sum of hydrodynamic pressure and pressure distribution due to external loading are inserted into the JS multiscale model to solve for the gap at each radial position. Then, a convergence test on tensile force is performed. In the lack of convergence, the updated values for radial gap is used in Reynolds equation to recalculate the hydrodynamic pressure distribution. When the convergence is acquired, the new value of b is calculated based on the relation between the pressure gradient and the rate of change of liquid flow radius $\left(\frac{\partial b}{\partial t} = -\frac{h_b^2}{12\eta}\frac{\partial p_{hyd}}{\partial r}\Big|_{r=b}\right)$.

TABLE 1: Reference properties

Name	Symbol	Value
Nominal domain radius	r_o	3 cm
Radius of entrance hole	r_i	1 mm
Edge radius	r'	0.1 mm
Effective elastic modulus	E'	50 GPa
Liquid surface tension	γ	72.7 mN/m
Liquid viscosity	η	0.89 mPa.s
r.m.s. surface roughness	σ	0.4 μm

4. Results

A set of results of the numerical algorithm for the reference properties given in Table 1 in the presence of external load $\left(P_{ext}=30N\right)$ is presented in this section. The results for the tensile force, F_t, and flow rate, Q, as the liquid spreads between the two surfaces as a function of time is shown in Figs. 4 and 5. The liquid flow starts at radius $b=b_0$ and flows until the radius reaches the outer radius of the domain $b=r_o$. As it can be seen, the tensile force increases with time while the flow rate decreases with time. The results for the maximum tensile force, $F_{t\,max}$ and the initial flow rate, Q_{b_0}, versus the external load are shown in Fig. 6. As it can be seen, the maximum tensile force increases with the external load while the flow rate decreases with the external load.
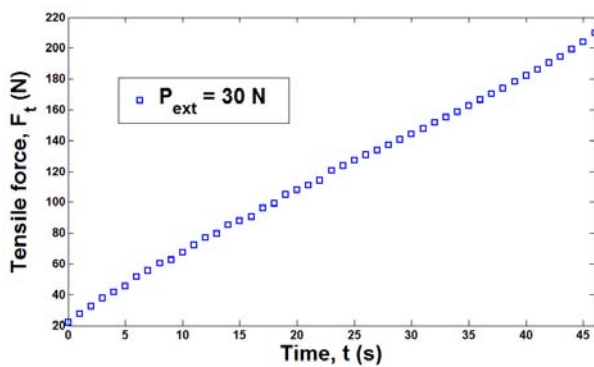

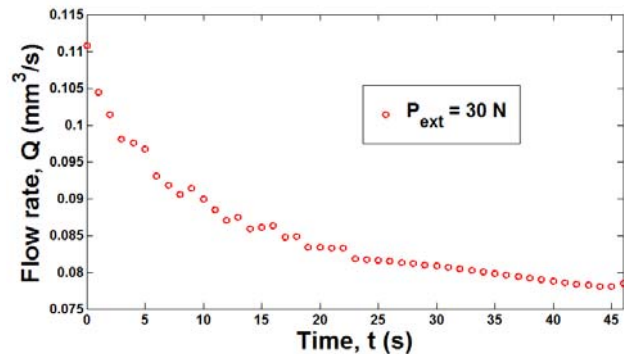**Fig.4.** The results for the tensile force versus time.

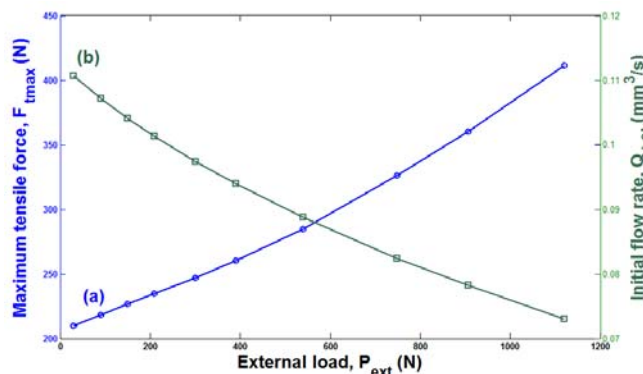**Fig.5.** The results for the flow rate versus time.

Fig.6. The results for (a) maximum tensile force, and (b) initial flow rate
versus the external load.

Conclusions

In this work, a numerical model for the liquid flow between two contacting rough surfaces due to capillary effects is presented. A contact model comprised of micro and macro level sub-models along with a mixed lubrication model are used to obtain the results. The results for the tensile force and flow rate are presented based on solving an iterative numerical algorithm. The results show that as the liquid spread between the two surfaces, the tensile force increases and flow rate decreases. The maximum tensile force increases as the external load is increased while the flow rate decreases with increasing external load.

References

[1] Tyree, M.T., 2003, "Plant hydraulics: the ascent of water," *Nature*, 423(6943), pp. 923-923.
[2] Fredlund, D.G., Rahardjo, H., 1993, "Soil mechanics for unsaturated soils," *John Wiley & Sons*.
[3] Maboudian, R., Howe, R.T., 1997, "Critical review: adhesion in surface micromechanical structures", *Journal of Vacuum Science & Technology B*. 15(1), pp. 1-20.
[4] Komvopoulos, K., 2003, "Adhesion and friction forces in microelectromechanical systems: mechanisms, measurement, surface modification techniques, and adhesion theory", *Journal of adhesion science and technology,* 17(4), pp. 477-517.
[5] Zhu, L., Xu, J., Zhang, Z., Hess, D.W., Wong, C., 2005, "Lotus effect surface for prevention of microelectromechanical system (MEMS) stiction," *Electronic Components and Technology Conference, 2005 Proceedings 55th: IEEE*, pp. 1798-1801.
[6] Hariri, A., Zu, J., Ben Mrad, R., 2007, "Modeling of wet stiction in microelectromechanical systems (MEMS)," *Microelectromechanical Systems, Journal of*, 16(5), pp. 1276-1285.
[7] Tas, N.R., Mela, P., Kramer, T., Berenschot, J., van den Berg, A., 2003 "Capillarity induced negative pressure of water plugs in nanochannels," *Nano Letters*, 3(1), pp. 1537-1540.
[8] Deleanu, L., 2011, "A simplified model for partial journal and water lubrication", *Hidraulica*, 1-2, pp. 71-77.
[9] Streator, J.L., Jackson, R.L., 2009, "A model for the liquid-mediated collapse of 2-D rough surfaces", *Wear,* 267(9), pp. 1436-1445.
[10] Streator, J.L., 2009, "A model of liquid-mediated adhesion with a 2D rough surface," *Tribology International*, 42(10), pp. 1439-1447.
[11] Rostami, A., Streator, J.L., 2014, "A Model for Capillary Flow between Rough Surfaces," *STLE Annual Meeting.*
[12] Rostami, A., Streator, J.L., 2015, "Study of liquid-mediated adhesion between 3D rough surfaces: A spectral approach," *Tribology International*, 84, pp. 36-47.
[13] Rostami, A., Streator, J.L., 2015, "A Deterministic Approach to Studying Liquid-Mediated Adhesion Between Rough Surfaces," *Tribology Letters,* 58(1), pp. 1-13.
[14] Adamson, A.W., Gast, A.P., 1967, "Physical Chemistry of Surfaces", *John Wiley & Sons*, New York.
[15] Johnson, K., 1985, "Contact mechanics," *Cambridge University Press.*
[16] Garcia, N., Stoll, E., 1984, "Monte Carlo calculation for electromagnetic-wave scattering from random rough surfaces," *Physical review letters*, 52(20), pp. 1798-1801.
[17] Green, C.K., Streator, J.L., Haynes, C., Lara-Curzio, E., 2013, "A Computational Leakage Model for Solid Oxide Fuel Cell Compressive Seals," *Journal of fuel cell science and technology*, 8(4), pp. 041003(1)-041003(9).
[18] Rostami, A., Jackson, R.L., 2013, "Predictions of the average surface separation and stiffness between contacting elastic and elastic–plastic sinusoidal surfaces," *Proceedings of the Institution of Mechanical Engineers, Part J: Journal of Engineering Tribology*, 227(12), pp. 1376-1385.
[19] Hamrock, B.J., Schmid, S.R., Jacobson, B.O., 2004, "Fundamentals of fluid film lubrication," *CRC press.*

Heat Transfer Performance Analysis in Porous Heat Exchanger

Assistant professor PhD. eng. **Petre OPRIŢOIU***

*Technical University of Cluj-Napoca, Department of MTC, str. Observatorului, nr.72-74, 400363, Cluj-Napoca, Romania, E-mail: petre.opritoiu@mtc.utcluj.ro

Abstract: *In the case of electronic components cooling, out of many ways and variants of existing heat transfers, the fluid single-phase forced convection heat is an effective and widely practiced method, especially due to its simplicity and economical character. In order to allow the evacuation of increasing heat fluxes, the method was optimized by making special heat exchangers, more and more compact, as meso-channel, micro channels [1] and more recently the porous metal heat exchangers [2,3].*

The objective of the research is to obtain a functional relationship between the cellular structure of open-cell metallic foam and the heat transfer characteristics for forced convective flows. Ideally foams would simultaneously maximize the amount of heat transfer and minimize the pump power needed to force the fluid passing through.

The working method used, is the numerical simulation using FLUENT software in which the actual characteristics of porous metal indicated by the manufacturing company, Erg Materials and Aerospace, were introduced [4].

A simple simulation model is developed in FLUENT to capture the most important behavioral trends of energy flow due to forced convection and conduction through cell ligaments of the cellular foam [5, 6, 7]. The overall heat transfer coefficient of the heat exchanging system and the pressure drop experienced by the fluid flow are obtained.

Trends of heat transfer predicted by the model are expected to be valid for a wide range of open-cell foams and are in reasonable agreement with available experimental data on aluminum foams [8]. The model is applied to evaluate the heat transfer efficiency of open-celled foams as heat sinks for power electronic components. Heat dissipation in high power electronics poses serious challenges for the integration of materials selection with thermal design, circuit design and manufacturing technology.

Keywords*: simulation, cellular structure, flow characteristics, heat transfer performance.*

1. Introduction

Metal foams find applications in ultra light structures where stiffness, strength and toughness are emphasized. Open-celled metal foams can be used to enhance heat transfer in applications such as cryogenic heat exchangers, heat exchangers for airborne equipment, coal combustors, compact heat sinks for high power electronic devices, heat shielding for aircraft exhaust, compact heat exchangers, liquid heat exchangers, air-cooled condenser-cooling towers and regenerators for thermal engines [9]. More uses of these relatively new materials are expected in the future, particularly because low density foams with remarkably uniform and regular cell morphologies are currently being developed using affordable processing methods.

One of the primary reasons to study forced convection in metal foams is to provide information necessary for the possible applications of these materials in electronic cooling and other thermal systems. The fibers of these materials could be thought of as a network of complex extended surfaces giving the advantage of increasing the interfacial area. In addition to the increased interfacial area the formation of eddies or fluid mixing promotes the heat transfer enhancement (fig.1).

Through the phenomenon of turbulence, an intensification of the process of heat transfer and faster exhaustion of heat accumulated when using this type of heat exchanger can be noticed. The overall heat transfer coefficient of the heat exchanging system is calculated, and the pressure drop experienced by the fluid flow obtained. These results are used to analyze and guide the design of optimum foam structures that would maximize heat transfer per unit pumping power. The objective is to select materials that enable the aluminum foam to operate with high power density (up to 100 W/m^2), while maintaining its temperature below that needed to ensure acceptable reliability: usually 90°C.
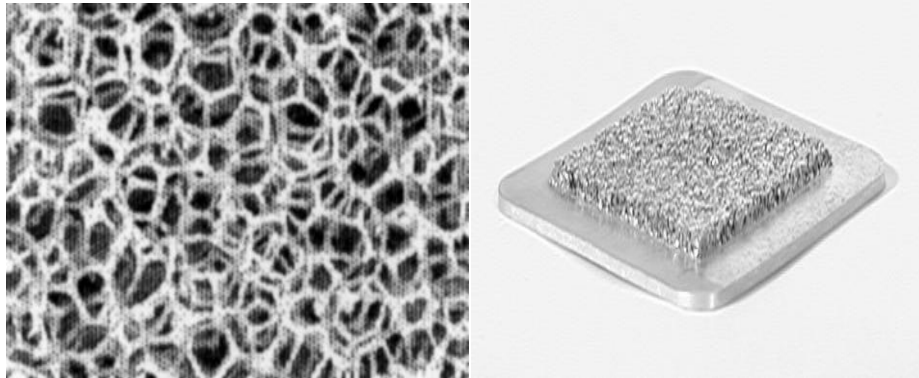
Fig. 1. Micro-computed-tomography of open-celled aluminum foam and aluminum foam heat exchanger [3].

2. Specification of the model

The present work provides a simulation model for the heat transfer in open-cell aluminum foam, when they are used in forced convective mode with a low conductive fluid. The simulation model has been idealized in several ways to limit the complexity of forced convective flow across open-celled foam. Some of the simplifying assumptions made in order to analyze heat transfer in the porous material likely lead to overestimate the actual level of heat transfer but nevertheless should capture the approximate functional dependence of the different control variables such as foam density, cell size and fluid velocity [9]. Assumptions:

1. The porous medium is isotropic and homogeneous with constant porosity, or the porosity variations can be accurately calculated,
2. Natural convection and radiation heat transfer effects inside the porous medium can be neglected,
3. The physical properties of the solid and fluid phase remain constant throughout the temperature range,
4. The solid and the fluid phases are in the thermal equilibrium,
5. Flow is steady and fully developed.

Most of the previous studies on heat transfer in porous medium are based on Darcy's law which is only valid for Reynolds numbers less than about 10 [10,11]. Under such conditions, the fluid and the solid matrix may be assumed to be in local thermal equilibrium so that the fluid saturated porous medium can be treated as a continuum. The model assumes and justifies that there is local thermal equilibrium between the solid and the fluid. This approach eliminates the need for rigorous numerical modeling of three-dimensional flow and heat transfer in and around the pores. Another advantage is that the current simulation model is easily verified by experiments [8].

Consider a rectangular block of porous foam, having a constant cross-sectional area. The analysis uses the typical parameters reported by the foam manufacturers such as the porosity (ε) and the area density (σ), defined as the ratio of the surface area of the foam to the volume (table 1). The hydraulic diameter is determined based on the size of the compressed porous cell (d_P), of the metal filament's diameter (d_l) and the porous density (PPI).

TABLE 1: Metal foam properties [4].

No.	PPI	ε [-]	d_l [mm]	d_P [mm]	Size LxWxt [mm]	σ [m^2/m^3]
1	10	0.914	0.406	5.08	250.8 x 101.6 x 50.8	809.1
2	10	0.704	0.406	1.93	250.8 x 101.6 x 50.8	2053.1
3	10	0.682	0.406	1.24	250.8 x 101.6 x 50.8	3169.3
4	20	0.924	0.203	2.90	250.8 x 101.6 x 50.8	1240.2
5	20	0.774	0.203	0.89	250.8 x 101.6 x 50.8	3593.7
6	20	0.679	0.203	0.63	250.8 x 101.6 x 50.8	5104.3
7	40	0.923	0.102	1.70	250.8 x 101.6 x 50.8	1800.8
8	40	0.918	0.102	1.70	250.8 x 101.6 x 101.6	1800.8

The mean cell size (a) for these foams, according to the ERG catalogue, are 2.0, 1.0 and 0.5 mm, respectively, correspond to 10, 20 and 40 PPI. Thermo-physical properties of aluminum used in the simulation are: density 1.6(10PPI), 2.7(20PPI) and 7.9(40PPI) kg/m^3, specific heat 895J/kgK, thermal conductivity 218W/mK.

The final overall dimensions of the compressed foam blocks used in pressure-drop and heat transfer simulations were 250mm(H) × 100mm(L) × 50mm(W), with the cross-sectional area normal to the flow direction measuring 250mm×100mm. The small thickness is suitable for small foam cooling design such those used in electronic cooling. To make them functional heat exchanger, each foam was brazed in a central position to a 12.7 mm thick heat spreader plate made by solid aluminum.

A typical flow and heat transfer configuration is shown in fig. 2. Cooling fluid having velocity u_0, temperature T_∞ and pressure p_0, is forced into the foam at x =0 (the inlet) and exits at x = L (the outlet) with temperature T_e and pressure p_e. A heat source ($q^{"}$) is bonded or joined to a thin conductive substrate on which a block of open-cell aluminum foam of length L and thickness W is attached. The foam is then placed in a channel, and cooling fluid of velocity u_0 at a temperature T_∞ is pumped through the open celled material, thereby affecting heat transfer from the hot source to the cooling fluid.
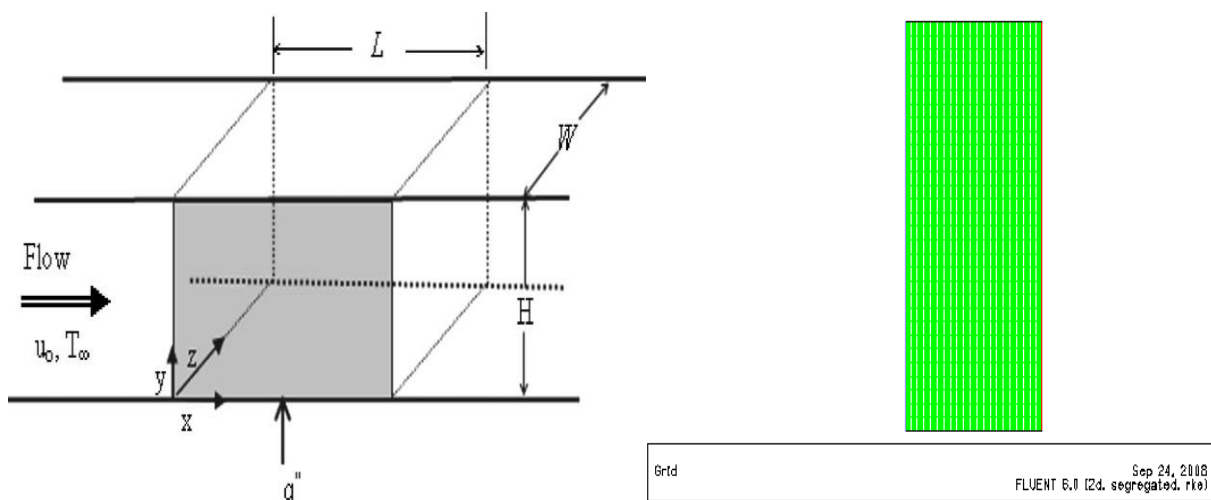

Fig. 2. Porous heat exchanger geometrical model [13] and the equal-sized cubic cells grid [14].

The cubic unit cell is chosen for its simplicity, allowing for approximate closed-form solutions for important heat transfer parameters. It is elegant and efficient to create mesh in one process. This also is more robust when topologically complex problems such as the open-cell metallic foam are being investigated. This means that the mesh generated required no intervention or correction so that solution is, as in flow/heat transfer presented here straightforward.

Uniform temperatures T_1=85°C (358K) on the bottom (y=0) and T_2=22°C (295K) on the top (y=H) are prescribed. The sandwich structure is thermally insulated at both ends and in lateral sides. The temperature of the cooling fluid increases continuously as it flows along the heat exchanger and so the driving force for heat transfer is continually diminished (fig.3).

We therefore wish to establish the fluid temperature as a function of downstream position x, the plate temperature T_1 and the properties of the foam. Several simplifications are made to arrive at an approximate solution for the steady-state temperature distribution of the fluid inside the heat exchanger.
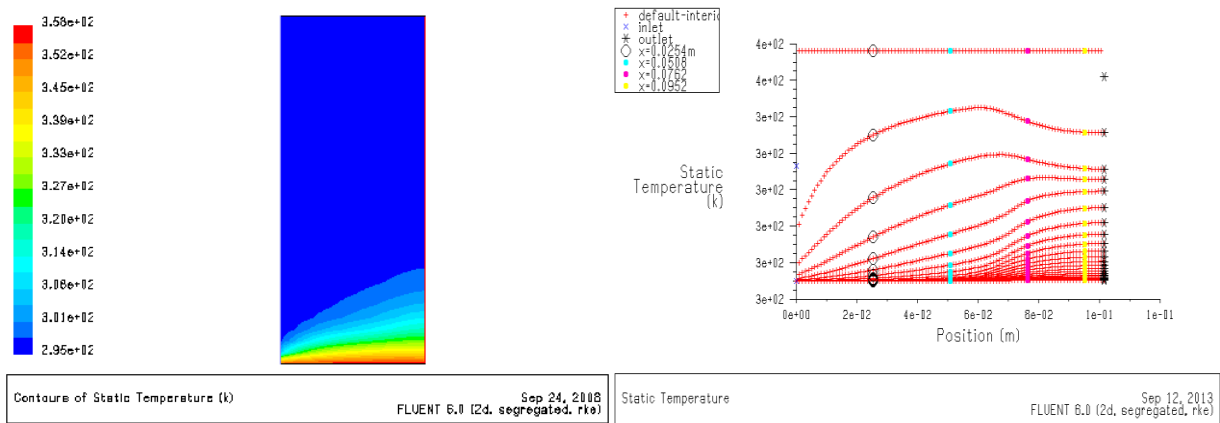
Fig. 3. Contour of static temperature and corresponding xy plot [8].

Turbulence intensity values and resistance coefficients of viscous and inertial type, required for running the FLUENT software for a porous medium were obtained using MATHCAD program, starting from equations specific to Brinkman's porous environment [8]. The overall heat flux dissipation, heat transfer coefficient and pressure drop caused as the fluid flows across the foam are calculated using the model and the optimum foam properties for the best heat transfer performance are suggested.

3. Application: porous heat exchanger for power electronic devices

The model presented in previous section can be used to analyze a variety of heat exchanger applications where the large surface density of open-celled metal foams is required. The maximum amount of heat that the fluid can extract from the system was determined according to equation [9]:

$$Q = \dot{m}c_p(T_1 - T_0) \tag{1}$$

where $\dot{m}$ is the flow rate, c_p is the specific heat, T_0 and T_1 are the inlet and the base temperatures of the fluid measured by thermocouples. Heat dissipation plots were obtained for different porosities and porous densities. The model and its underlying assumption were verified by simulation for several aluminum foam samples using air as the coolant [8]. All simulations were performed under steady state conditions and were carried out in the range of average air velocity $0.8 < v < 8$ m/s.

For both water and air cooling, dissipative heat flux removed by a porous heat exchanger of 50 mm thickness as a function of relative density (ρ) is plotted on fig. 4, for 10, 20 and 40 PPI porous densities, porosity ε= 0.927, $λ_{s,Al}$ = 200W/mK, ΔT= T_1-T_0= 63°C (336K).
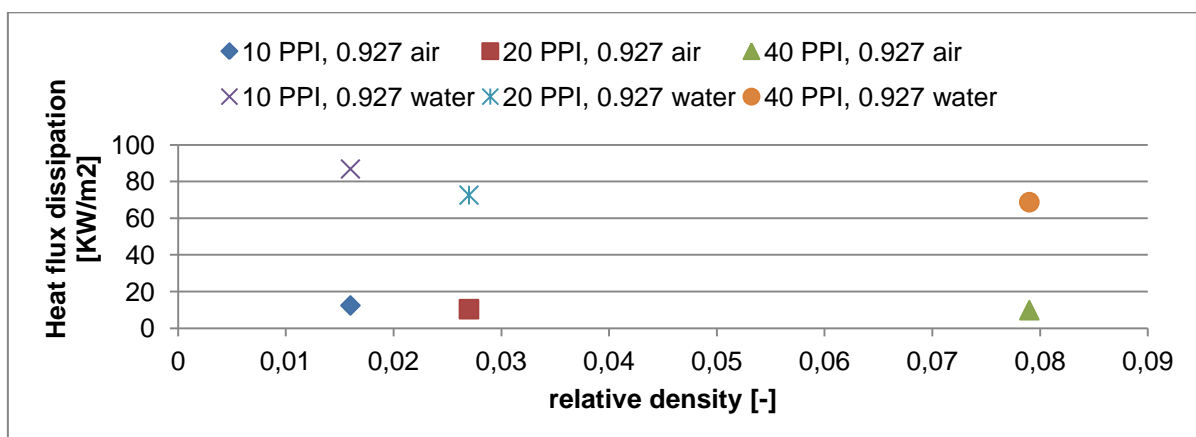

Fig. 4. Heat flux dissipation as a function of relative density.

It is seen that, even with forced air convection in aluminum foam heat exchanger, with relative density of 0.079(40 PPI), heat is efficiently dissipated (q= 10 kW/m², if air cooling and q= 69kW/m², if water cooling), indeed making it a very attractive device due to its compactness and light weight. Under these conditions the difference between the temperature of the wall and the air does not exceed 63°C. The heat transfer from the foam to the fluid will increase as either the porosity decreased (thus increasing surface area for heat transfer) or as the relative density (ρ) increases (thus increasing heat conduction through the ligaments) or as the velocity of the fluid increases (fig.5).
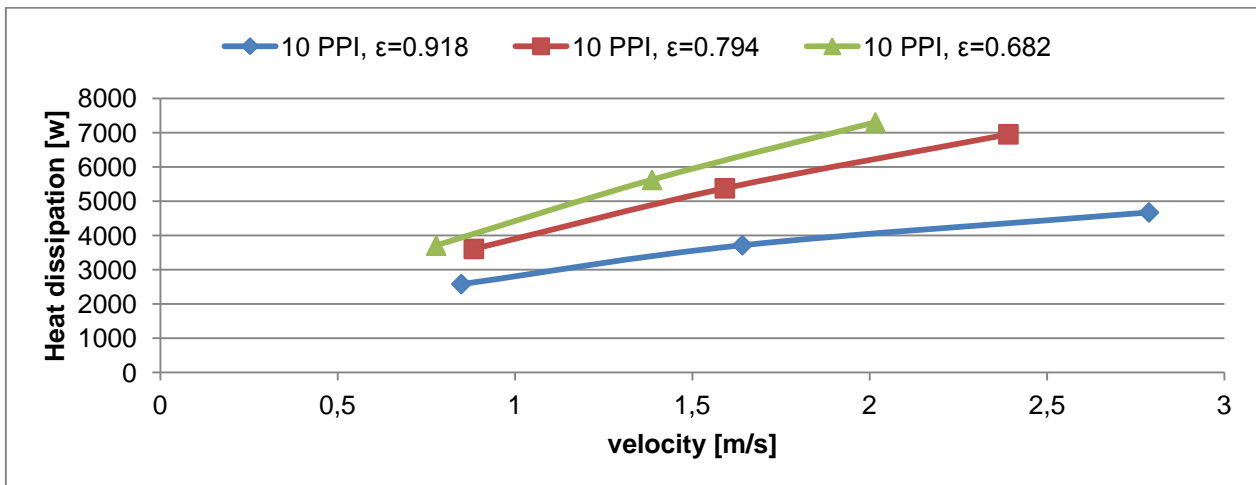

Fig. 5. Heat flux dissipation plotted against flow velocity, for 10 PPI porous density and porosities ε=0.918, 0.794 and 0.682.

Bigger heat dissipative was obtained for higher velocities and for foams with higher surface area densities or lower porosity. With σ>1000 m²/m³ even at very low densities (ρ=0.02), the conclusion drawn from these results is that open-celled metal foams well qualify as compact heat exchangers. Compact heat exchanger generally require σ>700 m²/m³ and are essential in applications where the size and weight of the heat exchanger is constrained due to design considerations. The average heat transfer coefficient is defined as [9]:

$$\alpha = \frac{q}{T_w - T_f} \qquad (2)$$

where T_w is the average wall temperature, measured by the thermocouple, T_f is the average value of the fluid temperature, calculated as the mean of the inlet T_0 and the outlet T_2 , temperature of the air in the test section. For metal foams α depends on the fundamental variables: foam density, channel width, fluid velocity, etc. the simulated values of α is much larger than that measured by experiments. The overestimates may be attributed to the simplifying assumptions of the model in order to obtain simple solutions.

For turbulent flows which are expected to occur in metal foams, the convective heat transfer coefficient calculated from equation (2) is typically on the order of $10^2 \sim 10^4$ W/mK. It is noticed that at the same porosity, the thermal convection coefficient is higher if the porosity density is higher, the difference between them increases with decreasing speed (fig.6).
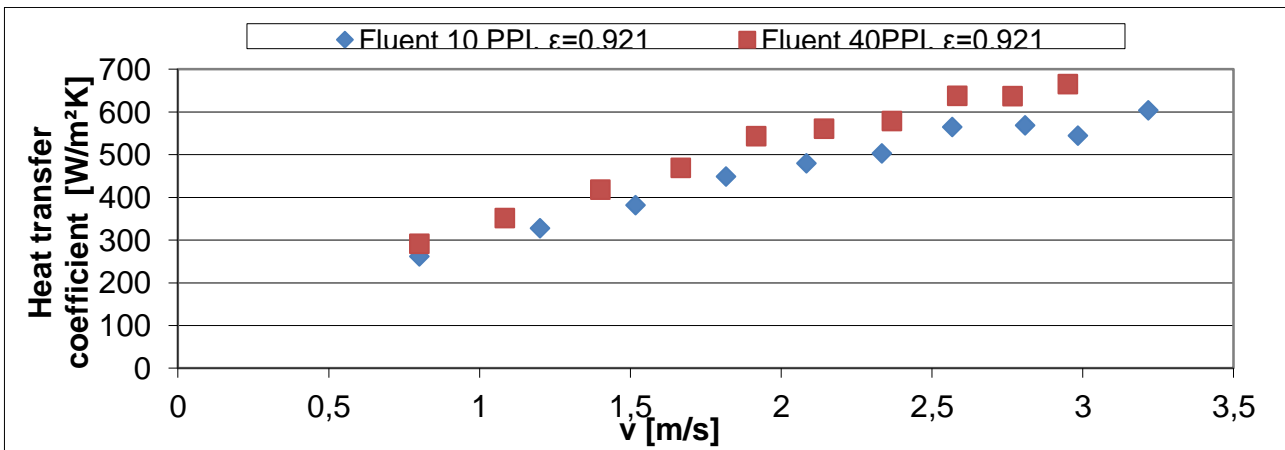
Fig. 6. Heat transfer coefficient plotted against flow velocity, for 10 and 40PPI porous densities and porosity ε=0.921.

For air at atmospheric pressure and room temperature with $v_{max.}$=3.5 m/s, one calculates from equation (2) that $\alpha_{max.}$=665 W/(m2K). At the same time, it can be observed that at the same speed and porosity density, the thermal convection coefficient grows with decreasing porosity and increasing relative density (fig.7, 8).

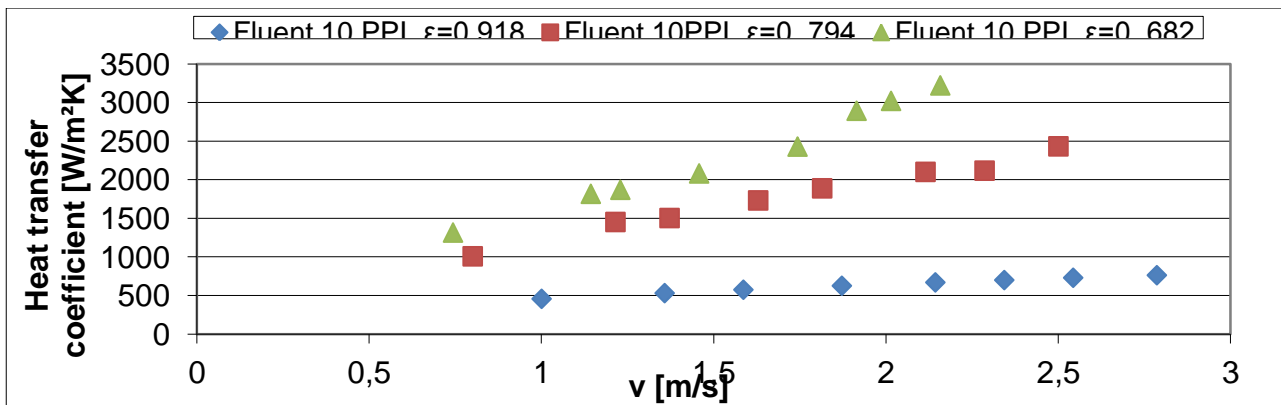**Fig. 7.** Heat transfer coefficient plotted against flow velocity, for 10 PPI porous density and porosities ε=0.918, 0.794 and 0.682.
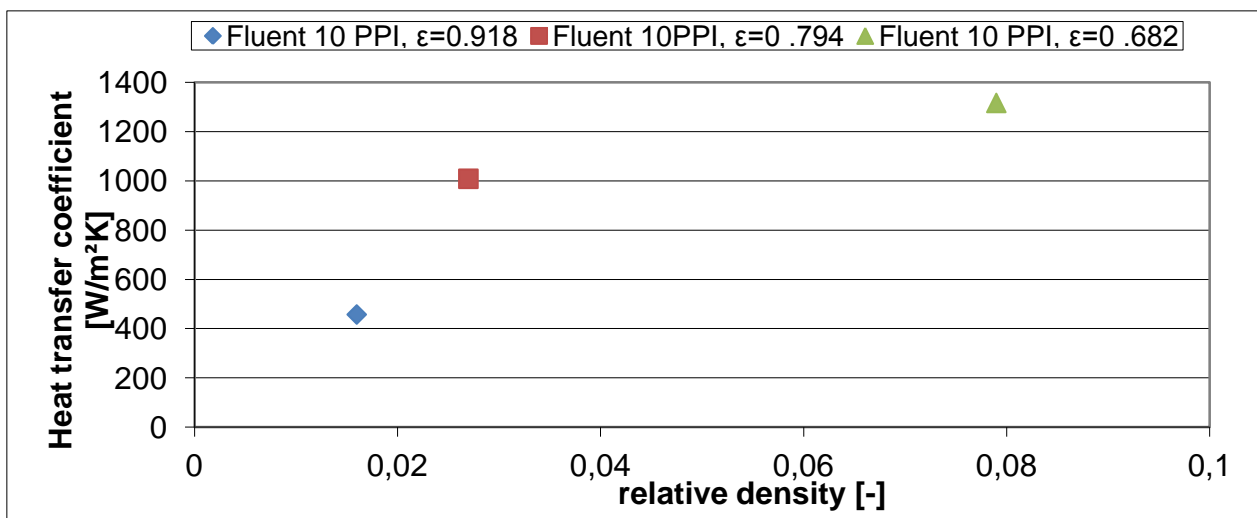
Fig. 8. Heat transfer coefficient as a function of relative density, for 10 PPI porous density and porosities ε=0.918, ε=0.794 and ε=0.682.

Pressure drop per unit length for porous media may be expressed using Forchheimer equation:

$$\frac{\Delta P}{L} = \frac{\mu_f}{K} \cdot v_f + \frac{c_F}{\sqrt{K}} \rho_f \cdot v_f^2 \tag{3}$$

where $\Delta p/L$ - pressure drop per unit length, μ_f - fluid viscosity, K - permeability, v_f - velocity, c_F - inertial coefficient, ρ_f - fluid density.

The pressure drop is also influenced by the porosity, the density of porosity and the fluid velocity and thickness. At the same porosity density the pressure drop is influenced by the flow rate of working agent and thickness. At the same porosity and flow rate, the pressure drop increases with the density of porosity (fig.9).
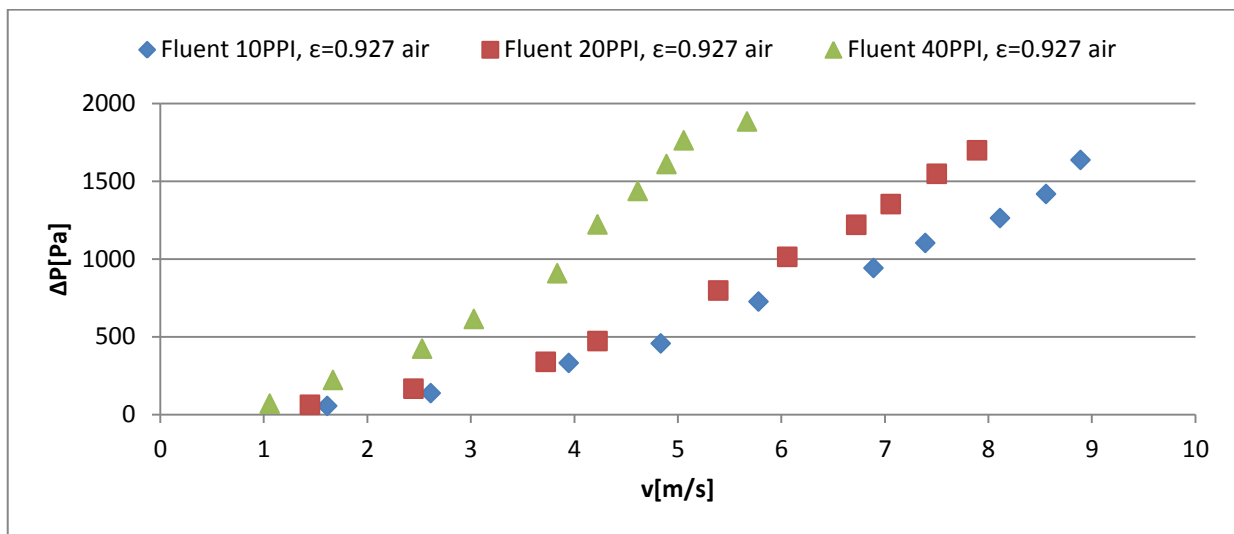
Fig. 9. Comparison between simulated pressure drop data at different velocities, for 10, 20 and 40 porous densities and porosity ε=0.927.

As seen compression has profound effect on the pressure-drop behavior of compressed foam. As expected, those foams which possess the highest solid fraction (highest porous density and lowest ε), generated the largest pressure drop (fig.10).
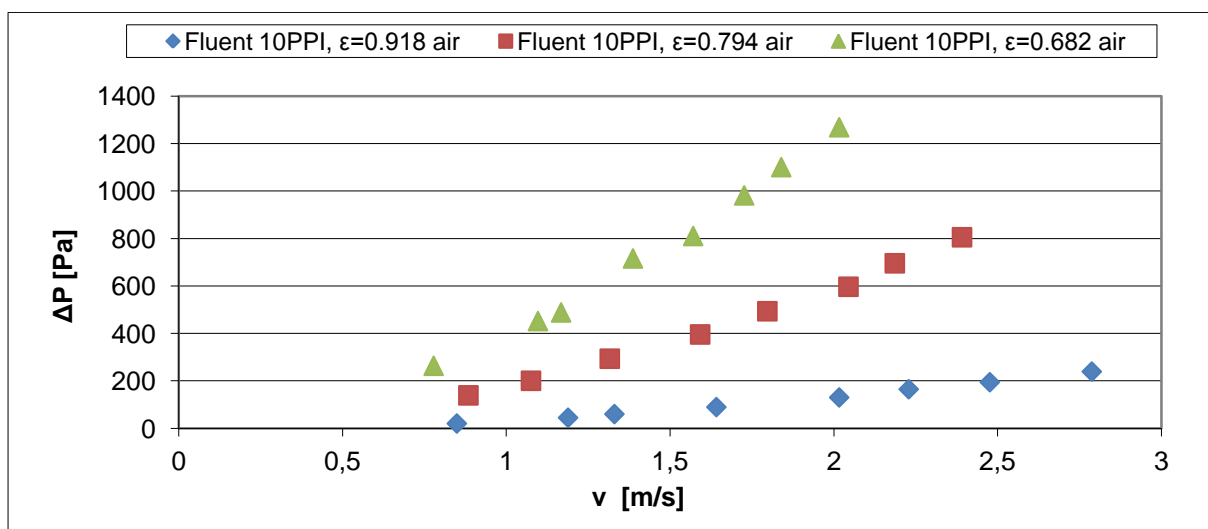
Fig. 10. Comparison between simulated pressure drop data at different velocities, for 10 PPI porous density and different porosities ε=0.918, ε=0.794 and ε=0.682.

The predicted pressure drop are plotted in fig. 11, as functions of relative foam density ρ, for air at T_2 =22°C flowing across the duct filled with aluminum foam. These results are generally in agreement with the experimental measurements by [8].

Whilst a foam having the smallest cell size a=0.5mm (40PPI), and highest relative density ρ=0.079 maximizes heat transfer it unfortunately also maximize pressure drop. The predicted minimum pressure drop occurs at a relative density equal to 0.016 (10 PPI) for aluminum ERG foams.

A high pressure drop not only increases the operational cost but often also leads to intolerable noises. One of the advantages of designing exchangers with foams is that they still have excellent heat transfer coefficient even if the mean flow velocity falls below the critical value required to maintain turbulent flow. Also, the foam itself may act as a noise suppressor due to its sound absorption capabilities.

Fig. 11. Pressure drop as a function of relative density ρ=0.016(10 PPI), 0.027(20PPI) and 0.079(40 PPI).

The heat transfer performance of the foam may be best characterized by a non-dimensional index I_1 combining both α and Δp [9]:

$$I_1 \equiv \frac{\alpha}{C_1} \frac{1}{\Delta p}†$$

$$(4)$$

Fig. 12. The index of the foam performance as a function of relative density ρ=0.016(10 PPI) and 0.079(40 PPI).

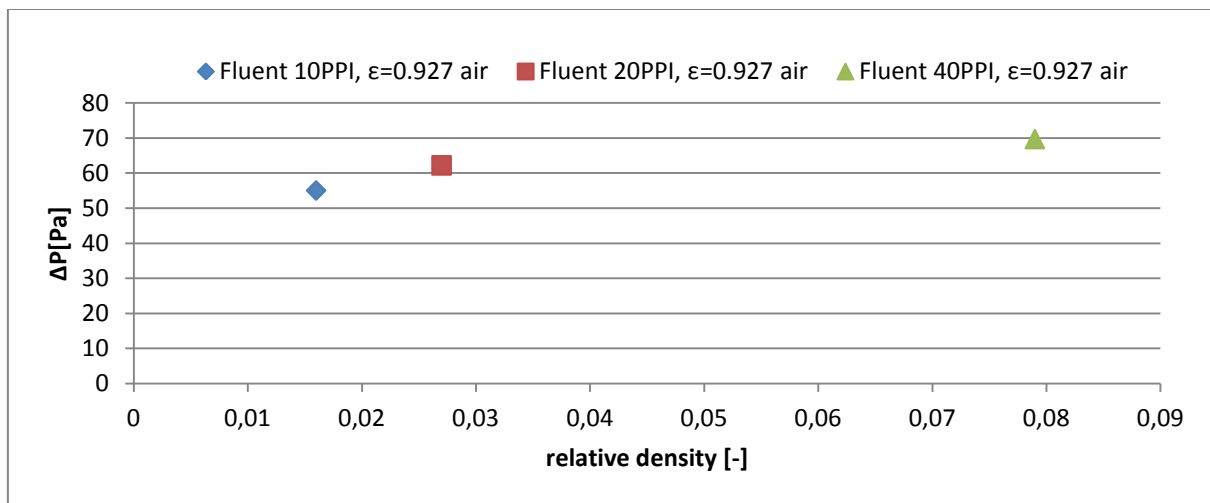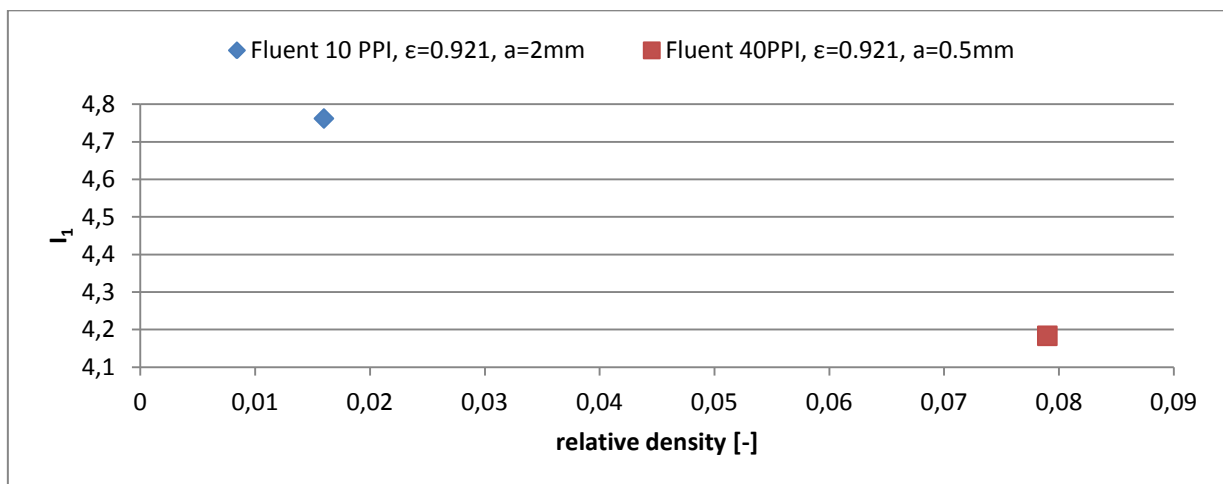Fig. 12 plots the index of the foam performance I_1, as a function of foam relative density ρ. Clearly there exists an optimum foam density which would maximize I_1. The cell size (a), does not affect ρ_{optim} but at a given density foam with larger cell size perform better than those having smaller cell size. If the weight of an heat exchanger is cause for concern in applications such as airborne equipments, the appropriate index for performance scaling may be taken as $I_2=I_1/\rho$. Here, the best performance is achieved by a foam with $\rho \to 0$ having the largest cell size [9].

In any heat exchanger design, the heat convection performance of the heat exchanger must be weighed against the energy required to operate the system, which is the pumping power in this configuration. In fig. 13 the optimal design is that which minimize the distance from the point to the origin of the plot [15].
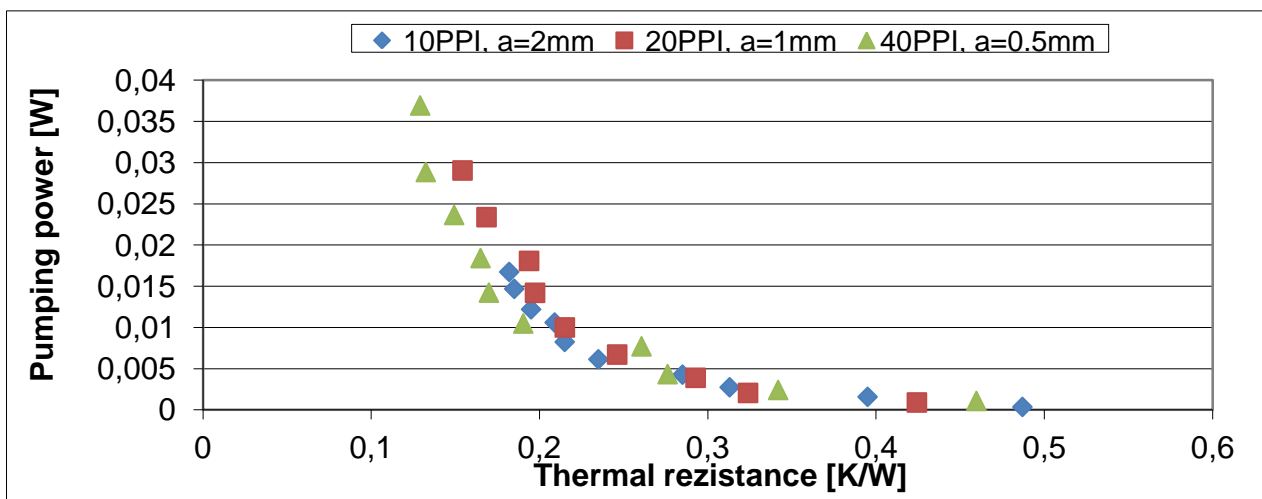

Fig. 13. Plot of the required pumping power against the corresponding thermal resistance.

This point was obtained by foam with 40PPI porous density and for a thermal resistance of 0.129 K/W. The metal foam heat exchangers decreased thermal resistance by nearly half when compared to currently used heat exchangers designed for the same application.

4. Conclusions

The simulated model is applied to evaluate the heat transfer efficiency of open-celled foams as heat sinks for power electronic components. The investigations were carried out for different types of open-cell porous aluminum having different geometrical characteristics: porosity, pore density and different flow rates of coolant. Through numerical simulation were identified optimal geometric characteristics necessary for this type of exchanger to achieve the most efficient cooling of electronic equipment that it serves, in terms of pressure drop as low as possible.

An interpretation of results was carried out, in order to apply the conclusions that result from the present research on the existing types of open cell porous aluminum heat exchangers and the design of new ones. Solutions for the overall heat transfer coefficient and pressure drop as functions of cell morphologies and other relevant heat transfer parameters are obtained, which can be used to guide the design of optimum cellular structures that maximize the heat transfer rate per unit pumping power (the energy expended driving the convective flow).

References

[1] Zhang, H. Y., Pinjala, D., Joshi, Y. K., Wong, T. N., Toh, K. C, Iyer, M. K., 2005, "Fluid flow and heat transfer in liquid cooled foam heat sinks for electronic packages", ASME, vol 28, pp. 272-280;
[2] Boomsma, K., Poulikakos, D., Zwick, F., 2003, "Metal foams as compact high performance heat exchangers". Swiss Federal Institute of Technology, Zurich, Switzerland;
[3] Banhart, J.: "Manufacture, characterisation and application of cellular metals and metal foams". Fraunhofer Institute for Manufacturing and Advanced Materials, Bremen, Germany;

[4] ERG, Materials and aerospace corporation, "Duocel aluminum foam brochure"*, 2003, Oakland, CA;

[5] Opritoiu, P., "Research on heat transfer and pressure losses through porous metal heat exchanger", PhD thesis, avril 2014, Techicall University of Cluj-Napoca, Faculty of Mechanics;

[6] FLUENT v. 5/6, "User's manual"*, Fluent Inc.;

[7] Gambit v.5/6, "User's manual", Fluent Inc.;

[8] Opritoiu, P., 2014*, "Validation of porous heat exchanger simulation model", Proceedings of HERVEX 2014, "International Conference and Exhibition of Hydraulics & Pneumatics", Călimăneşti, 5-7 noiembrie 2014, Vol. 21, pp. 208-216, ISSN 1454-8003;

[9] Lu, t. J., Stone, A., and Ashby, M. F., 1998, "Heat transfer in open cell metal foam", Acta Mater, 46(10), pp. 3619- 3635;.

[10] Tien, C. L. and Vafai, K., Adv. Appl. Mech., 1990, 27, 225;

[11] Bejan, A., Heat Transfer. John Wiley & Sons, 1993;

[12] Opritoiu, P., 2013*, "*Modelling turbulence in open cell aluminum foam heat exchanger"*, Acta Tehnica Napocensis, Series: Applied Mathematics and Mechanics, nr. 56/2013, vol.4, pp. 739-749;

[13] Nihad, D., Ruben, P., and Alvarez, H., 2006, Heat transfer analysis in metal foams with low-conductivity fluids, ASME J. of Heat Transfer, 128, pp. 784-789;

[14] Opritoiu, P., 2007, "Fluid flow and pressure drop simulation in aluminium foam heat exchanger", Acta Tehnica Napocensis, nr.50;

[15] Opritoiu, P., 2013, "Rans simulation of combined flow and heat transfer through open-cell aluminum foam heat sink", Magazine of Hydraulics, pneumatics, tribology, ecology, sensorics, mechatronics - Hidraulica no. 3/2013, pp. 15-25; ISSN 1453-7303;

[16] Giurgiu, O., Plesa, A., Opruta, D., 2014, "The effect of plate heat exchanger's geometry on heat transfer", Leonardo Electronic Journal of Practices and Technologies, nr. 25/ 2014;.

[17] Opruţa, D., Vaida, L., Pleşa, A., 2008. "The flow simulation through a hydraulic resistance", Annals for DAAAM 2008 – & Proceedings of the 19th International DAAAM Symposium, Oct. 2008, Trnava, Slovakia.

Experimental Investigation on Transient Response of Two Stage Pressure Relief Valve

Prof. **Basavaraj V.HUBBALLI**[1], Dr. **Vilas B.SONDUR**[2]

[1]Jain College of Engineering, Belagavi Karnataka, India, bvhubliabhi@gmail.com

[2]Founder Director, Sondur Academy, Belagavi Karnataka, India, vbsondur@gmail.com

Abstract: *Pressure control valves are used in fluid power systems to control the operation of the hydraulic system. The time response of a hydraulic system is the integrated result of the response times of all of the components used in the system. The ability to understand and manage the valve performance characteristics like transient response, pressure-flow are important in automation and heavy industrial processes. In this paper, part of experimental research work carrying out on the two stage pressure relief valve is presented.*

Keywords: *Cracking pressure, Pilot valve, Pressure override, Relief Valve, Two stages, Transient response.*

1. Introduction

Considering safety and accuracy reasons, it is required to control pressure in hydraulic system as quick as possible. Hence to know the response, sensitivity and performance consistency of the pressure control valves are very much essential. These factors play major impact in the precision hydraulic control systems.

The approaches adopted to study the performance of the valves are mainly experimental and computer numerical simulation study. Many researchers have experimented and analyzed the valves for the fluid characteristics, operating parameters, and the coefficients such as discharge coefficient and pressure loss coefficient .From the viewpoint of practical application, this method is more reliable and suitable, since the real situations are usually simulated in the experiments.

A pressure control valve can be used to limit the maximum pressure (a relief valve), to set a back pressure (a counter balance valve), or to pass a signal when a certain pressure has been reached (sequence valve). The principal feature of most pressure controls is that the hydraulic forces are resisted by a spring.

2. Pressure Relief Valve

The most widely used type of pressure control valve is pressure relief valve, since it is found in every hydraulic system. It protects the system against overpressure, which may occur due to excessive actuators loads or due to the closing of the valves. It is normally a closed valve whose function is to limit the pressure to a specified maximum value by diverting pump flow back to the reservoir.

Direct operated pressure control valves are limited as the flow increases due to the space required for the control spring. A larger flow requires a larger poppet or spool diameter. The area and hence the spring force increases proportionally to the diameter squared. In order to keep the space required for these valves down to a sensible level, two stage (pilot operated) valves are used.

Two stage valves is a pilot operated relief valve which gives good regulation of pressure over a wide range of flow. They are used to limit the operating pressure or limit and unload the operating pressure by means of solenoid operation.

3. System response and stability

Rapid response is generally an essential requirement of a hydraulic servo system. However, if the response is too rapid the system can become unstable, in which case damping has to be introduced. The necessary degree of system damping for stability will depend upon:

- The system response
- The load inertia
- The back-lash of the system

A system is said to be 'underdamped' when the output resulting from a step input is oscillatory but ultimately reaching a steady condition. Critical damping is that at which the system just ceases to oscillate and the output achieves a steady state in the minimum possible time. When the damping is greater than the required for critical damping the system is said to be 'overdamped'.

4. Operational description

The pilot valve is a direct operated pressure relief valve. The pressure present in system line P acts on main spool. At the same time, the pressure is fed to the spring-loaded side of the main spool via control lines containing orifices and also to the poppet element in the pilot valve.
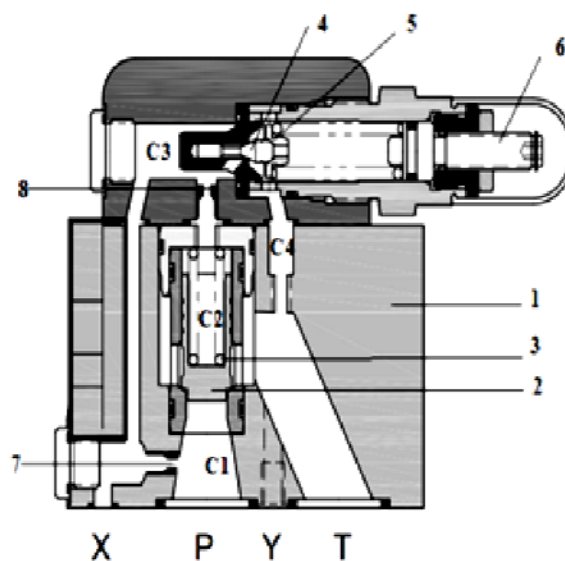
(1- Valve housing; 2 – Main Spool; 3 – Spring; 4- Pilot Poppet; 5 - Spring; 6- Screw; 7 – Orifice 1; 8- Orifice 2 ; P- Pressure line port ; T- Tank port)

Fig. 1. Sectional view of the valve (PPRV20)

If the pressure increases in system line to a above that set by spring, poppet element opens against spring. It creates unbalance on the main spool and it will lifts off its seat to permit larger flow into the tank. Since main spool compresses only the light spring, and hence very little override occurs compared to the single stage pressure relief valve.
This valve can be observed as a system consisted of three subsystems: main spool 1(cylindrical poppet) , pilot poppet 4 and fixed orifices 7,8. In neutral position both pilot poppet and main spool are closed under the influence of the springs 3 and 5, and there is a balance of forces at the closing element of the main spool 1. When inlet pressure will reach higher value than the preset spring force 5 of the pilot poppet, the closing element of the pilot poppet 2 is opening and through the orifices there is beginning to flow some little amount of pilot flow.
The pressure in the upper part of the main spool is maintaining approximately constant by the pilot poppet. With further increase of the inlet pressure the pressure drop continues to increase and main valve relieve the major flow to the tank.

5. Experimental Investigation

Two Stage Pressure Relief Valve tested on the developed experimental setup to investigate the transient response of the valve. On the existing double-pump hydraulic test rig, arrangements were

made shown in the Fig.5. It consists of a high-pressure, low volume pump P1 in conjunction with a low-pressure, high-volume pump P2. Two pressure transducers and output data logger digital storage oscilloscope (DSO) is used to record the pressure transient response of the valve.

Application of this system is used where wide range pressure – flow regulations required. This system eliminates the necessity of having a very expensive high-pressure, high-volume pump. The valve fitted on the hydraulic test rig as shown in the fig. Before switching on the system, all the pressure relief valves kept open. Then pressure built on the system by energizing the solenoid valve to close. The maximum pressure of the system set by operating the relief valves. Test valve loaded by setting the cracking pressure, which is lower than the system pressure.

When solenoid directional control valve is energized, the pressure built in the line of pressure relief valve. Once the pressure exceeds the set pressure, test valve gets cracked and releases the flow back to the reservoir. During this process, transient response of the valve is observed through the data acquisition system. Here through the oscilloscope and pressure transducers, the transient response of the valve is studied.

Fig.4 shows the hydraulic circuit of the test stand for determination of transient response of the specified pressure relief valve.
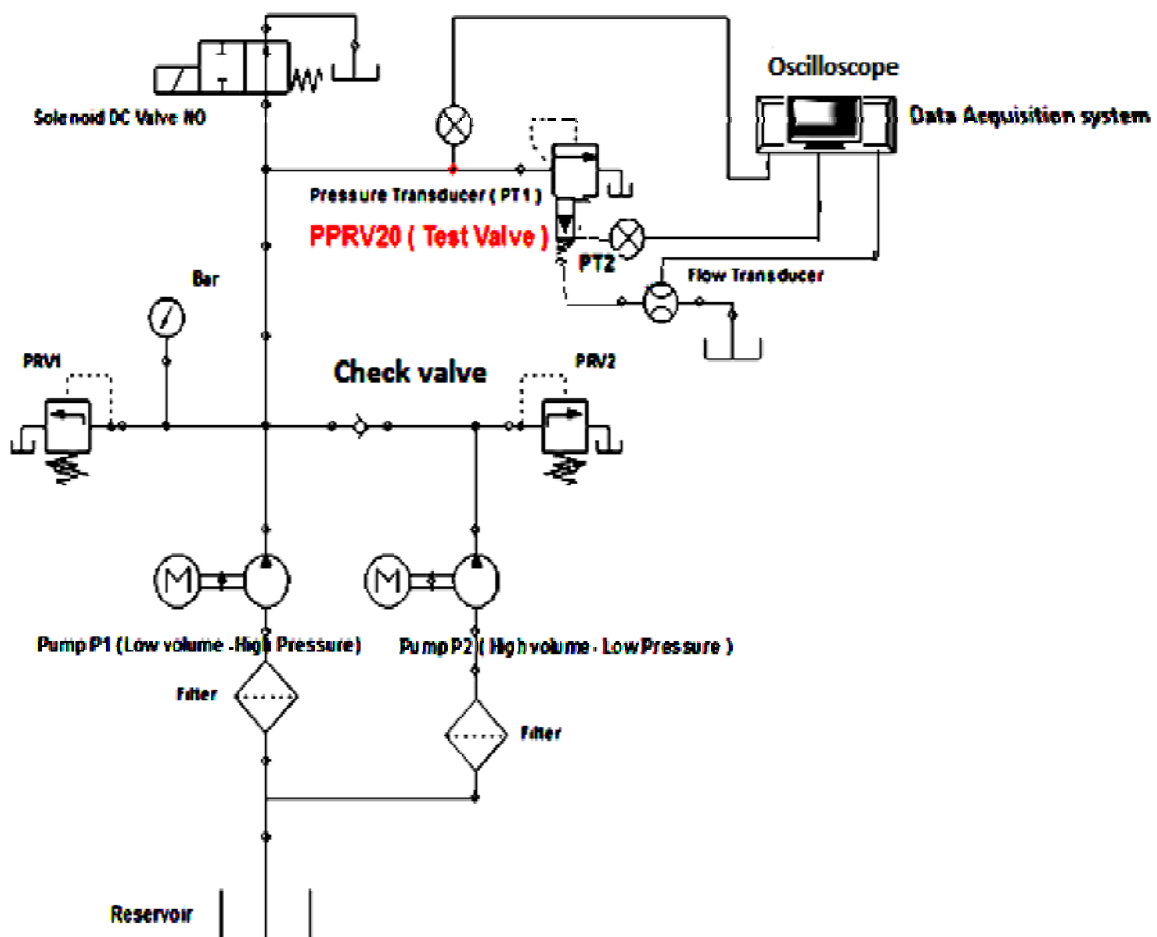

Fig. 2. Test Rig Hydraulic circuit

6. Results and discussion

Here the transient response of the pilot relief valve and main relief valve investigated separately and plotted the graphs.

Pilot valve Relief Pressure = 180 bar, Main valve Relief Pressure = 188 bar

The following parameters are used for the determination of the response.

Delay time: The time required for the output to reach 50% of the steady Output.
Rise time: The time required for the output to rise from 10% to 90% of the final output value
Maximum overshoot: The time at which the maximum overshoot occurs.
Settling time: The time for the system to reach and stay within a stated plus-and-minus tolerance band around the steady-state output
Pressure peak p_{Emax}:

$$P_{Emax} = V_m / p_E * 100$$

The maximum overshoot V_m is the largest deviation of the response from the set command value after the transient tolerance has been overshoot for the first time.
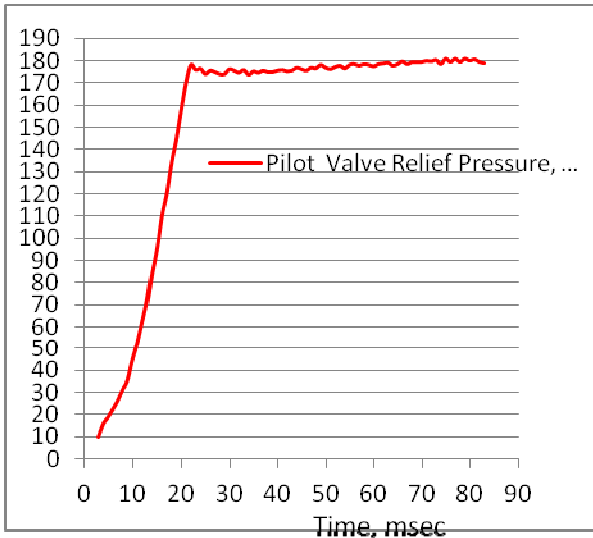
Fig. 3. Transient response of pilot relief valve   **Fig. 4.** Transient response of main relief valve
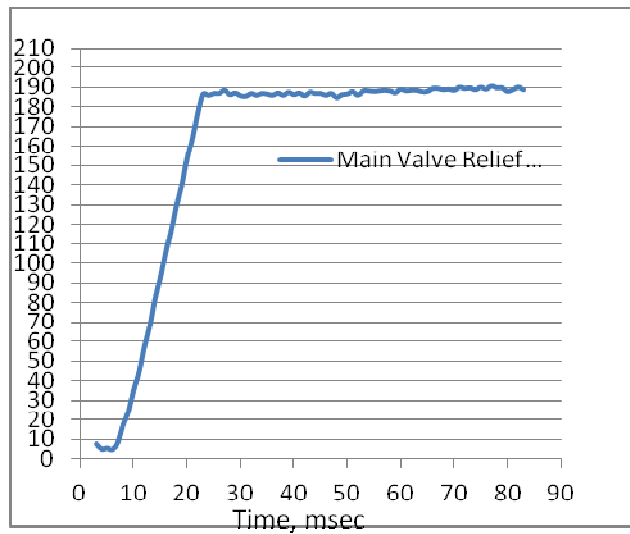
TABLE 1: Response time

Time in , msec	Pilot Valve	Main Valve
Delay time ,	14	16
Rise time	15	13
Max over shoot time	---	----
Settling time	70	67
Pressure Peak	0.44 %	0.68%

From the graphs it is observed that, overshoot not exist in the valve. There is a pressure decrease in front of pilot poppet after it cracks i.e. just open. Due to this pressure drop, imbalance occurs on the main cylindrical poppet and lifts off from the seat against the light spring. It releases the major flow to the tank without much working on the oil.
This is the first technical paper to present the new method to measure the pressure override characteristics of the valve in the form of transient response curves of both pressures in the form of graph. It is seen that, there is a reduction in the pressure, as pilot valve cracks and later it stabilizes to the set pressure.

Fig. 5. Pilot relief pressure v/s Main relief pressure

Fig. 6. Transient Response of both stages

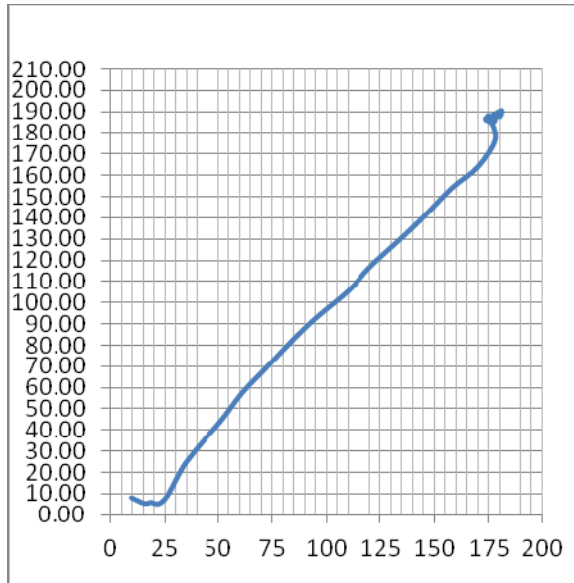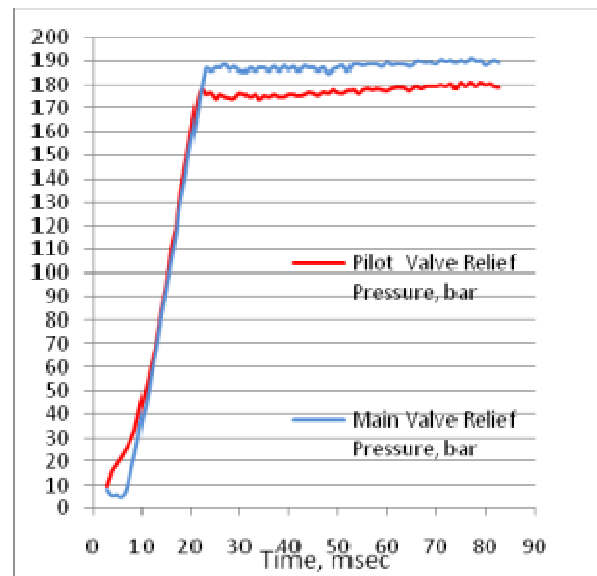From the transient pressure curves, both the pressures of poppet relief valve and main relief valve remain same, till the pilot valve cracks. The pressure override of this valve is 8 bar and which is less compared to the single stage relief valve. Pressure override is the difference between the cracking pressure or opening pressure and the pressure drop across the valve when it is passing the maximum rated flow at the same valve setting.

7. Conclusion

From this experimental investigation and literature survey, it concludes that its pressure override is less compared to the single stage pressure relief valve. The highlight of this research work is to correlate the pressures of both pilot relief valve and main relief valve in the form of graph.
The ability to understand and utilize the response information obtained from the individual component manufacturers is very much necessary while observing the response of a whole hydraulic system.
Based on the transient response curves, the dynamic behaviour of the valve is presented in the form of time response parameters.
But on the other hand, this method is very expensive in time, manpower and facilities. For further research work, computer simulation is also used to investigate and validate with the experimental results.

References

[1] Michael Pinches and John G. Ashby, "Power Hydraulics", Prentice hall International (UK) Ltd , UK , 1989.
[2] M. Galal Rabie, Fluid Power Engineering, McGraw –Hill, 2009;
[3] H. Exner, R. Freitag "Basic Principles and components of Fluid Technology", By Mannesmann Rexorth;
[4] Bud Trinkel, "Fluid Power Basics" Hydraulics & Pneumatics magazine;
[5] John Watton, "Fundamentals of Fluid Power Control", Cambridge University Press. 2009;
[6] Sasko S. Dimitrov "STATIC CHARACTERISTICS OF PILOT OPERATED PRESSURE RELIEF VALVES WITH COMPENSATING PISTON". Proceedings of the XVI National Scientific Conference with International Participation Energy- Ecology- Comfort- Self- confidence, 17th – 20th September 2011, Sozopol, Bulgaria;
[7] Sasko Dimitrov . "Numerical and experimental determination of static characteristics of a pilot operated pressure relief valves";
[8] Jekel, T. B., Claas, M., and Reindl, D. T. (2011). "Development and Validation of a Bench Test Procedure for Post Mortem Testing of Relief Valves ".Presented at IIAR 2011 Ammonia Refrigeration Convention & Exhibition Orlando, FL March 26-30;

[9] K. Dasgupta and R. Karmakar "Dynamic Analysis of Pilot Operated Pressure Relief valve**"** SIMULATION MODELLING PRACTICE AND THOERY, ELSEVIER, December 2001;

[10] YAMIN LUO Mᴀʏ 2006**, "**SYSTEM MODELING AND CONTROL DESIGN OF A TWO-STAGE METERING POPPET-VALVE SYSTEM";

[11] www.polyhydron.com/ Pressure Control Valves;

[12] Sasko Dimitrov, Simeon Simeonov, Slavco Cvetkov, "Static Characteristics of the Orifices in a Pilot Operated Pressure Relief Valve"," Hidraulica" (No2/2015), ISSN 1453-7303;

[13] Corneliu Cristescu et al., "Theoretical and experimental research regarding the dynamic behaviour of linear hydraulic motors", "Hidraulica" (No1-2/June 2011), ISSN 1453-7303.

Experimental Methods Aiming to Improve Dynamic Performance of Pneumatic Actuators

Ph.D. eng. **Gabriela MATACHE**[1]**,** Ph.D. eng. **Gheorghe SOVAIALA**[1]**,** Ph.D. eng. **Radu RADOI**[1]

[1] INOE 2000-IHP

Abstract: *This paper presents the tests carried out on two dimensional types of pneumatic actuators to determine their dynamic characteristics, highlighting the main factors and methods influencing them. The paper presents only three of the tests that have been conducted on actuators. They are:*
- response to step signal in three points of the stroke, at constant pressure - 8 bar;
- response to sine wave signal having initial amplitude, from minimum to maximum value, for three stroke values;
- determining the minimum starting pressure for the pistons of pneumatic actuators for both directions of travel (rod chamber and piston chamber).

Keywords*: pneumatic actuators, dynamic performance, influencing factors*

1. Introduction

In recent years in the Laboratory for Pneumatics of Hydraulics and Pneumatics Research Institute INOE 2000-IHP there have been research concerns about medium pressure pneumatic actuators. There have been developed testing methodologies and test devices for them.
The tests carried out on two dimensional types of medium pressure pneumatic actuators **(DNCKE-100-200-PPV-A**, respectively **DNCKE-40-130-PPV-A)**, highlight the main influencing factors and methods concerning their dynamic behavior, under no load, and they have consisted in [1],[5]:

a. response to step signal in three points of the stroke, at constant pressure - 8 bar;
b. response to sine wave signal having initial amplitude, from minimum to maximum value, for three stroke values;
c. determining the minimum starting pressure for the pistons of pneumatic actuators for both directions of travel (rod chamber and piston chamber).

2. Presentation of the experimental test bench

It consists of (see Fig. 1):

1. Compressed air supply-compressor + air preparation unit GPA
2. Testing device consisting of: Frame; Medium pressure actuator -ALP; Reflex displacement transducer -TDR; Pressure transducers -TP$_1$ and TP$_2$; Proportional directional control valve - DP
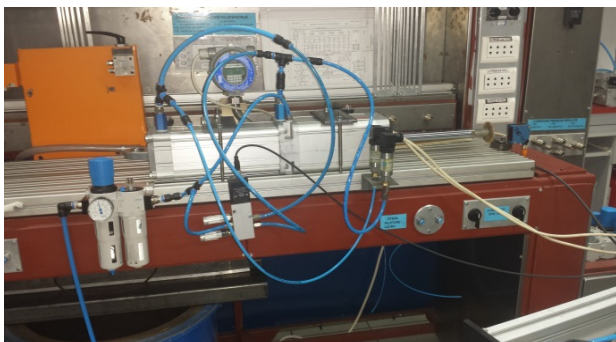3. Computerized data acquisition system.

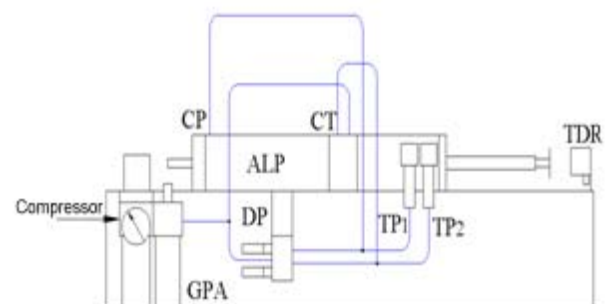**Fig. 1.** Bench for testing the DNCKE-100-200-PPV-A medium pressure actuator

Fig. 2. Pneumatic circuit diagram of the test bench in dynamic regime

The testing software, developed in LabVIEW, consists of block diagrams conducting the test in automatic mode. The results consisting of charts and databases are automatically saved.

On the input of USB-6218 data acquisition board there are inserted voltage-type signals from the pressure transducers (corresponding to the two chambers of the actuator under tests) and the (reflex) displacement transducer [3]. One of the two analog signal outputs of the acquisition board is used to drive the proportional directional control valve in the testing diagram.

Feeding the electromagnets of the proportional equipment, the sensors and data acquisition board is done from a 2-channel power supply, Figure 3.
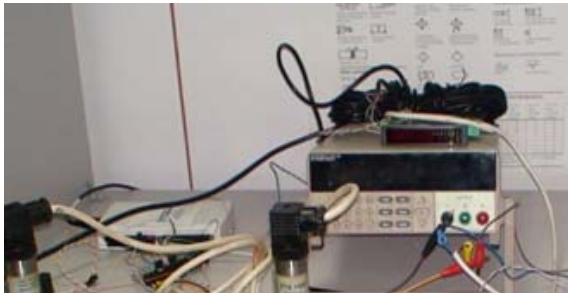

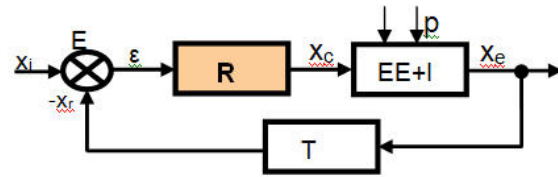**Fig. 3.** 2-channel power supply

Fig. 4. Block diagram of automatic control system

In the automatic control system used to drive the pneumatic actuators, the automatic regulator (RA) is meant to operationally process the error signal ε (resulted following the linear – additive comparison between input parameter x_i and response parameter x_r in the comparison element) and to generate an output control signal x_c for the execution element. It is located on the direct route between the comparison element and the execution element (the actuator), according to the block diagram of automatic control system shown in Figure 4 [4].

Current information on the automated process is obtained by means of the response transducer TR and it is processed by the automatic regulator RA in compliance with a certain law which defines the algorithm for automatic control (the adjustment law).

3. Presentation of tests conducted and results achieved

a. Response to step signal in three points of the stroke, at constant pressure

The software diagram for determining the response to step signal, developed in LabVIEW, is shown in Figure 5.
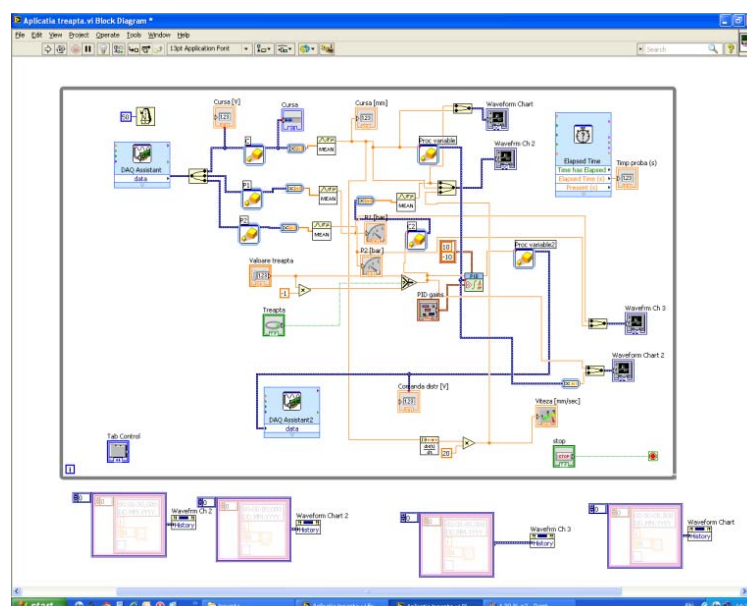

Fig. 5. Software diagram for determining response to step signal, developed in LabVIEW

The tests are conducted at working pressure of 8 bar, in 3 points along the stoke, namely 30%, 60% and 100% of stroke value mentioned by the manufacturer of the actuators, for different values of proportionality factor kc of the PID automatic controller.

In window 1 (screenshot), Figure 6, there are highlighted: prescribed position, achieved position, speed, amplitude variation over time, values of PID parameters of the automatic controller, step value.

In window 2, Figure 7, there are highlighted: pressures in piston chamber -p_1 /rod chamber -p_2, amplitude, values of PID parameters of the automatic controller, step value, time length of the test.

Fig. 6. Window 1 of the application - DNCKE-100-200-PPV-A medium pressure pneumatic actuator

Fig. 7. Window 2 of the application - DNCKE-100-200-PPV-A medium pressure pneumatic actuator

The graphs obtained by running the software, for the two windows of the application, are shown in Figure 8.

Fig. 8. The shape of graphs obtained during tests concerning the response of the DNCKE-100-200-PPV-A medium pressure pneumatic actuator to step signal

b. Response to sine wave signal having initial amplitude, from minimum to maximum value, for three stroke values

The software diagram for determining the response to sine wave signal, developed in LabVIEW, is shown in Figure 9. [2]

The tests are conducted at working pressure of 8 bar, in 3 points along the stoke, namely 30%, 60% and 100% of stroke value mentioned by the manufacturer of the actuators, for different values of proportionality factor kc of the PID automatic controller.
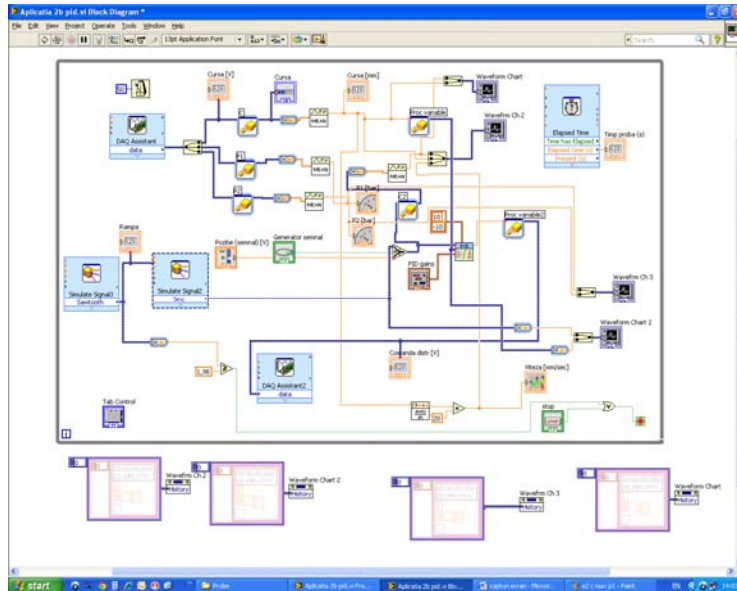
Fig. 9. Software diagram for determining the response to sine wave signal, developed in LabVIEW

In window 1, Figure 10, there are highlighted: prescribed position, achieved position, speed, amplitude variation over time, values of PID parameters of the automatic controller, status of the signal generator.

In window 2, Figure 11, there are highlighted: pressures in piston chamber -p_1 /rod chamber -p_2, amplitude, values of PID parameters of the automatic controller, status of the signal generator, time length of the test.

The graphs obtained by running the software, for the two windows of the application, are shown in Figure 12.
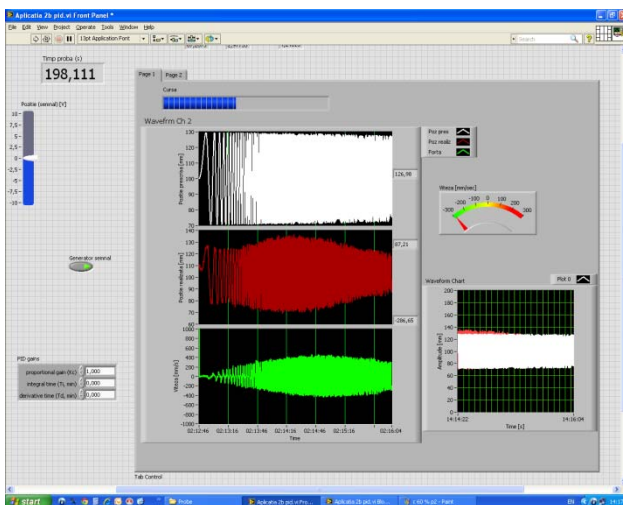
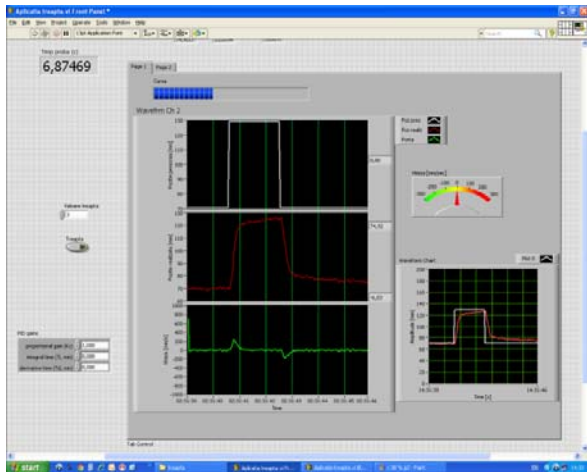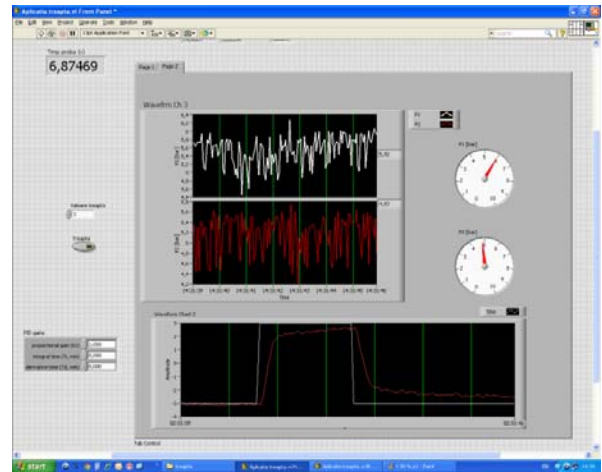**Fig. 10.** Window 1 of the application - DNCKE-100-200-PPV-A medium pressure pneumatic actuator

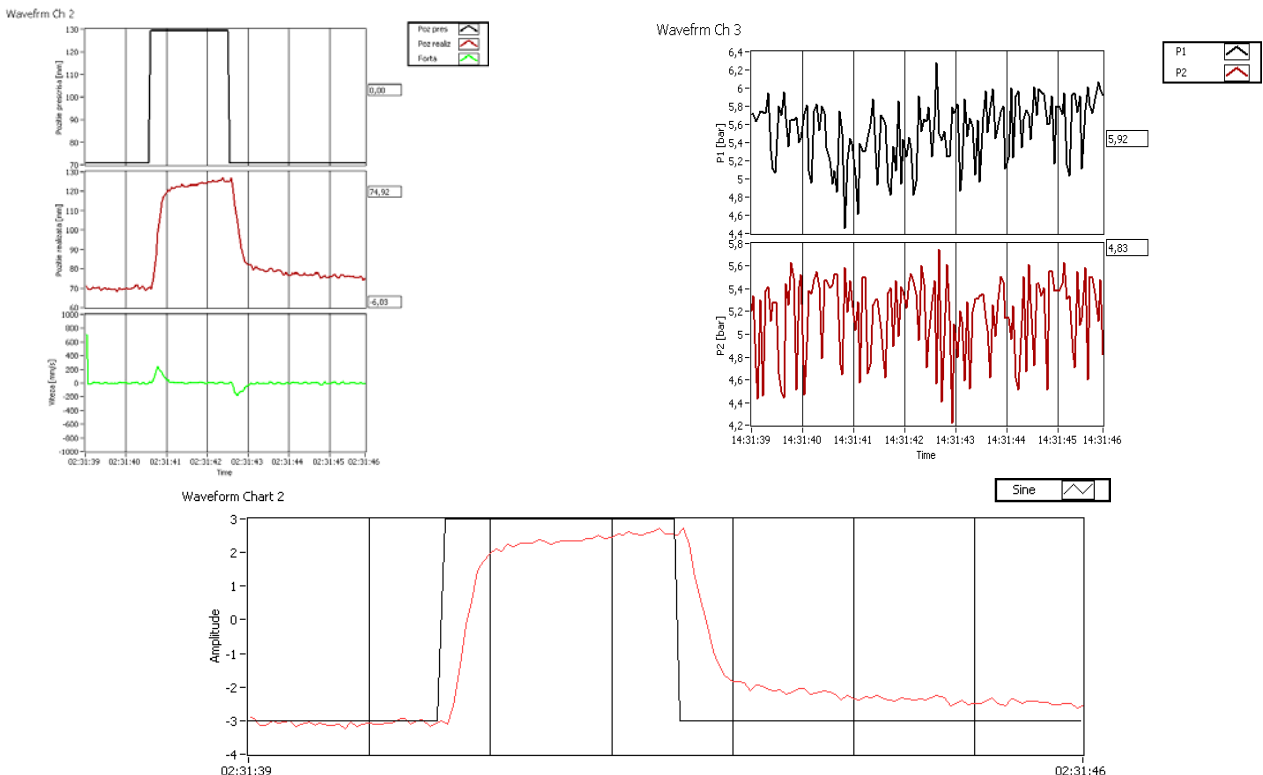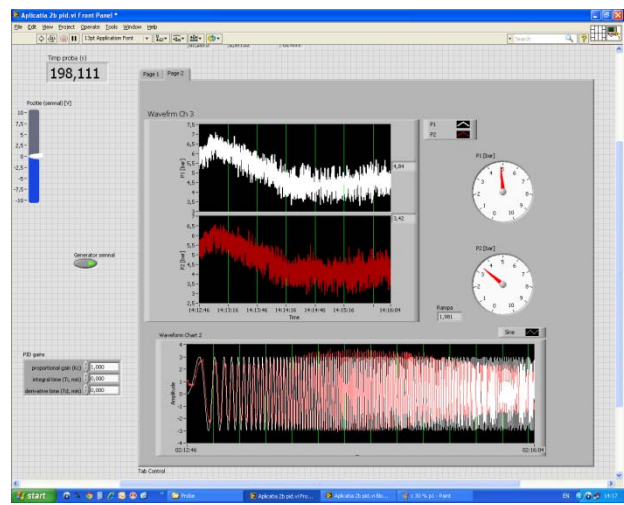**Fig. 11.** Window 2 of the application - DNCKE-100-200-PPV-A medium pressure pneumatic actuator
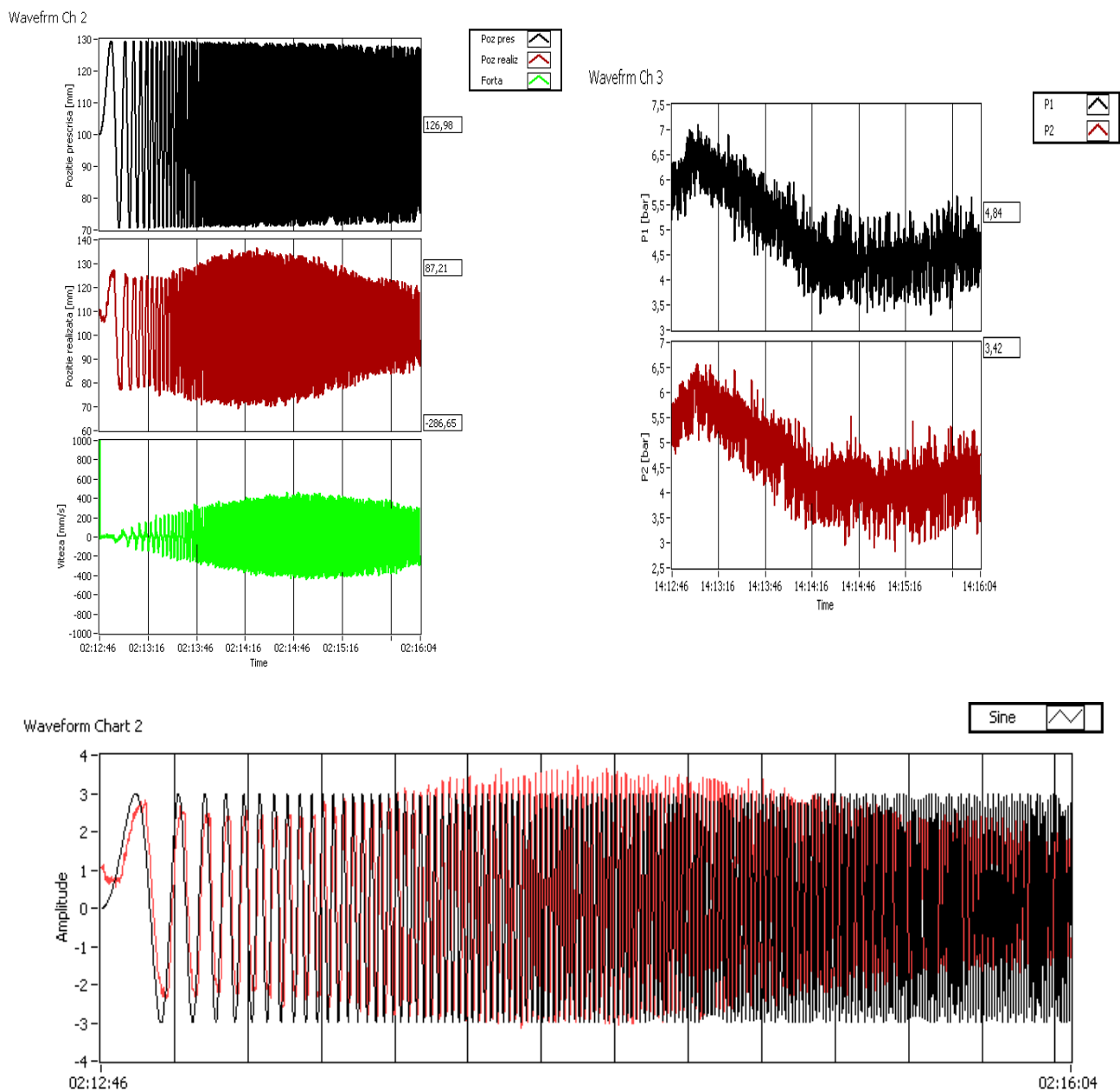
Fig. 12. The shape of graphs obtained during tests concerning the response of the DNCKE-100-200-PPV-A medium pressure pneumatic actuator to sine wave signal

c. Determining the starting pressure

The software diagram for determining the starting pressure, developed in LabVIEW, is shown in Figure 13.

Starting pressure was determined by gradually increasing the supply pressure of the actuator under tests from a ZERO value, while runing the software which tests the response to step signal.[5]

Upon reaching the starting pressure, on the graph of the application there occurs a leap in the step signal.

In the application window, Figure 14, there are highlighted: stroke value, pressures in piston and rod chambers, status of the signal generator, time length of the test.

The graphs highlighting the starting pressure for the piston chamber / rod chamber of the DNCKE-40-130-PPV-A actuator are shown in Figure 15.
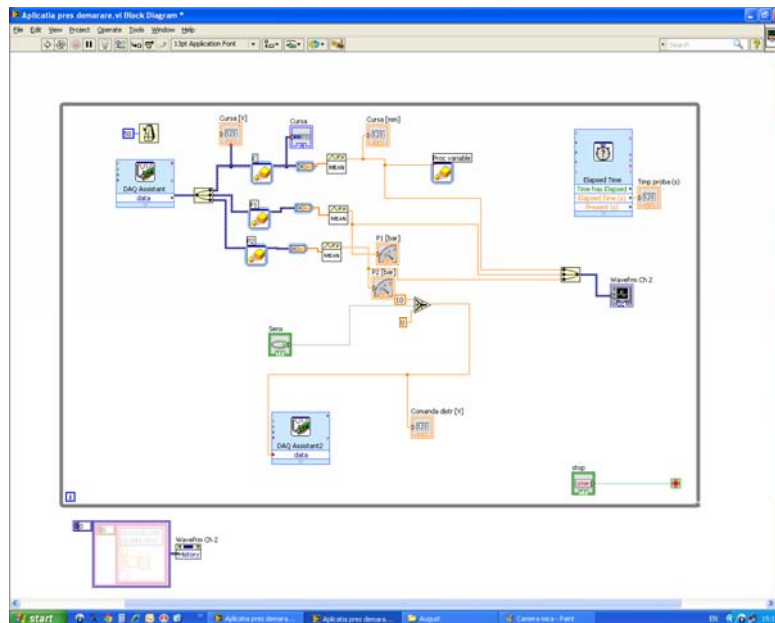
Fig. 13. Software diagram (graphics) for determining the starting pressure
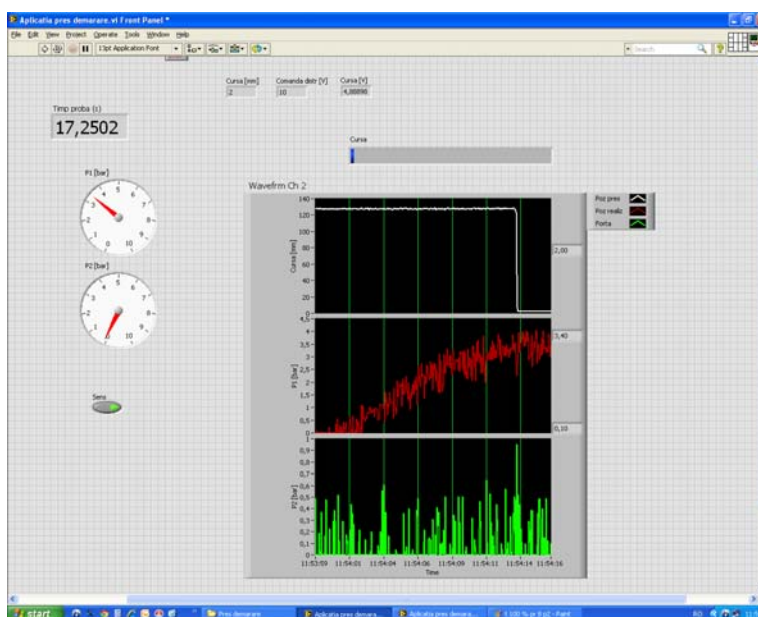
Fig. 14. Window of the application for determining the starting pressure
- DNCKE-40-130-PPV-A actuator

4. Conclusions

1. Experimental research on main factors and methods influencing the dynamic behavior of medium and high pressure pneumatic actuators has been carried out on two dimensional types of medium pressure pneumatic actuators **(DNCKE-100-200-PPV-A**, respectively **DNCKE-40-130-PPV-A)**.
2. Tests concerning the response to step and sine wave signal, determination of starting pressure, influence of parameters of the automatic regulator within the automatic control system (PID) have been run in the LabVIEW environment.

Piston chamber starting pressure   Rod chamber starting pressure
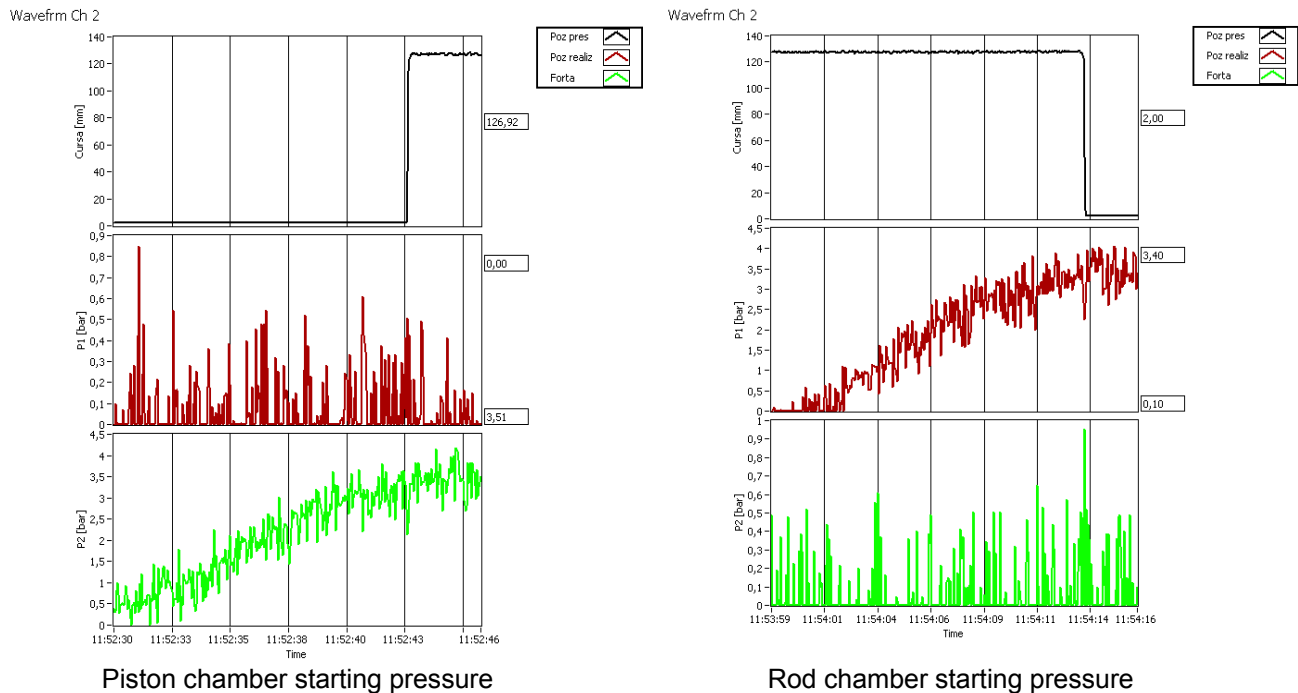
Fig. 15. Graphs of starting pressure for the DNCKE-40-130-PPV-A actuator

3. Influence of sizes, type of seals and the materials they are made of, the level of processing (surface quality of cylinder liners and their rods), quality of working fluid on dynamic performance of actuators has been analyzed on the basis of research performed in the field and presented in scientific literature.

4. Temperature of the working fluid has been maintained rigorously at the standard value of 25 ^{0}C.

5. Working pressure (at the input of actuators' chambers), controlled by the pressure regulator within the air preparation group, has been 8 bar.

6. The automatic controller used has been P (proportional) type, the only variable factor of the automatic control system being the proportionality (amplification) factor k_c.

References

[1] M. Avram, "Acţionări hidraulice şi pneumatice - Echipamente şi sisteme clasice şi mecatronice"/"Fluid Power - Classical and mechatronic equipment and systems", University Press, Bucharest, 2005;

[2] R. Radoi, M. Blejan, I. Dutu, Gh. Sovaiala, I. Pavel, "Determining the step response for a pneumatic cylinder positioning system**",** In: Hidraulica no. 2/ 2014, pp. 25-31, ISSN 1453-7303;

[3] A. Drumea, P. Svasta, "Modelling and simulation of sensors for position control for hydraulic mechatronic systems", 34th International Spring Seminar on Electronics Technology, ISSE2011, May 2011, pp. 622-625;

[4] A. Drumea, R. Al. Dobre, "Modelling, simulation and testing of an autonomous embedded system supplied by a photovoltaic panel", 20th International Symposium for Design and Technology in Electronic Packaging, SIITME2014, October 2014, pp.309-312;

[5] G. Matache, R. Radoi, Gh. Sovaiala, I. Pavel, "Experimental determinations on improving dynamic and energy performance of pneumatic systems"**,** In: Hidraulica no. 2/ 2015, pp. 40-47, ISSN 1453-7303.

Influence of Cutting Parameters on Surface Roughness of Red Brass (C23000) in Turning Using Exponential Model

Assistant Professor **M. Hanief** M.Tech[1], Professor **M. F.Wani**[2] Ph.D

[1] National Institute of Technology, Srinagar, India, hanief@nitsri.net

[2] National Institute of Technology, Srinagar, India, m_f_wanif@nitsri.net

Abstract: *This paper examines the effect of cutting parameters (cutting speed, feed rate and depth of cut) onto the surface roughness of red brass during turning. Mathematical model was developed by using experimental data gathered from a series of experiments, based on full factorial design. The experiments were performed on red brass using HSS tool. Exponential model based on regression analysis were developed in this study. It was concluded from the study that the feed rate is the most dominant factor affecting the surface roughness followed by depth of cut and cutting speed. The model developed was evaluated for its competence using statistical methods, coefficient of determination (R^2), mean absolute error (MAPE) and mean square error (MSE).*

Keywords: *brass, cutting force, regression, surface roughness, turning*

1. Introduction

Brass and brass alloys are widely used as industrial materials because of their excellent characteristics such as high corrosion resistance, non-magnetism and good machinability e.g. in bushes, ball valves, butterfly valves etc. of hydraulic devices. Surface roughness is an important parameter in evaluating the performance of the hydraulic equipment [1]. It is necessary to achieve a desired surface topography of a mechanical component during the machining operation, as the surface roughness influences significantly its tribological properties during its useful life. Good surface finish improves the wear and friction characteristics and also increases the fatigue life of a component. In order to predict surface roughness of a mechanical component it is essential to develop an appropriate mathematical model. Surface finish in turning has been found to be influenced in varying amounts by a number of factors such as feed rate, work material, characteristics, work hardness, unstable build up edges, cutting speed, depth of cut, cutting time, tool nose radius and cutting tool edge angles, stability of machine tool and workpiece-setup, chatter and use of cutting fluid [2]. Surface roughness is mostly based on cutting parameters (cutting speed, feed, and depth of cut) and sometimes some other parameters [3]. The various models for optimum surface roughness have been reported in the literature. These models are based on: multi regression technique, physics of the process, fuzzy set based technique, Neural network modeling (NNM) [4]. [5] used multiple regression to predict the surface roughness during hard turning of AISI 4340 steel. [6] investigated the effect of cutting parameters (cutting speed, feed rate and cutting time) on surface roughness and flank wear during the turning of AISI H11, using response surface methodology (RSM). [7] studied the performance and wear behavior of different cubic born nitride tools in finish turning of AISI 52100 steel. [8] developed ANN models to study the effect of cutting conditions on the surface roughness in turning of free machining steel. This necessitates a cutting process optimization to determine the optimal values of the cutting parameters, such as cutting speed, feed rate and depth of cut to fully evaluate the performance and life of the cutting tool. The literature survey reveals that lot of work has been done to model the surface roughness in turning operation using linear regression models, power law models, ANN etc. Conventionally ANOVA has been used to determine the influence of the cutting parameters on the surface roughness. The present paper intends to develop a model based on exponential law and demonstrates how the influence of the cutting parameters can be found without using ANOVA.

2. Experimentation and the exponential model

In this study, cylindrical red brass bars of diameter 30mm and 150mm length as work piece material and HSS tool were used. The experiments were performed on ***Kiloshkar Enterprise 1550*** make lathe under dry conditions. A total of 27 (3^3) experiments were conducted on the basis of full factorial design methodology. The parameter chosen for the study were feed rate, cutting speed and depth of cut. The surface roughness was measured by ***Hommel Etamic WS*** roughness meter. The details of the data obtained from the experiments for red brass are given in Table. 1.

TABLE 1: Experimental data for model construction

Feed rate(mm/rev)	Depth of cut(mm)								
	v=840 (mm/min)			*v=1000 (mm/min)*			*v=1280 (mm/min)*		
	0.10	0.13	0.16	0.10	0.13	0.16	0.10	0.13	0.16
0.40	2.610	2.906	3.126	2.396	2.646	3.271	3.076	3.318	3.566
0.80	2.569	2.532	2.542	2.426	2.626	2.919	2.666	2.854	3.081
0.12	2.896	3.064	3.093	2.856	3.105	3.573	3.296	3.210	4.109

The model of predicted surface roughness, R_a can be expressed as Eq. 1

$$R_a = k \prod_{i=1}^{n} p_i{}^{c_i} \tag{1}$$

where p_i, and c_i $i = 1,2,3 \dots n$ are the model parameters and cutting parameters respectively.

Eq. (1) can written as

$$R_a = k p_1{}^{c_1} p_2{}^{c_2} p_3{}^{c_3} \dots \dots p_n{}^{c_n} \tag{2}$$

The parameters considered in the present study were cutting speed (*v*), feed rate (*f*) and depth of cut (*d*). Thus Eq. (2) can be written as

$$R_a = k \, p_1{}^{v} p_2{}^{f} p_3{}^{d} \tag{3}$$

using logarithmic transformation, Eq.(3) can be written as Eq. (4).

$$\ln R_a = \ln k + v \ln p_1 + f \ln p_2 + d \ln p_3 \tag{4}$$

$$Y_r = a_o + a_1 v + a_2 f + a_3 d \tag{5}$$

The model parameters in Eq. (5) were obtained by least square method ($\mathbf{c} = (\mathbf{X^T X})^{-1} \mathbf{X^T Y}$). Accordingly Eq.(6) was obtained.

$$R_a = 1.7739 \times 1.0003^{v} \times 10.8528^{f} \times 0.764^{d} \tag{6}$$

3. Results and discussion

The experimental and predicted surface roughness is shown in Fig.(1). It is clear from the Fig(1) that the predicted and experimental values of surface roughness are very close to each other. The accuracy of the proposed model was assessed by the statistical methods using coefficient of regression (R^2) mean square error (MSE) and mean absolute error (MAPE) as tabulated in Table 1.

TABLE 2: Statistical parameters of proposed model

R^2	MSE	MAPE
99.84%	0.4035	3.2254%

It is clear from the Table. 1 that the proposed model has very high coefficient of determination R^2, very small mean square error and mean absolute percentage error . These parameters of the model are indicative of the fact that the model is capable to predict the surface roughness with high

accuracy. In order to find the influence of each machining parameter on surface roughness Eq. (6) was used to evaluate

$$\left(\frac{\partial R_a}{\partial f}\right)_{d,v}, \quad \left(\frac{\partial R_a}{\partial d}\right)_{f,v} \text{ and } \left(\frac{\partial R_a}{\partial v}\right)_{d,f}$$
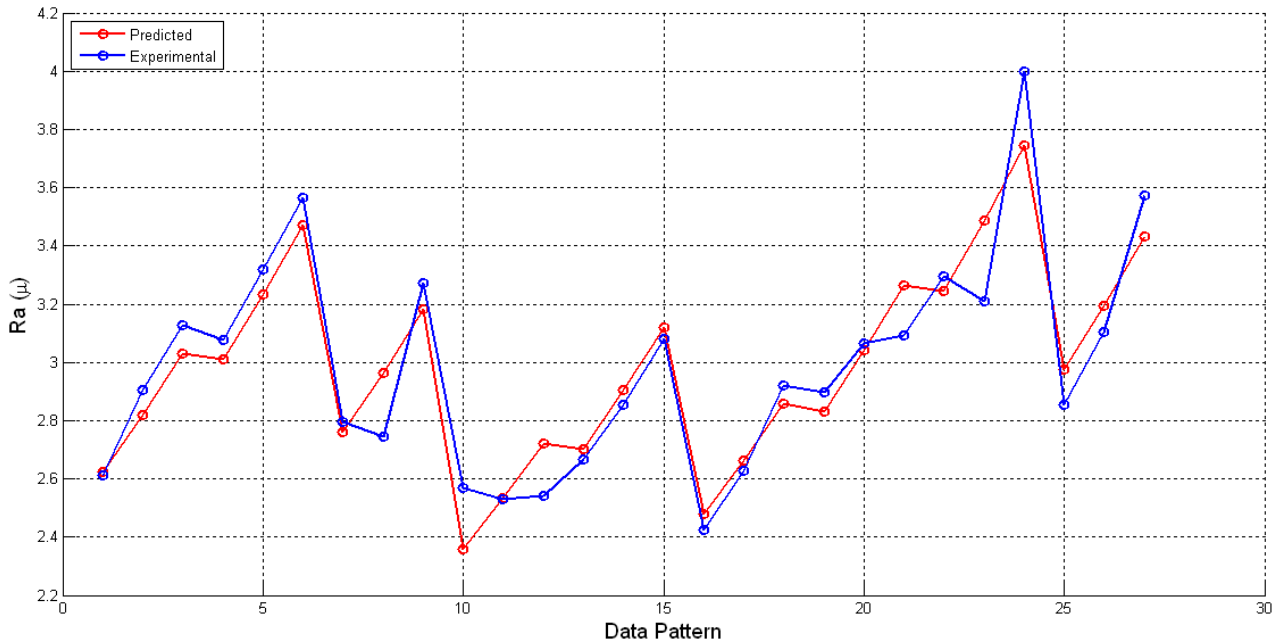

Fig.1. Predicted and experimental values of surface roughness

It was found that

$$\left|\left(\frac{\partial R_a}{\partial f}\right)_{d,v}\right| > \left|\left(\frac{\partial R_a}{\partial d}\right)_{f,v}\right| > \left|\left(\frac{\partial R_a}{\partial v}\right)_{d,f}\right| \qquad (7)$$

It was concluded from Eq. (7) that the most dominant factor that influences surface roughness, R_a is feed rate, *f* followed by depth of cut, *d* and least by .cutting speed, *v.* Also

$$\left(\frac{\partial R_a}{\partial f}\right)_{d,v} > 0, \qquad \left(\frac{\partial R_a}{\partial d}\right)_{f,v} < 0 \qquad and \left(\frac{\partial R_a}{\partial v}\right)_{d,f} > 0$$

The above inequalities indicate that the surface roughness increases with increase in feed rate and cutting speed and decreases with increase in depth of cut.

4. Conclusions

The present investigation focused on surface roughness prediction and analysis during turning of red brass using HSS tool. This analysis was carried out by developing surface roughness model of *Ra* using exponential function with feed rate, speed and depth of cut as process parameters. The model developed has only four unknown model parameters. The existence of highly non-linear relationship between the surface roughness and process parameters justifies the use of exponential function. On the basis of R^2, MAPE and MSE it was concluded that the model is in good agreement with the experimental data. It was also concluded from the analysis that the surface roughness is highly sensitive to the feed rate.

References

[1] Lorena Deleanu, "A simplified model for partial journal and water lubrication", Hidraulica, No1-2, (June, 2011), pp. 71-77;

[2] Suresh, P. V. S., Venkateswara Rao,P., Deshmuhk, S. G., "A Genetic Algorithmic Approach for Optimization of Surface Roughness Prediction Model", International Journal of Machine Tool and Manufacture, 42 (2002) 675-680;

[3] Cakir M. Cemal, Cihat Ensarioglu, Ilker Demirayak, "Mathematical Modeling of Surface Roughness for Evaluating The Effects of Cutting Parameters and Coating Material", Journal of Materials Processing Technology, 209, (2009) 102-109;

[4] Asilturk Ilhan and Mehmet Cunkas, "Modeling and Prediction of Surface Roughness In Turning Operations Using Artificial Neural Network and Multiple Regression Method", Journal of Expert Systems with Applications, 38, (2011) 5826-5832;

[5] Agrawal Anupam, Saurav Goel, Waleed Bin Rashid and Mark Price, "Prediction of surface roughness during hard turning of AISIS 4340 steel (69 HRC)", Applied Soft Computing, 30 (2015) 279-286;

[6] Aouici Hamdi, Mohamed Athmane Yallese , Brahim Fnides, Kamel Chaoui and Tarek Mabrouki, "Modeling and optimization of hard turning of X38CrMoV5-1 steel with CBN tool: Machining parameters effects on flank wear and surface roughness", Journal of Mechanical Science And Technology, 25(11) (2011) 2843-2851;

[7] Chou. Y. K., Evans, C. J., and Barash, M. M., "Experimental investigation on CBN turning of hardened AISI 52100 steel, Journal of Materials Processing Technology". 124, (2002) 274-283;

[8] Davim, J. Paulo, Gaitonde, V. N., Karnik, S. R., "Investigations into effect of cutting conditions on surface roughness In Turning Of Free Machining Steel by ANN Models". Journal of Materials Processing Technology, 205, (2008) 16-23.

Flow through Command Hydraulic Resistance

Dipl. Eng. **Ioana SFARLEA**[1]**,** PhD. Eng. **Lucian MARCU**[1]**,** PhD. Eng. **Daniel BANYAI**[1]

[1] Technical University of Cluj-Napoca, sfarlea.ioana@termo.utcluj.ro

Abstract: *The growing usage of hydraulic servo technique involves optimizing the elementary components of these types of devices. The paper presents the results of a study on hydraulic resistance, achieved by mathematical modeling and numerical simulation, CFD. We have studied three types of bushings and 3 types of piston forming different geometric resistant fed in turn with three different pressure values. There are shown the formation and dissipation of fluid jets that appear in the flow through the variable resistance.*

Keywords*: CFD, hydraulic resistance, servo-hydraulics*

1. Introduction

Precision hydraulic actuators have the beginnings in 1955, when J.F. Blackburn publish at Massachusetts Institute of Technology the "Fluid Power Control". The importance of this research lies in the fact that the work founded the servo-hydraulics, marking the moment when the conventional hydraulic actuators were developed for servo drives (servo-hydraulic) and then for proportional hydraulics. The difference between proportional hydraulic equipment or servo-hydraulic and classic hydraulics is in the first two cases, by opening a variable hydraulic resistance the flow can be controlled continuously, eventually, the velocity of the fluid in a hydraulic system. This cannot be achieved in conventional hydraulics. The difference between proportional and servo-hydraulic equipment is represented by technological achievements and the coverage of the hydraulic resistance (Fig.1).

As shown in Fig. 1, for zero coverage, the width of the sleeve, t, and the width of the spool, a, are equal, t>a of the negative cover and t <a for positive coverage. The appearance of the coverage is reflected in the variation of the flow rate, according to the opening resistance. Thus, for negative coverage, the middle position is characterized by a flow, Q_0. Positive coverage is characterized by a movement, y_0 for which there is no flow. It is noted that the only situation in which for a reference displacement, y occurs flow and movement of the spool without parasite flow Q_0 if coverage is "0". The usage of zero coverage resistances was limited at first by the technological possibilities for achieving them. This is why the proportional hydraulics technique was used. The years 1970-1990 were characterized by proportional hydraulics research. The technological advances of the last decades have led to the use of systems "servo" research in medical and energy production directions [1],[4],[5].
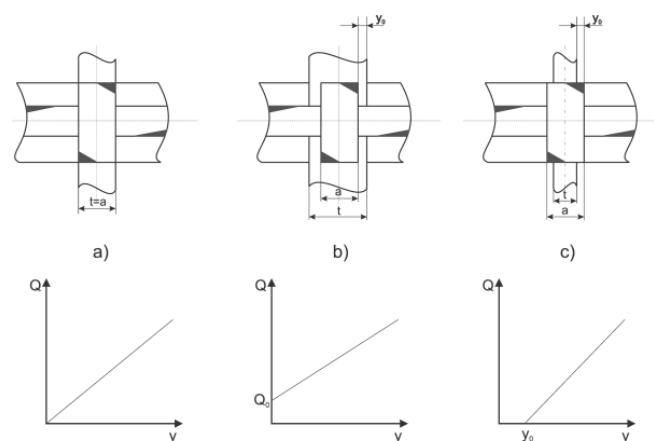

Fig. 1. Flow variation depending on spool displacement a) zero coverage (servo-hydraulics); b) negative coverage (conventional hydraulics); c) positive coverage (proportional hydraulics)

2. Objectives

At the base of the manufacture of hydraulic energy control equipments, also called hydraulic control valves are the resistances. Given this and the fact that there are targeted superior static and dynamic performances, there is made an in-depth study and research of all aspects influencing parameters for fluid flow through the hydraulic resistance. The need to know these issues is given primarily by the automation of the industrial process, where hydraulic systems are in big number of applications. Also the predictability of the static and dynamic behaviour of hydraulic power control devices require knowledge of these issues.

This paper proposes to study the static and dynamic behaviour of a hydraulic resistance with spool and sleeve with holes, based on numerical simulations. The numerical simulations conducted will help to understand, visualize and analyze the phenomena occurring, during the fluid flow through hydraulic resistance formed. Thus, they are traced and can be interpreted the fields and gradients of pressure and velocity. It will be analyzed the formation of fluid flow and of vortices, where the situation will be such.

The program involves geometric modeling numerical simulation of hydraulic resistance sleeve with holes and spool design using SolidWorks software and then was used the module Fluent, ANSYS.

The study objective is to optimize the sleeve's holes geometry, so for small openings command to have turbulent regime, the hydrodynamic forces as smaller as possible, and, where possible, to avoid the appearance of cavitation. Numerical analysis of CFD (Computational Fluid Dynamics) helps us in this regard by viewing flow and phenomena that occur during it without actually manufacture the resistance.
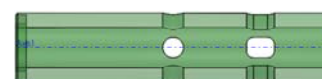
3. Mathematical modeling

To study the flow through hydraulic resistance spool and sleeve with holes were designed several CAD models. A body has been modeled, three types of sleeve holes (circular, rectangular and triangular), and three patterns of piston (control edge bevel at 30°, 45° or 60°), there were made various combinations of these, to study the flow through them. The inlet pressure was considered 20 bar, 30 bar, 35 bar and 40 bar, the control openings of 0.1 mm, 0.2 mm, 0.3 mm, 0.4 mm and 0.5 mm. Was chose, small openings control, because in this area the effects of hydrodynamic force disrupts the dynamic behaviour but also because of the potential of cavitation due to pressure drop.

The simulations that will be presented below are made for the following combinations: circular holes and piston 30°, 45° or 60°, rectangular holes and piston 30°, 45° or 60° and triangular holes and piston 30°, 45°, 60° respectively at all openings and input pressures considered above.

The geometric models were designed using SolidWorks software and the simulations being carried with Fluent, ANSYS. The steps that were followed are: Defining the computational domain (representing the physical space), Defining the hydraulic oil used, Meshing the fluid domain. Figures 2 and 3 show the models of sleeve or piston used.
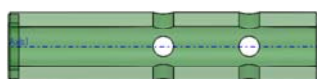
a) cylindrical holes   b) rectangular openings

c) triangular openings

Fig. 2. Sleeves used

a) 30°   b) 45°
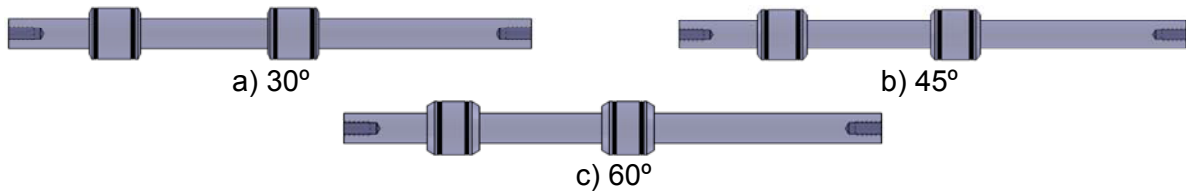
c) 60°

Fig. 3. Pistons

From the imposed boundary conditions point of view, which have been implemented only by the values of the input or the output of the fluid. In this case, the input pressures were 20e5 Pa, Pa 30e5, 35e5 Pa, Pa 40e5 and 101325 Pa output pressure (atmospheric pressure); was considered a hydraulic fluid density ρ_{oil} = 876 kg/m^3 and kinematic viscosity v = 45cSt.

Turbulent flow is characterized by the variations in the speed fields, which mix the transported sizes, such as momentum and energy. The turbulence models help to simulate these fluctuations. The turbulence model chose for this study was, k-ε RNG (Renormalization Group). This model of turbulence arising from model k-ε, bringing the latter improved by including a term in addition to the equation ε, which gives a significant increase in precision and by implementing the theory of renormalization, which lets us to get satisfactory results if there are small Reynolds numbers [2].

In addition to the turbulence equations proposed, for the accurate modeling of flow the mathematical model contains also the continuity of mass equations, the Navier-Stokes equations (conservation of momentum) and the equation of speed in any point of the fluid.

$$\frac{\partial x}{\partial t} + \frac{\partial y}{\partial t} + \frac{\partial z}{\partial t} = 0$$

$$\begin{cases} \dfrac{\partial v_x}{\partial t} + V_x \dfrac{\partial v_x}{\partial x} V_y \dfrac{\partial v_x}{\partial y} + V_z \dfrac{\partial v_x}{\partial z} = f_x - \dfrac{1}{\rho}\dfrac{\partial p}{\partial x} \\[2mm] \dfrac{\partial v_y}{\partial t} + V_x \dfrac{\partial v_y}{\partial x} + V_y \dfrac{\partial v_y}{\partial y} + V_z \dfrac{\partial v_y}{\partial z} = f_y - \dfrac{1}{\rho}\dfrac{\partial p}{\partial y} \\[2mm] \dfrac{\partial v_z}{\partial t} + V_x \dfrac{\partial v_z}{\partial x} + V_y \dfrac{\partial v_z}{\partial y} + V_z \dfrac{\partial v_z}{\partial z} = f_z - \dfrac{1}{\rho}\dfrac{\partial p}{\partial z} \end{cases} \qquad (1)$$

$$v = v_0 * tgh\left(\frac{t}{T}\right)$$

$$v = v_0\left(\frac{r}{R}\right)^{\frac{1}{7}}$$

where: v_0 the velocity of fluid at input;
$v_{x,y,z}$ – the velocity about Ox, Oy and Oz.

4. Numerical analysis

Regarding the flow regime, investigations start from the need of a turbulent regime, a flow coefficient (α) constant with a value as close to 1, it includes the value all hydraulic resistance. It is known that the proportionality between flow and the opening control is ensured only if both the pressure difference and flow coefficient are constant [3].

Flow coefficient, α, is constant only in turbulent flow regime. It will not depend on Re, but will be heavily influenced by the pressure difference. It is necessary to avoid laminar regime, as it depends on the temperature and thus the viscosity of the oil [3].

In the following part will be presented numerical simulation of the studied models. The fields are shown in a longitudinal section through the center of interest. Figure 4 is intended to highlight the fields studied.

a)   b)

c)
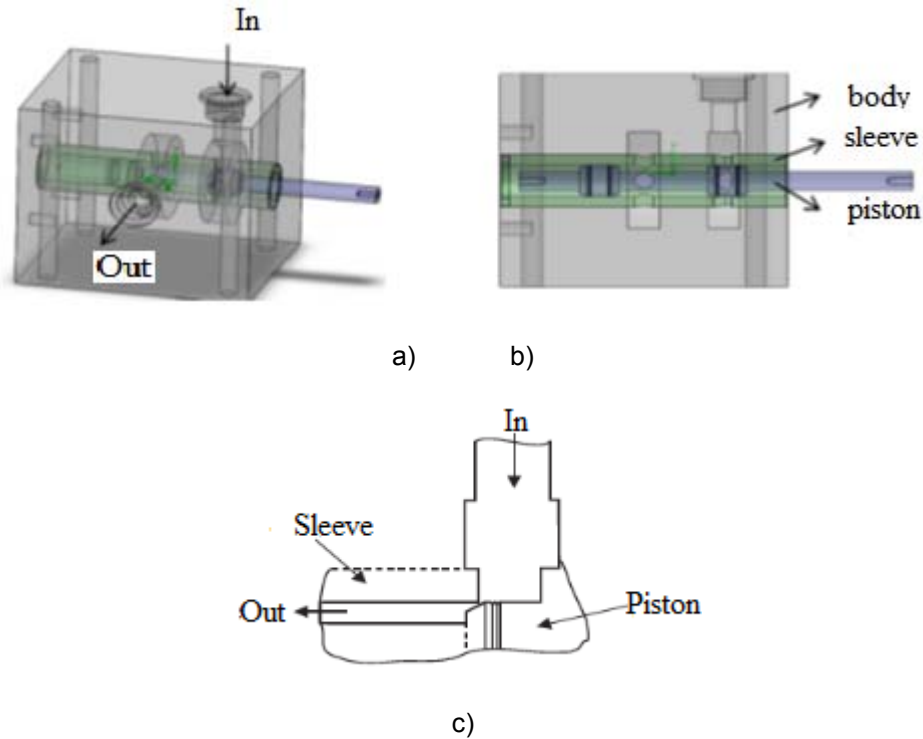
a) Overview b) Longitudinal section through the middle of the aperture c) Section for displaying the results

Fig. 4. Hydraulic resistance assembly

Fig. 5 shows the distribution of the pressure inside the hydraulic resistance that is formed in the whole body, sleeve with rectangular holes and piston with the control edge chamfered at 30°. Representations are available for opening 0.2 mm at various inlet pressures.
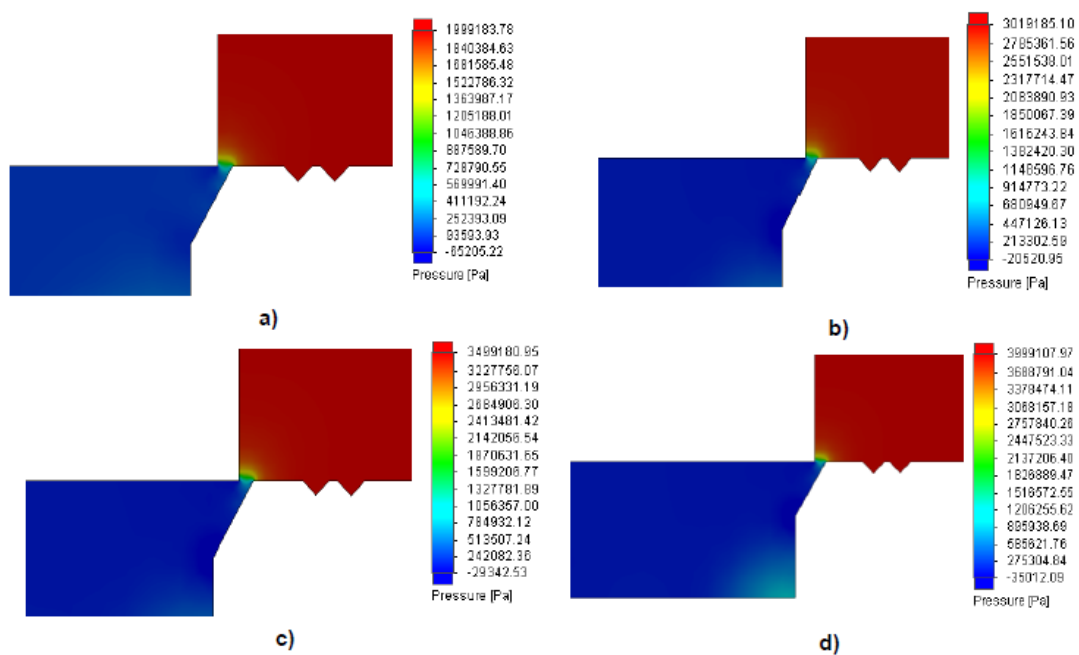

Fig. 5. Pressure field (rectangular holes, and the active edge chamfered at 30 °. Inlet pressure: a) 20 bar; b) 30 bar; c) 35 bar; d) 40 bar.

In Fig. 6 is shown the speed distribution of the assembling with three sleeves having holes with a control edge chamfered at 30°. Opening command is 0.2 mm and the inlet pressure is 20 bar. The highest values were recorded for the combination of the sleeve with cylindrical apertures, about 69 m/s (Fig. 5a), then assembling the sleeve with triangular openings, about 67 m/s (Fig. 5c), and the low speed values occurred at the rectangular holes, 66 m/s (Fig. 5b). It is noted that the values are close but very different the form of the jet that cross the considered resistance. As if a) the jet is dispersed almost immediately after passing the resistance, in the other two situations the jet is "sticking" to the walls of the spool, much more when the sleeve have rectangular holes. Also in the latter two cases, recirculation zone is observed, which leads to slower the oil flow.
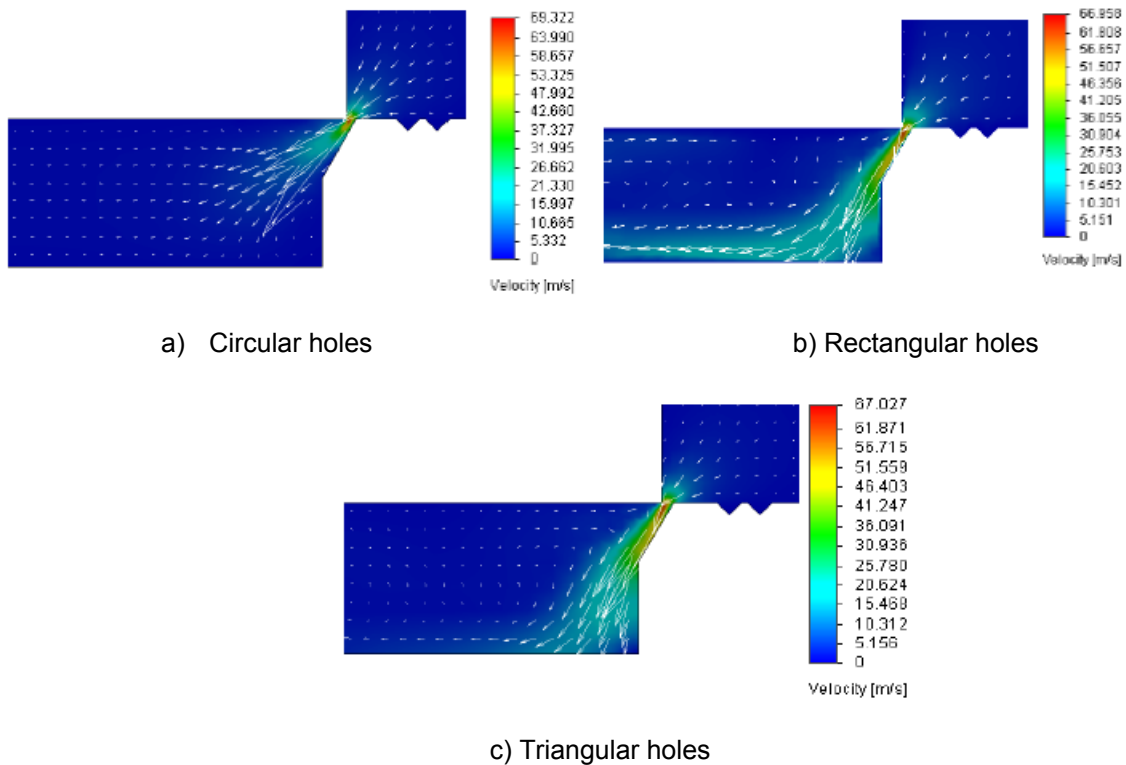

a)   Circular holes   b) Rectangular holes

c) Triangular holes

Fig. 6. Velocity distribution for 30° chamfer

The velocity field is compared if inlet pressure is 40 bar and active edge sloping at 45°; the conclusions drawn from the analysis of all results obtained by combining together the 3 pistons 3 bushings, with a pressure of 20, 30, 25, 40 bar, for a small opening of 0.2 mm are presented in the following.
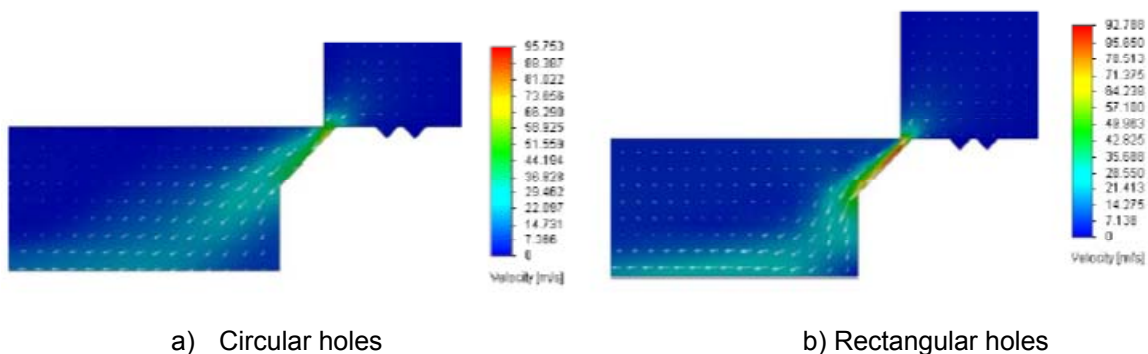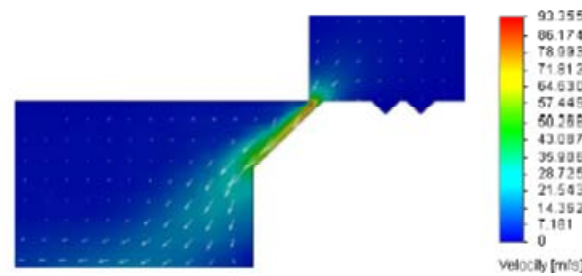

a)   Circular holes   b) Rectangular holes

Fig. 7. Velocity distribution for 45° chamfer

c) Triangular holes

Fig. 7. Velocity distribution for 45° chamfer (continued)

5. Conclusions

As seen in the pressure field in each case there is a sudden pressure drop in the minimum section, reaching negative values. This is an alarm in the occurrence of cavitation phenomenon.

As the value of the inlet pressure increases, it is evident that the velocity of the oil will increase the value. Regarding the speed values recorded, the results provided by simulations is not much different between them, regardless of the geometry of the hole.

According to the orientation of the velocity vector and the jet shape, it can be seen that in the case of circular apertures the fluid jet is dispersed almost uniformly on the surface of the sleeve and spool, when leaving the beveled edge. In the other two cases, the fluid stream tends to be closer to the edge of the control spool; in the assembly of sleeve with rectangular apertures, the fluid jet is observed as it is joined to both the sleeve and the plunger. This aspect allows the formation of vortices in the upper part of the enclosure.

In the case of the sleeves with circular and triangular holes, the fluid jet is sticking by the control edge of the hydraulic resistance. When the jet reaches the stem of the spool, it begins to fall apart. For the case of the sleeve with rectangular apertures, the jet of fluid is attached to both: the control edge and its rod. It also appears, a fluid recirculation due to the meeting with the second control section of the spool, eddies areas where fluid decelerates.

For chamfered edge at a greater angle, the oil speed increases through resistance which leads to a decrease in static pressure in the minimum section pass.

References

[1] C. Dumitrescu, C. Cristescu, I. Nita, G. Matache, I. Ilie, "Considerations regarding the use of hydraulic and pneumatic trackers for photovoltaic panels to convert solar energy directly into electric energy", Proceedings of International Multidisciplinary Scientific Geo-Conference SGEM-2013, 2013, Albena Co., Bulgaria, Vol.: "Energy and clean technologies", pp. 77 – 84, ISBN 978-619-7105-03-2, ISSN 1314-2704;
[2] C.H. Shin, "A numerical study on the characteristics of transient flow in a pressure regulator resulting from closure of the pressure control valve", Journal of Mechanical Science and Technology, 02/2013; 27(2). DOI: 10.1007/s12206-012-1257-y;
[3] D. Opruta, L. Vaida, H. Hedesiu, "The influence of the geometric configuration of the hydraulic command resistances upon the cavitational phenomena", Proceedings of First National Conference on Recent Advances in Mechanical Engineering, September 17-20, 2001, University of Patras, Greece, Volume: 1;
[4] G. Matache, P. Drumea, M. Comes, I. Ilie, "Echipament proportional de reglare a presiunii", Hidraulica Magazine no. 1 /2005 – ISSN 1453-7303, pp.76-79;
[5] L. Vaida, L. Nascutiu, D. Potolea, C. Vaida, D. Opruta, "Techniques for the reduction of noise and vibrations for axial piston pumps", Conference: Experimental Fluid Mechanics 2006, EMT06, Liberec.

Study on the Dynamics of the Tilling Aggregate

Ph.D.St.Eng. **Cristian NUȚESCU**[1], Lect.Ph.D.Eng. **Iulian-Claudiu DUȚU**

[1] University Politehnica of Bucharest, cristiannutescu@yahoo.com

Abstract: This paper has as main subject presenting some theoretical and experimental researches regarding the dynamic behaviour of the tilling aggregates. These are made of a tractor and an attached plow that allow emphasizing the influence of the work width adjustment system over the dynamics of the tilling aggregates when moving on different types of soil, in different work conditions.

Keywords: dynamics, tilling, aggregate

1. Introduction

External forces acting on a vertical-longitudinal plane on a tilling aggregate that has an accelerated motion when climbing on a tilted surface at an angle of *α*, in respect to the horizontal, represents the equivalent dynamic model of the aggregate.

In this paper there are presented a theoretical research over the dynamics of the towed tilling plow and a theoretical research of the dynamics of the tilling aggregate made of a tractor and a towed plow with and without the copying wheel.

2. Theoretical researches on the dynamics of the towed plow

In Figure 1 there is presented an equivalent dynamic model [1], [2] of a towed plow with three mouldboards that is moving with an accelerated motion on a soil with tilted surface at an angle of *α*, in respect to the horizontal. The plow is equipped with a copying wheel and it is attached to the suspension mechanism in three points.
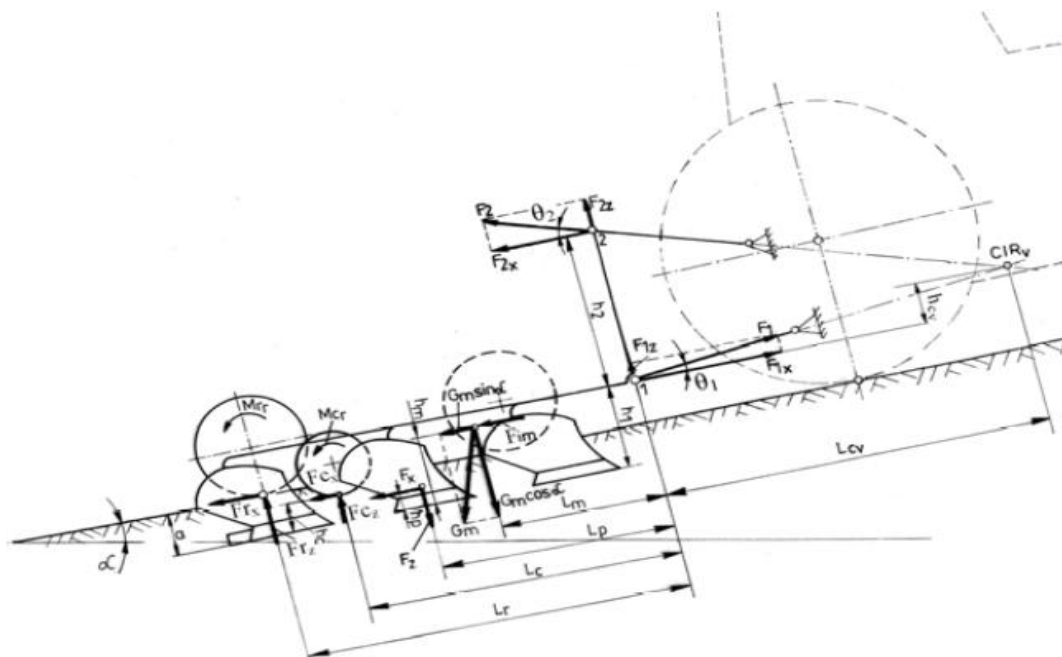

Fig. 1. Diagram of the forces acting on the towed plow, with copying wheel,
in vertical-longitudinal plane when moving with accelerated motion on a tilted terrain

Instantaneous rotation centre in vertical plane, CIR_y, is located at the intersection point of the central axel axis with the lower axels plane. The plow has the working depth of *a*; working width of a mouldboard is *b* (working width of the plow is B = 3b) [1].

Component F_x, parallel to soil's surface, represents the traction resistance force of the plow, that can be experimentally determined (through field or laboratory measurements) or through analytical calculus using the following equation:

$$F_x = k \cdot a \cdot b \cdot n \tag{1}$$

where:
  k – global specific tilling resistance coefficient;
  a – working depth;
  b – working width of the first mouldboard;
  n – total number of mouldboards.

Component F_z, perpendicular to soil's surface, of the tilling resistance force is determined using:

$$F_z = F_x \cdot \tan \beta \tag{2}$$

where:
  β – angle between the two components of the tilling resistance force.
  For normal working conditions, it is considered that:

$$F_z = (0,2 \dots 0,3) \cdot F_x \tag{3}$$

The force acting on the disc knife has two components: one parallel with soil's surface, F_{cx}, and one perpendicular to soil's surface, F_{cz}. The dependency between the two components of the cutting resistance force is given by:

$$F_{cx} = F_{cz} \cdot f_c \tag{4}$$

where:
  f_c – rolling resistance coefficient of the disc knife.

The force acting on the copying wheel has two components: one parallel to soil's surface, F_{rx} and one perpendicular to soil's surface, F_{rz}. Component F_{rx} represents the rolling resistance force of the copying wheel, being dependent on the size of the copying wheel, on the soil's characteristics and on the wheel load [3]. The dependence between the two components of the resistance force that acts on the copying wheel is given by:

$$Fr_x = Fr_z - f_r \tag{5}$$

where:
  f_r – rolling resistance coefficient of copying wheel.

Components of the forces F_1 and F_2 acting on coupling points 1 and 2 of the suspension mechanism axels onto the aggregate's chassis can be written to each other using equations (6) and (7):

$$F_{1z} = F_{1x} \cdot \tan \theta_1 \tag{6}$$

$$F_{2z} = F_{2x} \cdot \tan \theta_2 \tag{7}$$

Given the above, the equilibrium equations can be written as:

$$F_{1x} - F_{2x} - F_{im} - G_m \sin \alpha - F_x - F_{cz} \cdot f_c - F_{rz} \cdot f_r = 0 \tag{8}$$

$$F_{1x} \cdot \tan \theta_1 + F_{2x} \cdot \tan \theta_2 - G_m \cdot \cos \alpha - F_x \cdot \tan \beta + F_{c2} + F_{rz} = 0 \tag{9}$$

$$F_{rz} \cdot [l_r + f_r(h_1 - a)] + Z_c \cdot [l_c + f_c(h_1 - h_c)] + F_x \cdot (h_1 - h_p - l_p \cdot \tan \beta) +$$
$$+ G_m[(h_1 - h_m) \cdot \sin \alpha - l_m \cdot \cos \alpha] + F_{im}(h_1 - h_m) - F_{2x} \cdot h_2 - Mr_r - Mc_r = 0 \quad (10)$$

The system formed by the equations (8), (9) and (10) is a linear system [2] having three unknowns and can be a compatible determined system, the unknowns being the forces acting on the coupling points 1 and 2 of the suspension mechanism axels onto plow's frame (F_{1x}, F_{1z}, F_{2x} and F_{2z}) and the forces acting on the copying wheel (F_{rx}, F_{rz}) and M_{rr} torque. Solving through algebraic methods the system of equations it can be found the three unknowns: F_{1x}, F_{2x} and Fr_z.

3. Theoretical researches on the dynamics of the tilling aggregate made of a tractor and a towed plow with copying wheel

In this case, the plow is equipped with a copying wheel and it is attached to the suspension mechanism with three coupling points (functioning in a floating regime), having the instantaneous center of rotation in vertical-longitudinal plane, CIR_v, located at the intersection point of the central axel's axe with the lower axels plane.
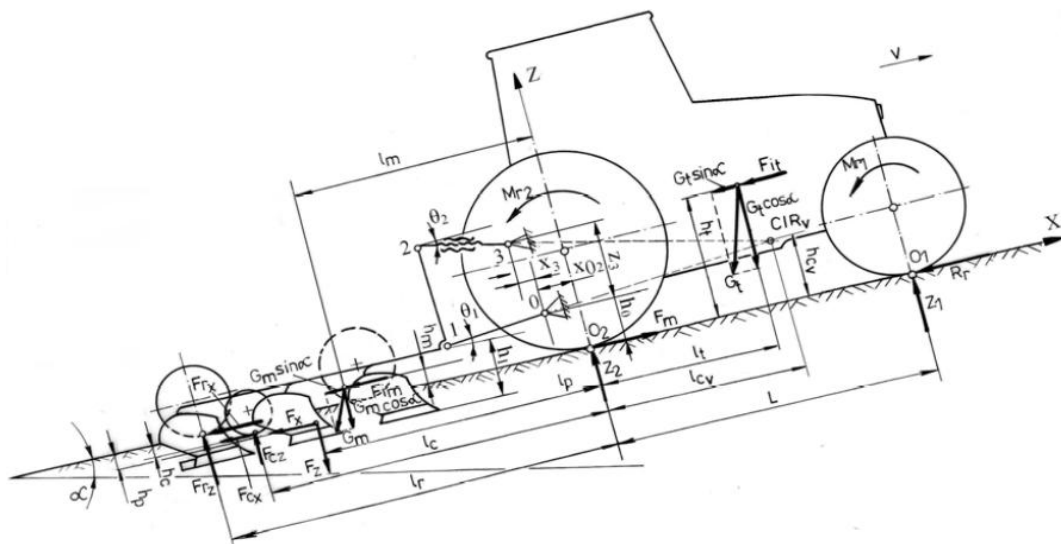

Fig. 2. Dynamic model, in vertical-longitudinal plane, of the tilling aggregate with towed plow equipped with a copying wheel (without automatic adjustment)

It is given a system of coordinates XOZ, having its origin in point O_2, representing the point of contact with the soil of the rear axel's wheels, where OX axis is parallel to the moving direction of the aggregate.
Therefore:

$$G_t = m_t \cdot g \tag{11}$$

where:

    G_t – tractor's gravity force;

$$G_m = m_m \cdot g \tag{12}$$

    F_{it} – inertia of the tractor:

$$F_{it} = m_t \cdot \frac{dv}{dt} \tag{13}$$

    F_{im} – inertia of the aggregate:

$$F_{im} = m_m \cdot \frac{dv}{dt} \tag{14}$$

Since the suspension mechanism [4] is working in floating regime, the plow has the possibility to rotate in vertical-longitudinal plane around the instantaneous center of rotation, CIR_v, following the unevenness through the copying wheel's profile, keeping constant the working depth *a*. Therefore, the tractor-plow system is supported on the wheels of tractor's axels as well as on the copying wheel of the plow. Load forces acting on the tractor's axels are given by the torque equations of the forces acting on the tractor, in respect to points O_1 and O_2.

$$Z_1 = \frac{G_t \cdot (l_t \cdot \cos\alpha - h_t \cdot \sin\alpha) - G_m \cdot (h_m \cdot \sin\alpha + l_m \cdot \cos\alpha)}{L} -$$

$$- \frac{Fi_t \cdot h_t + Fi_m \cdot h_m - F_x \cdot (h_p - l_p \cdot tg\beta) + Fc_x \cdot (h_c + f_c \cdot l_c) + Mr_t}{L} + \frac{Fr_z \cdot l_r}{L}$$

$$Z_2 = \frac{G_t \cdot [h_t \cdot \sin\alpha + (L - l_t) \cdot \cos\alpha] + G_m \cdot [h_m \cdot \sin\alpha + (L + l_m) \cdot \cos\alpha]}{L} +$$

$$+ \frac{Fi_t \cdot h_t + Fi_m \cdot h_m - F_x \cdot [h_p - (L + l_p) \cdot tg\beta] - Fc_x \cdot [h_c + f_c \cdot (L + l_c)] + Mr_t}{L} - \frac{Fr_z \cdot (L + l_r)}{L}$$

(15)

The system of equations given above represents the mathematical model that describes the system's dynamic behavior in vertical-longitudinal plane, when moving on a tilted terrain having constant speed. This mathematical model can be used for analyzing (computer simulation) the rollover stability, provided that the load on the front axle to be at least 20% of tractor's weight.

Given the equations above, it results that using a copying wheel only some of the forces of the aggregate are transferred onto the tractor because a part of these are being taken by the copying wheel.

4. Theoretical researches on the dynamics of the tilling aggregate made of a tractor and a towed plow without copying wheel

Given the case when the tractor is a part of the tilling aggregate and the plow is not equipped with a copying wheel (as shown in Fig.3), the suspension mechanism is operates in an automatic control regime (for force, position or mixed).
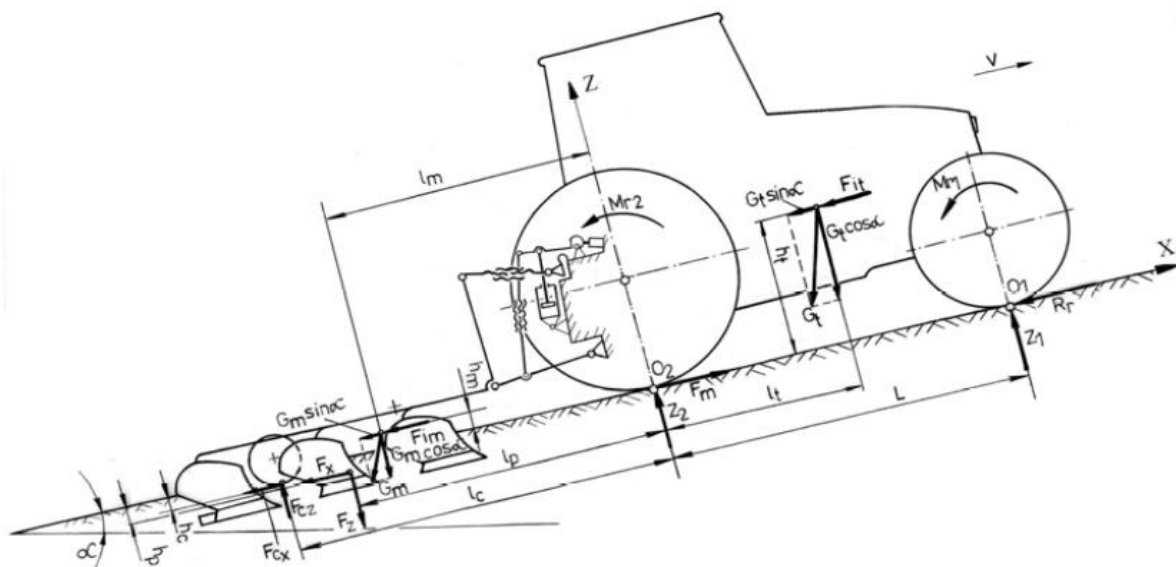

Fig. 3. Dynamic model, in vertical-longitudinal plane, of the tilling aggregate with towed plow without a copying wheel (automatic adjustment)

The case when the towed plow is not equipped with a copying wheel implies that its entire weight along with vertical components of the forces that act on the working bodies are transmitted to the

tractor's chassis through the suspension mechanism. Therefore, plow's frame is attached with the tractor's chassis [2].

Total load on the tractor's axels, Z_T, is given by summing the reaction forces, Z_1 and Z_2, on the two axels, as follows:

$$Z_T = Z_1 + Z_2 = (G_t + G_m) \cdot \cos\alpha + F_z - Fc_z \tag{16}$$

The reaction forces in the suspension points of the tractor's drivetrain are determined from the torque equilibrium equations in respect with support points O_1 and O_2 of tractor's axels, as follows:
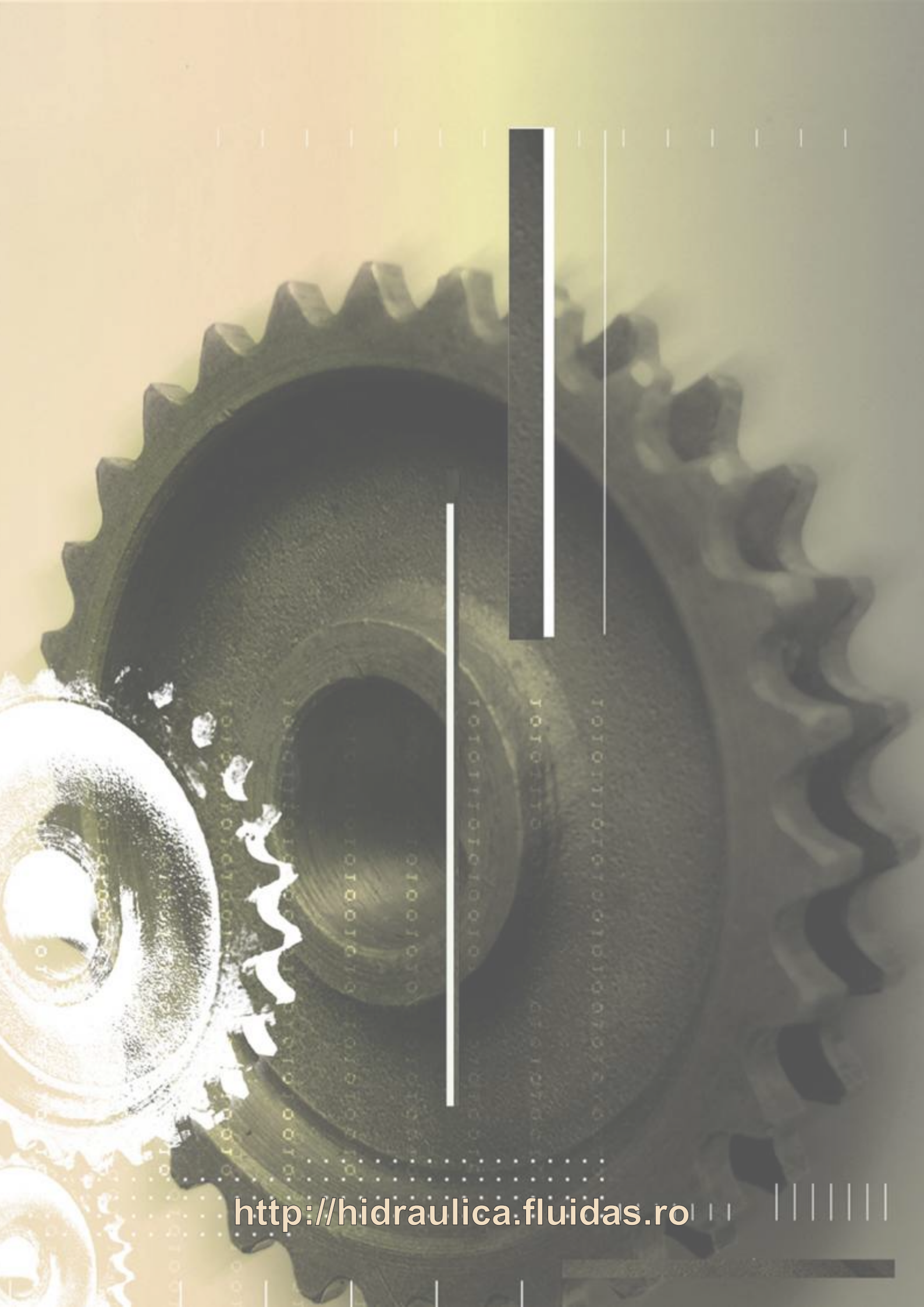
$$Z_1 = \frac{G_t \cdot (l_t \cdot \cos\alpha - h_t \cdot \sin\alpha) - G_m \cdot (h_m \cdot \sin\alpha + l_m \cdot \cos\alpha)}{L} -$$

$$- \frac{Fi_t \cdot h_t + Fi_m \cdot h_m - F_x \cdot (h_p - l_p \cdot tg\beta) - Fc_x \cdot (h_c + f_c \cdot l_c) + Mr}{L}$$

$$Z_2 = \frac{G_t \cdot [h_t \cdot \sin\alpha + (L - l_t) \cdot \cos\alpha] + G_m \cdot [h_m \cdot \sin\alpha + (L + l_m) \cdot \cos\alpha]}{L} +$$

$$+ \frac{Fi_t \cdot h_t + Fi_m \cdot h_m - F_x \cdot [h_p - (L + l_p) \cdot tg\beta] - Fc_x \cdot [h_c + f_c \cdot (L + l_c)] + Mr}{L} \tag{17}$$

Given the above it results that when the plow is not equipped with a copying wheel (automatic adjustment plow), the axels of the tractor have an additional load equal with the load that would have been taken by the copying wheel.

References

[1] Caproiu, St. et al. „*Masini agricole de lucrat solul, semanat si intretinere a culturii*", Didactic and Pedagogic Publishing House, Bucharest, 1982;

[2] Ormenisan, A. N. ,"*Cercetari teoretice si experimentale privind influenta sistemelor de reglare automata ale mecanismelor de suspendare ale tractoarelor asupra dinamicii si energeticii agregatelor de arat*", PhD thesis, Transilvania University of Brasov, Faculty of Food and Tourism, 2014;

[3] Sandru A., Popescu S., Cristea I., Neculaiasa V., „*Exploatarea utilajelor agricole*", Didactic and Pedagogic Publishing House, Bucharest, 1983;

[4] David L., Dinu I., „*The modernization of the MAC – 3 machines from the substitution of the mechanism of the pressing room*", Hidraulica Magazine, no. 3-4/ 2012, pp. 67-72.